UNIVERSITÀ DEGLI STUDI DI PADOVA

Dipartimento di Fisica e Astronomia "Galileo Galilei"
Corso di Laurea Magistrale in Astronomia

Tesi di Laurea Magistrale

High-energy photons from blazars and constraints on the existence of Axion-like particles

Relatore:
Prof. Eugenio Bottacini
Correlatore
Prof. Alberto Franceschini
Dr. Giorgio Galanti

Laureando:
Francesco Cenedese

Anno Accademico 2021/2022

Index

1 Introduction

Gamma-ray astronomy is destined to play a crucial role in the exploration of the most extreme and the most violent non-thermal phenomena in the Universe. The great potential of this discipline is the impressive discovery space of many open questions of modern astrophysics and cosmology, such as the origin of galactic and extragalactic cosmic rays, particle acceleration and radiation processes under extreme astrophysical conditions, and the search for dark matter, and much more. Recent observational results and exciting theoretical predictions provide a strong rationale for a deep study of cosmic radiation with forthcoming satellite-borne and ground-based detectors in the so-called very-high-energy domain of the electromagnetic spectrum. Gamma astronomy occupies such a vast spectral range (over 9 orders of magnitude) that it is widespread divided into two regions: the High Energy (HE) between 100 keV and 100 GeV (10^5 - 10^8 eV), and the Very High Energy (VHE) reaching hundreds of TeV (10^{14} eV). Given the extraordinary band extension, different techniques are used to observe different photon energies. HE photons are detected by the currently flying most advanced pair conversion telescope on board NASA's Fermi satellite known as the Large Area Telescope (LAT). The LAT converts the incident gamma ray into an electron-position pair tracking the directions. Eventually the calorimeter allows reconstructing the energy of the incident photons. Due to the drop of the effective area around several hundreds of GeV, photons at these energies are not efficiently detected. For this reason, a completely different phenomenon is used to "observe" at the VHE: the Cherenkov radiation (chapter 5). With this technique, rather than directly detecting gamma-rays, the effect of this radiation is being observed.

The other source of information in the Universe for energies higher than VHE photons are cosmic rays, which gain even more than 10^{20} eV and neutrinos which can even exceed a hundred TeV. Neutrinos, however, interact extremely little with matter thus their investigation is still rather difficult (IceCube Observatory has detected about 70 neutrinos in several years). Regarding the very high energy photons and cosmic rays, it is possible to trace them during their passage in the atmosphere. Motivated by a very recent research by Galanti et al.[(1), 2020], this thesis explores the need to call into existence the presence of exotic particles, known as Axion-like particles (ALPs), to explain VHE spectra of galaxies pointing a jet towards Earth that we call blazars. The focus of the problem is the comparison between the spectra emitted slope by low and high redshift sources. No discrepancy between these spectra is expected using conventional physics models. Instead, if there was a systematic evolution of the spectra as the redshift grows, the ALP hypothesis would be the most accredited proposal to solve the problem. To answer this question, an entire category of blazars was

analyzed: 90% of the blazar spectra observed at VHE found in literature were used in this thesis. Moreover, to further expand the database of spectra, more spectral observations for each single source were considered. In this way, a more in-depth analysis should be obtained, and greater account should be taken of the fluctuations of the spectral indices over time. Very importantly, this thesis also accounts for the different classes of blazars that feature intrinsically different spectra. Such an approach allows for more homogenous results. For all these reasons, this thesis can therefore be considered a rather complete analysis.

In this thesis I have first applied analyses dictated by conventional physics. After accounting for all such possible avenues, also the presence of ALPs has been analyzed.

The thesis is structured as follows. Various aspects and consequences, including current constraints on the ALPs are discussed in Chapter 2, along with a description of the actual theory and how these particles can significantly modify the optical depth of gamma radiation. The Extragalactic Background Light as the low-energy photon field responsible for the high-energy cosmic opacity is discussed in Chapter 3. This section also includes the model by Franceschini (2) to correct for the gamma-ray flux attenuation by the EBL. The blazars and their multiple characteristics, that make them an extremely peculiar sources, are described in Chapter 4. Chapter 5 describes the sample of the blazars observed so far and the main photon observation technique at VHE. In Chapter 6 there is the actual analysis of the data divided into three sections: the observational analysis, the EBL correction with conventional physic and the EBL correction taking into account the ALPs. The results found are summarized in plots in each subchapter. Finally, in Chapter 7 the conclusions of this thesis are presented.

2 Standard model of fundamental interactions

2.1 Standard model

The 20th century witnessed a spectacular revolution in our understanding of the fundamental laws of nature, that culminated with the establishment of the Standard Model (SM) of particle physics, the theory that describes with accuracy (at least as far as our experimental accuracy) the results of every experiment performed so far in particle physics. There are however many reasons to believe the SM is not an ultimate theory of nature. Some decades ago, it could have been argued that the SM does not include the gravitational interactions, so successfully described at the classical level by Einstein's theory of general relativity, and so it has to be extended or embedded in a more complete theory. Another old problem of the theory is the CP (Charge-Parity) symmetry of strong interactions. The equations that describe the fundamental interactions are in fact not symmetrical for a simultaneous variation of charge and parity. It has long been known that weak interactions violate this symmetry, in accordance with the theory. On the contrary, strong interactions preserve it, contrary to the theory. To recover the CP symmetry, some theoretical physicists have therefore hypothesized the existence of a new scalar field, in some ways similar to the famous Higgs field. This new field, with a mechanism very similar to the one that generated the Higgs boson, would be activated in the early Universe following a symmetry breaking, generating a new particle of small and very elusive mass: the axion. There are currently several other unsolved problems: more than 30 arbitrary parameters have to be fine-tuned in order to explain observations (3) and no unification of strong and electroweak interactions is accomplished. Perhaps the most pressing SM problem comes from cosmology, which seems to be also extremely well described by a classical solution of Einstein's gravity equations, a homogeneously expanding Universe with some primordial inhomogeneities seeded by tiny quantum fluctuations during an exponential expansion phase, so-called primordial inflation. This excellent description requires a few ingredients that are nowhere to be found in the SM: Dark Matter (DM), a substance that behaves under gravity as cold gas of non-baryonic weakly interacting particles, Dark Energy (DE), which gravitates as Einstein's famous cosmological constant, and at least a new field whose potential energy drives inflation for some time and then transforms somehow into the radiation that will dominate the energy density of the Universe during Big Bang Nucleosynthesis. Amongst these three, the evidence for Cold DM is the most precious for particle physics as it is directly attributable to the existence of new species of particles, i.e. it has been convincingly proven that the majority of DM is not in the form of neutrinos or any other SM particle. The main candidate is just the axions due to their characteristics: low mass and weak reactivity with other standard particles.

2.2 New physics and quantum gravity

The SM itself also provides compelling reasons to seek a more fundamental theory of nature. Most of them follow the same pattern: the lack of symmetry of the SM will be alleviated as we consider physics at higher energy scales. New particles/fields are expected to appear and restore symmetries that are not altogether evident in the SM. Couplings can be all related at high energies and still lose this unified character at low energies because they run with the energy scale. Electroweak and strong interactions could be two aspects of the same Grand Unified Theory (GUT) at a very high energy scale of 10^{15} GeV where quarks and leptons would also be different ingredients of the same multicomponent fundamental field. Other ideas consider the unification of the fermion generations into the framework of family symmetries. Finally, theories beyond the framework of quantum field theory have to be invoked to include gravity at the same quantum footing than the rest of known interactions. In this context, processes involving VHE photons and opacity measurements in distant gamma ray sources allow us important tests for possible deviations from the Standard Model predictions, and for new physics, well beyond the reach of the most powerful terrestrial accelerators (i.e., the Large Hadron Collider).

In particular, possible violations of a fundamental physical law such as the special-relativistic Lorentz Invariance are testable in principle. Such violations may arise in the framework of alternative theories of gravity and quantum gravity [(4), (5)]. While quantum gravity effects are expected to manifest themselves in the proximity of the extreme Planck's energy $E_{QG} = \sqrt{hc^5/2\pi G} \simeq 10^{19} GeV$, it turns out that the effects may be testable even at much lower energies. In particular, the quantization of space–time may affect the propagation of particles and a modification of the dispersion relation for photons in the vacuum would appear at an energy given by E_{QG}, bringing for example to a relation

$$c^2 p^2 = E^2 (1 + {}^{\lambda E}/_{E_{QG}} + \vartheta({}^{E}/_{E_{QG}}))^2 \qquad\qquad (2.1)$$

E the photon energy and λ a dimensionless parameter, that, if different from zero, would violate the Lorentz invariance (6). Such a dispersion relation leads to an energy-dependent propagation velocity of photons: $v = dE/dp = c(1 - \lambda(E/E_{QG}))$, with a consequent time of arrival also depending on energy that is testable with VHE observations of fast transient sources like variable blazars or even Gamma Ray Bursts (GRB) (7). The interesting point here is that an anomalous dispersion as above would also affect the interactions of high energy particles, like the photon–photon collisions. The threshold condition for pair creation, given one photon of energy and momentum E_1 and P_1 and a

second with E_2 and P_2 given by $(E_1 + E_2)^2 - (\vec{P}_1 - \vec{P}_2)^2 \geq 4m_e^2 c^4$, would be modified by the anomalous dispersion as $2(E_1 E_2)(1 - cos\theta) - \lambda E_1^3 / E_{QG} \geq 4m_e^2 c^4$, with θ the angle between the two photons, m_e the electron mass and assuming E_1 is the gamma photon energy and E_2 that of the low-energy background. The most conspicuous framework in which this appears to be possible, at least in principle, is the framework of string theories in 10 dimensions. A key point of the superstrings and superbranes theories is the prediction of axion-like particles (ALPs) existence.

2.3 Axions and ALPs

Axions and other very light axion-like particles appear in many extensions of the SM and are leading candidates to compose part or all of the missing matter of the Universe. They also appear in models of inflation, dark radiation, or even dark energy, and could solve some long-standing astrophysical anomalies. The axion is a pseudo-scalar boson with zero spin characterized by the presence of a coupling to the photon, through an interaction of the type $F\tilde{F}a$ (or $a\gamma\gamma$). It was first invoked in the 1970s to resolve the strong CP problem (8). The axion mass is believed to be very small, theoretical calculations identify it around 10^{-5} eV (in natural units) $(m_{axion} \lesssim 10\ meV\ [\ (9),\ (10)]$, about one million times smaller than the current limits on the neutrinos mass: the coupling with ordinary matter is strongly suppressed by a factor of 10^{-12} compared to that of pions or other families of particles. The axion interacts with fermions, two gluons and two photons, and one of its characteristic feature is the existence of a strict linear relationship between its mass m_{axion} and axion-photon coupling constant $g_{a\gamma\gamma}$[1]:

$$m_{axion} = 0.6\ eV \left(\frac{10^7\ GeV}{f_a}\right) \qquad\qquad (2.2)$$

where $f_a = \frac{g}{2\pi}\frac{1}{g_{a\gamma\gamma}}$, with g the strong coupling constant. Both the mass and the strength of these couplings are inversely proportional to f_a, an energy scale related to the spontaneous breaking of the Peccei-Quinn symmetry, so that the smaller the mass the weaker the couplings. Indeed, the first Weinberg (11) and Wilczek (12) models had f_a of the order of the electroweak scale and were soon

---

[1] A coupling constant is a number that determines the strength of the force exerted in an interaction.

ruled out [(13), (14)]. However, very soon it was realized that f_a could correspond to a much higher energy scale [(15), (16)] which implies very low mass and weakly interacting axions. These axions were so weakly coupled that they were dubbed invisible axions. The tests constraint the values of $f_a \gg 10^7$ GeV, which imply very small masses $m_{axion} \ll eV$. Indeed, the axion is the paradigm of the so-called weakly interacting slim particles WISPs (17) and its discovery would imply the identification of a new energy scale in particle physics.

ALPs are generalizations of the axions, however they differ in two respects. ALPs are supposed to couple primarily only to two photons while other interactions are discarded. While for the axion its coupling to fermions and two gluons is essential in order for the Peccei-Quinn mechanism to work. Moreover, ALPs mass m_a and axion-photon coupling constant $g_{a\gamma\gamma}$ are unrelated parameters. This is very important for the model used in this thesis because they will be considered as independent free parameters.

The key-point of the ALP scenario is that ALPs do neither interact with the EBL, in spite of the fact that they couple to two photons, nor with the ionized intergalactic medium. Indeed, ALPs might interact with the EBL only through two processes: $a + \gamma_{EBL} \rightarrow a + \gamma_{EBL}$ and $a + \gamma_{EBL} \rightarrow f^+ + f^-$, where f denotes a generic charged fermion. For the process $a\gamma_{EBL} \rightarrow a\gamma_{EBL}$ a cross section estimate $\sigma_{(a\gamma_{EBL} \rightarrow a\gamma_{EBL})} \lesssim (E_{EBL}E_{ALP}/GeV^2) 10^{-68}$ cm^2, which shows that this process is negligibly small for any reasonable choice of E_γ and E_{ALP}. The same goes for the process $a\gamma \rightarrow f^+f^-$: $\sigma_{(a\gamma_{EBL} \rightarrow f^+f^-)} < 10^{-52} cm^2$.

Apart from the two-photons mechanism, the only other possible process is $af \rightarrow \gamma f$. However, we have again $\sigma_{(af^\pm \rightarrow \gamma f^\pm)} < 10^{-52} cm^2$. As a consequence, for all practical purposes ALPs neither interact with photons nor with any fermion in these ways.

The ALP theory can be described by the Lagrangian:

$$\mathcal{L}_{ALP} = \frac{1}{2}\partial^\mu a\, \partial_\mu a - \frac{1}{2}m_a{}^2 a^2 + \mathcal{L}_{a\gamma} \qquad (2.3)$$

where a is the axion field and m_a is the ALP mass. What best characterizes the ALP theory is the last one term: the Lagrangian $\mathcal{L}_{a\gamma}$. It describes the photon-ALP mixing, i.e. the coupling between ALPs and photons in a magnetic field:

$$\mathcal{L}_{a\gamma} = -\frac{1}{4}g_{a\gamma\gamma}F_{\mu\nu}\tilde{F}^{\mu\nu}a = g_{a\gamma\gamma}E \cdot B\, a \qquad (2.4)$$

where E and B are the electric and magnetic components of the field strength $F^{\mu\nu}$ and $\tilde{F}^{\mu\nu}$ is its dual: $\tilde{F}^{\mu\nu} = \frac{1}{2}\epsilon^{\mu\nu\rho\sigma}F_{\rho\sigma}$. This means that ALPs and photons can oscillate in each other in the presence of an external electromagnetic field. The CERN Axion Solar Telescope (CAST) experiment gives a bound on $g_{a\gamma\gamma} < 6.6 \cdot 10^{-11}\,\text{GeV}^{-1}$ for ALP masses $m_a < 0.02\,eV$ at the 2σ level [(18), (19), (20)]. As the electric field of a photon is orthogonal to its wave vector (k), the dot product in $\mathcal{L}_{a\gamma}$ means only the component of the external magnetic field (B in $\mathcal{L}_{a\gamma}$) that is transverse with respect to the direction of beam propagation (B_T) is important for mixing. Similarly, only the component of E in the plane spanned by B and k is involved in the mixing ($E_{||}$), meaning only photon polarization states along $E_{||}$ mix with ALPs. Hence, the term $g_{a\gamma\gamma}E \cdot B\,a$ acts as a polarizer. Specifically, besides $\gamma \leftrightarrow a$ oscillations, for an initially linearly polarized photon beam two effects occur. One is birefringence, namely the linear polarization becomes elliptical with its major axis parallel to the initial polarization. The other effect is dichroism, namely the polarization-dependent selective photon conversion, which causes the ellipse major axis to become misaligned with respect to the initial polarization.

The oscillation phenomenon is linked to the non-coincidence of the interaction eigenstates of the photon-ALP system with those of propagation, i.e. the evolution equation of this system has a propagation matrix with non-diagonal terms, the presence of these terms generates a not zero probability that a photon traveling in an external electromagnetic field converts into ALP and vice versa. In summary, supposing the photon of energy E traveling along the z direction in a magnetic field, the mixing matrix of the system will be of the type:

$$\mathcal{M}(E,y) \equiv \begin{pmatrix} w(E,y) & 0 & v(y)\sin\phi(y) \\ 0 & w(E,y) & v(y)\cos\phi(y) \\ v(y)\sin\phi(y) & v(y)\cos\phi(y) & u(E) \end{pmatrix} \tag{2.5}$$

with $\phi(y)$ denoting the angle between B_T and the fiducial fixed x direction. The quantities $v(y)$ and $u(E)$ are real, but $w(E,y)$ can be complex. We will see in chapter 6 the true nature of these factors but we can already say that they depend on many parameters: m_a, w_{pl}, B_T, $g_{a\gamma\gamma}$ and the photon mean free path $\lambda_\gamma(E)$. We note that if the matrix were diagonal there would be no oscillation, as there would be no mixing between eigenstates.

The phenomenon of photon-axion oscillation is similar to what happens for neutrinos, but there is a substantial difference. All neutrinos have the same spin, so neutrino oscillations can occur freely. The ALP, on the other hand, is supposed to have zero spin while the photon has a unitary spin, so one can

only transform into the other if there is an external magnetic field that compensates for the spin difference between the two particles.

Solving the full equations of motion for the photon-ALP system, in the simplest possible case, where no photon absorption take place and B is homogeneous, one realizes that the conversion probability becomes maximal and independent of energy above a critical energy $E_L = \frac{|m_a^2 - w_{pl}^2|}{2 g_{a\gamma\gamma} B_T}$, where B_T denotes the field strength transversal to the photon propagation direction, $g_{a\gamma\gamma}$ the photon-ALP coupling, and w_{pl} the plasma frequency of the medium. Taking in this regime, for example, the y-axis along B, the conversion probability γ-ray in ALP is:

$$P_{\gamma_y \to a}(z) = sin^2 \left(\frac{g_{a\gamma\gamma} B_T z}{2} \right). \tag{2.6}$$

Since this regime is the maximum possible it is known as strong mixing regime. This regime persists as long as:

$$E < E_H = g_{a\gamma\gamma} B_T \left[1.42 \cdot 10^{-4} \left(\frac{B_T}{B_{cr}} \right)^2 + 0.522 \cdot 10^{-42} \right]^{-1}, \tag{2.7}$$

with the critical magnetic field $B_{cr} \sim 4.4 \times 10^{13} G$.

For $E \sim E_L$ and $E \sim E_H$ the $\gamma \to a$ conversion probability rapidly oscillates with E: weak-mixing regime. Above E_H, the oscillations are damped due to the quantum electrodynamics (QED) vacuum polarization. When ALP mass effect at low energies is important (see the oscillatory region at low energy in Fig. 2.1) the $\gamma \to a$ conversion probability $P_{\gamma \to a}(E, m_a, g_{a\gamma\gamma}, B)$ predicts spectral irregularities in observational data, which are related to the value of m_a and $g_{a\gamma\gamma}$. This is due to the relation between the observed spectrum F_{obs} and the emitted one F_{em}:

$$F_{obs} = P_{\gamma \to \gamma}(m_a, g_{a\gamma\gamma}) \cdot F_{em}, \tag{2.8}$$

with $P_{\gamma \to \gamma}$ denoting the photon survival probability in the presence of photon-ALP interaction.
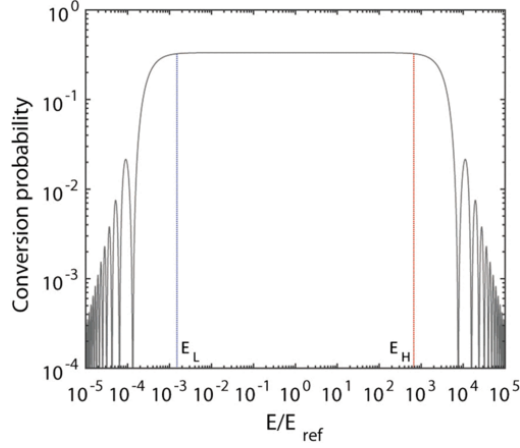
Figure 2.1: Behavior of $P_{\gamma \to a}$ versus E/E_{ref} where E_{ref} is a reference energy. Also E_L and E_H are plotted. Taken from (21).

A natural question arises: how large is E_L? Obviously, the answer depends on $g_{a\gamma\gamma}$, but in order to get an orientation it is enough to know its upper bound. As already mentioned, due to the negative result of the CAST experiment, the resulting bound is $g_{a\gamma\gamma} < 0.66 \cdot 10^{-10}$ GeV^{-1} ; incidentally, exactly the same bound at the same confidence level has been obtained from the study of a particular kind of globular cluster stars (22). Correspondingly, neglecting w_{pl} that is very small for simplicity, the critical energy becomes[2]:

$$E_L > 3.90 \cdot 10^{11} \left(\frac{m_a}{eV}\right)^2 \left(\frac{G}{B}\right) GeV \qquad (2.9)$$

Thus, we see that for astrophysical magnetic fields in the range $(10^{-10} - 10^{-5})$ G, even for very small values of m_a, it turns out that E_L tends to fall into the X- and γ-ray bands. Therefore, $\gamma \leftrightarrow a$ oscillations are expected to show up in high-energy astrophysics.

However, it is important to note that the arguments made concern only the photon-ALP conversion and does not take into account the interaction of gamma photons with those of lower energy. A great uncertainty afflicts the configuration of the external magnetic field responsible for the photon-ALP oscillations. The magnetic fields crossed by photons in their motion towards the Earth extend on different intensity scales. An interesting estimate of the extent of these fields generated by different celestial objects (stars, galaxies, clusters, etc.) is provided on an experimental basis by the Hillas plot (Figure 2.2), which plots the intensity of these fields as a function of length over which they extend. As can be seen from Figure 2.2, a magnetic field is certainly present inside the photon source (blazar,

---

[2] Natural Lorentz-Heaviside (rationalized) units with ℏ = c = k$_B$ = 1 are employed throughout this thesis. The magnetic field B is expressed in Gauss (G) and so 1 G $\simeq 1.953 \times 10^{-2}$ eV^2.

stars), furthermore the magnetic fields in the Milky Way give a not negligible contribution to the effects we are considering, the same is true for the magnetic fields generated by clusters of galaxies that the photon passes through on its way to Earth. So far, $\gamma \leftrightarrow a$ oscillations have been considered in a variety of astronomical objects, like active galaxies, spiral and elliptical galaxies, the Milky Way, clusters of galaxies and extragalactic space, since they are all magnetized structures. The jet, the intergalactic magnetic field (IGMF) and the galactic (Milky Way) magnetic field (GMF) contributions are usually estimated in ALPs correction models. However, other searches use a cluster magnetic field (CMF) as the main mixing region (e.g., (23)).
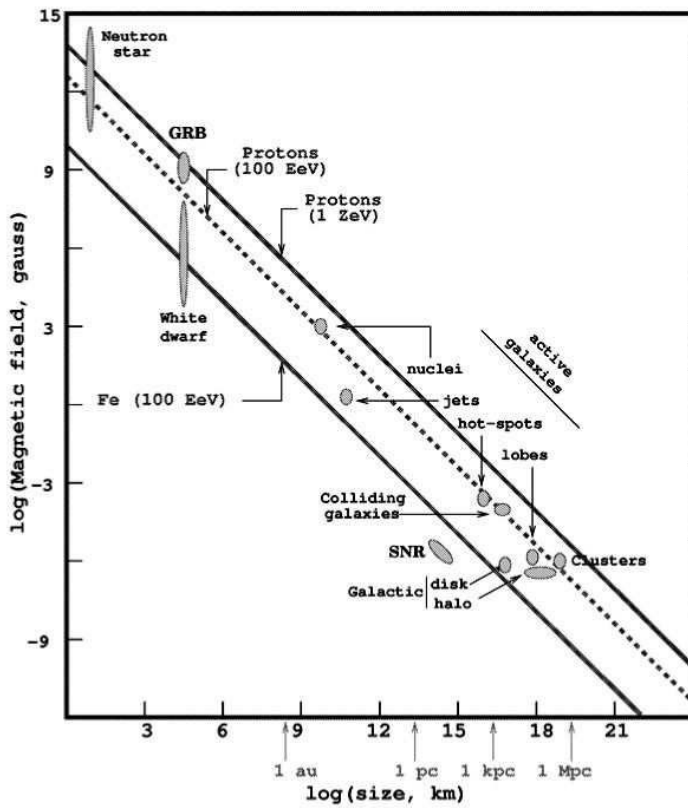

Figure 2.2: Hillas plot: results of studies on magnetic fields generated by celestial sources (stars, galaxies, cluster,..) as a function of the lengths over which they extend. Taken from (24).

Regarding the magnetic field near the blazar, the models are unfortunately rather vague at the moment. Because of the E · B term in $\mathcal{L}_{a\gamma}$, ALPs only see the component of external magnetic field transverse to their direction, so we need to model the magnetic field direction as well as the strength along the whole of the jet to solve the mixing equations. In contrast to the overall jet magnetic field strength and distance dependence that are relatively well agreed upon, the jet magnetic field orientation

10

structure is currently not very well understood, especially at small scales close to the black hole. The overall magnetic field should become dominated by the transverse component with strength $\propto 1/r$ but, jet magnetic field structure is certainly more complicated, particularly at small radii. For one thing, in a parabolic base, the same flux argument would make the transverse component go as $1/r^a$, where a is the parabolic index (~ 0.58 in M87). Many rotation measure maps show asymmetry across the jet in a way indicative of helical magnetic fields at both parsec and (for powerful sources) kiloparsec scales [(25), (26)] – meaning the field is not purely transversal. It also seems unlikely that the magnetic field within such a violent environment would be entirely ordered. A tangled field could change the transverse field dominance, even at large radii, because a large poloidal field with many reversals could nevertheless have a small net flux down the jet. Entrainment of matter and the surrounding field would likely have a tendency to disorder the magnetic field, producing a tangled component (as well as changing the dependence from flux conservation). Fitting of models to Mrk 501 maps has provided observational support for this idea, deriving fractions of magnetic energy density in a tangled component up to 0.7 (27). So, for ALP searches, it is not obvious how to model the transverse magnetic field component in the jet properly. Clearly the values vary with the distance and from source to source but typical values are: $B_T(r_{em} = 0.3 \, pc) \simeq 0.8G$ and $n_e(r_{em}) = 5 \times 10^4 cm^{-3}$ (28), where r_{em} is the location of the gamma-ray emission region measured from the black hole.

Apart from the case of active galaxies and clusters of galaxies, in all the other systems the magnetic field B can be approximated with models more accurate. For example, a classical model is called domain-like sharp-edges (DLSHE) model. The idea is that the intensity of the magnetic field remains constant in intervals (domains) called coherence lengths. These usually, in extragalactic cases, are smaller than 10 Mpc. However, the direction of the magnetic field changes randomly within the domain and discontinuously passing from one domain to the next. Different domains can have different intensities of B. Another important feature for the model is the oscillation length (l_{osc}) of ALP-photon mixing. It depends on the ALP mass (ma), the ALP-photon coupling ($g_{a\gamma\gamma}$), the photon energy (E), the transverse field strength (B_T), and the electron number density (n_e) of the mixing environment. In the case of relativistic jets, compared to the extragalactic medium, there is a significant difference in the magnetic field intensity and in the electron number density. In fact, the electrons in relativistic jets cannot be interpreted as a cold plasma. Therefore, the photon effective mass depends on the nonthermal distribution function of electrons in the jet instead of simply being the plasma frequency as it is in a cold plasma.

The extragalactic magnetic field $Bext$ has large uncertainties in the range $10^{-7} \, nG < Bext < 1.7 \, nG$ on the scale $\mathcal{O}(1 \, Mpc)$. However, models contemplating galactic outflows especially from

dwarf galaxies are generally believed to be the source of $Bext$. Accordingly, $Bext$ turns out to have a domain-like structure with field strength of $\sim nG$, $n_e^{IGMF} \simeq 10^{-7} cm^{-3}$ and coherence lengths vary between $0.2\ Mpc$ and $10\ Mpc$.

For this model an important thing is that domains (L_{dom}) are shorter than the photon-axion oscillation length (l_{osc}) because when $l_{osc} \lesssim L_{dom}$ a whole oscillation, or even several oscillations, are contained inside a single domain, thereby implying that the photon-ALP conversion probability, across a single domain, depends on the domain shape. This is indeed what happens above or below a certain energy threshold in a variety of astronomical objects, radio lobes, spiral galaxies, starburst galaxies, elliptical galaxies and extragalactic space. For instance, a particular case study in which indeed the condition $l_{osc} \lesssim L_{dom}$ occurs, owing to the photon dispersion on the CMB (Cosmic Microwave Background), is a photon/ALP beam of energy $E \gtrsim \vartheta(40\ TeV)$ with a large uncertainty traveling in extragalactic space [(29), (30)]. However, this will concern observations made with new generation telescopes (CTA) since, so far, the observations reach a maximum of a few tens of TeV. Whenever $l_{osc} \lesssim L_{dom}$ the use of the DLSHE model gives rise to meaningless results because of its unphysical nature. In addition, it looks fairly unrealistic to suppose that all magnetic domains have exactly the same size: a random spread of L_{dom} within a given range looks much more realistic. In order to save the situation, the model smooths out the edges in such a way that the components of B change continuously across the edges between adjacent domains, thereby obtaining the domain-like smooth-edges (DLSME) model.

However, under strong mixing conditions, using a classical field theory, the characteristic length of the photon-axion oscillations $z = l_{osc} \simeq \frac{2\pi}{g_{a\gamma\gamma}B_T}$ can be estimated around $l_{osc} \simeq 100\ Mpc \left(\frac{10^{-11}GeV^{-1}}{g_{a\gamma\gamma}}\right)\left(\frac{10^{-9}G}{B}\right)$, therefore much larger than the estimated coherence length for extragalactic magnetic fields. For this reason, the DLSHE model is often used to describe the IGMF contribution.

For the GMF, the model of Janson and Farrar is usually used. It includes a disk field and a halo field with strength $B \simeq 5\ \mu G$ and a coherence length $L_{dom} \simeq 10\ kpc$. For this model, the electron number density in the Milky Way is $n_e^{GMF} \simeq 1.1 \times 10^{-2} cm^{-3}$.

In the current models, despite the lower values of B, the IGMF contribution is considered the most important for mixing. As well as for long distances, also because in this region it is necessary to take into account the VHE photons interaction with the extragalactic background photons. For this reason, in this thesis it was decided to use the DLSHE model. However, according to recent studies, mixing near blazars could be significant (31).

2.4 Astrophysical constrains on ALPs

Current ALP research involves many researchers in various fields: from particle physics, to astrophysics and cosmology. Given ALPs extremely weak interaction with matter, no direct measurements are made. The key to the experiments is to exploit a fundamental consequence of the presence of a coupling: the phenomenon of photon-axion mixing. This effect, according to current theories, involves the oscillation between photon and ALP in the presence of an external electromagnetic field. This conversion is very important as it allows you to indirectly investigate the ALPs based on the effect they generate on photons.
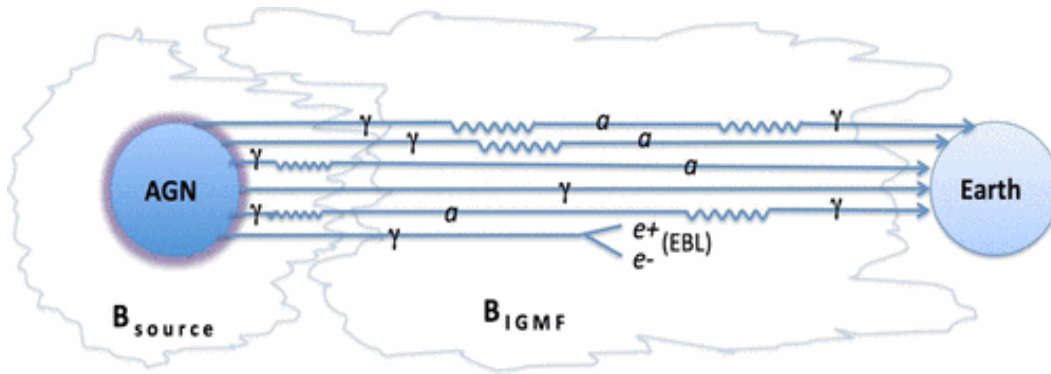

Figure 2.3: Photon to ALP oscillations (or vice-versa) are represented by a crooked line, while the symbol γ and a mean gamma-ray photons and ALP respectively. This diagram collects the main physical scenarios that we might identify inside our formalism. Each of them are schematically represented by a line that goes from the source to the Earth. Taken from (32).

Actually, the possibility of $\gamma \rightarrow a$ and $a \rightarrow \gamma$ conversions is of paramount importance for the ALP detection with various techniques. They include ALPs production in the Sun core through the Primakoff process $\gamma + ion \rightarrow a + ion$ and their subsequent conversion into photons of the same energy inside one or more superconducting hollow blind magnets pointing towards the Sun, like in the CAST experiment (18) and in the planned IAXO (International Axion Observatory) experiment. IAXO is a next generation helioscope, it should be able to obtain a signal-to-noise ratio about 5 orders of magnitude better than CAST and to probe couplings $g_{a\gamma\gamma}$ as low as $5 \cdot 10^{-12} GeV^{-1}$ for $m_a < 0.01 \, eV$ (33). However, the signals of non-Primakoff axions in helioscopes depend of the corresponding product of couplings, and typically do not compete with astrophysical limits.

Remarkably, just the same conversion-reconversion mechanism allows for the 'shining light through a wall' detection strategy like in the ALPS II experiment at DESY (34) and in the planned STAX experiment (35). Furthermore, ALPs can be detected with other strategies developed by Avignone and collaborators [(36), (37)]. Finally, in case ALPs build up the bulk of the dark matter then they can also be discovered by the planned ABRACADABRA experiment (38). In all these cases the magnetic field extends over a very limited distance, and in order to maximize the effect one has to resort to a magnetic field which is as strong as possible.

In astrophysics field, on the other hand, it is possible to exploit much greater distances and therefore the magnetic fields can be less intense to generate the same effect. According to current theories, ALPs could affect stellar evolution [(39), (40)] and cosmology (41) in a similar way to thermal neutrinos. As in Sun core, ALPs can be thermally produced in the hot and dense stellar interiors of globular clusters (GCs). In GCs, the ALP-photon coupling is best constrained by the ratio of horizontal branch (HB) to red giants. The ratio decreases as the HB phase is accelerated by the increasingly faster He-burning, due to the hotter temperature implied by axion emission through the Primakoff effect. The latest study of 39 GCs [(42), (43)] gives the constraint $g_{a\gamma\gamma} < 0.66 \times 10^{-10}\,\mathrm{GeV^{-1}}$, labeled as "HB" in Fig. 2.4. Recent research is also looking for ALPs in massive stars [(44), (45)] and supernova explosions. These cases investigate for very small ALP masses compared to laboratory experiments. In the first case, from observations of the Perseus cluster the results were $g_{a\gamma\gamma} \lesssim 5 \times 10^{-12}\,\mathrm{GeV^{-1}}$ for $5 \cdot 10^{-10}eV \lesssim m_a \lesssim 5 \cdot 10^{-9}eV$ at 2σ level. Instead from the lack of detection of gamma-rays from supernova SN1987A result $g_{a\gamma\gamma} \lesssim 5.3 \times 10^{-12}\,\mathrm{GeV^{-1}}$ for $m_a \lesssim 4.4 \cdot 10^{-10}eV$. All astrophysical bounds can be met provided that we assume $m_a = \mathcal{O}(10^{-10}eV)$. Therefore, this will be the value chosen for the model in this analysis. Axions could be discovered by experiments at the low-energy high-intensity frontier. This is because axions could mediate new long-range forces (46), allow rare decays, appear after thick walls in beam-dump experiments (light-shining-through-walls (LSW) experiment (47). Other experiments exploit a second effect linked to the ALP-photon interaction which consists in the change of the photon polarization state that passes through an external magnetic field. All these strategies so far have not led to any real detection however they have allowed us to place constraints on the mass and on the two-photon coupling constant $g_{a\gamma\gamma}$. The results of all these experiments are summarized in Fig. 2.4.
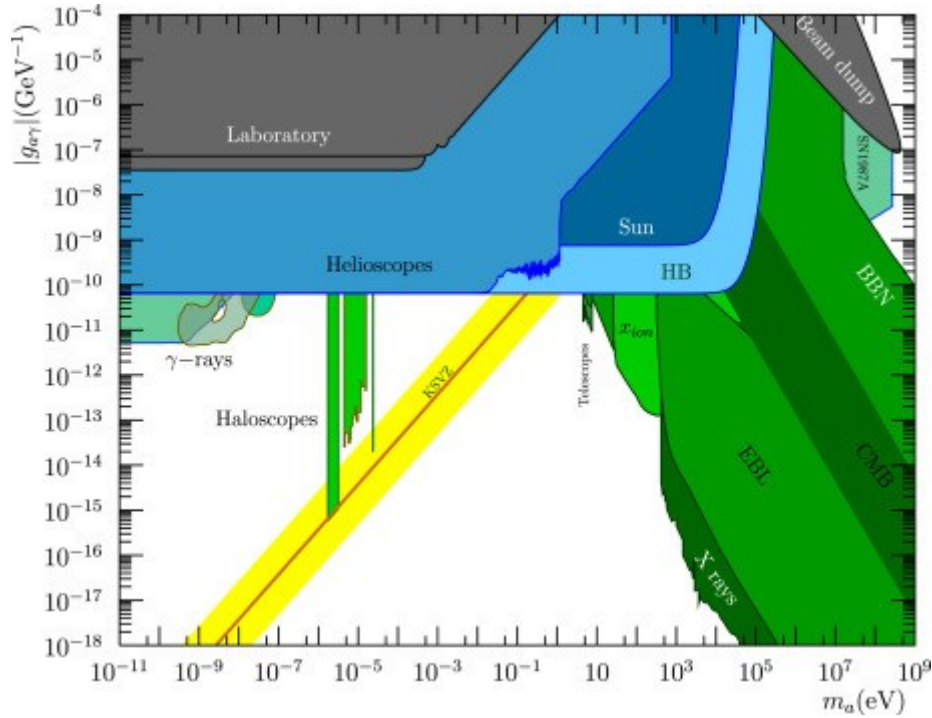
Figure 2.4: Review of current constraints in the overall $(g_{a\gamma\gamma}, m_a)$ plane. We introduce the color criteria for the rest of plots of this review: black/gray for purely laboratory results, bluish colors for helioscope experiments or bounds depending on stellar physics, and greenish for haloscopes or cosmology-dependent arguments. Yellow/orange are reserved for hinted regions of the parameter space, like, in this case, the QCD axion band. Taken from (48).

Any astrophysical manifestation of the presence of axions, however, have advantages over laboratory research. In fact, in astrophysical cases, the coupling constant $g_{a\gamma\gamma}$ can also have lower values than in the experimental case, and in any case lead to traceable effects. For example, interesting effects related to the photon-axion oscillation can be sought in the observations of X and gamma-ray beams coming from distant sources. The magnetic field can be very small as compared to the laboratory standards (apart from inside or around active galaxies, white dwarfs and neutron stars), but it extends over very much larger distances. Because the $\gamma \to a$ and $a \to \gamma$ conversion probability depends on the product of the magnetic field times the distance (as we shall see later), even a tiny magnetic field can produce sizable effects over astronomical distances [(49), (50)]. The main sources of gamma rays are active galactic nuclei (AGN). These are powered by mass accreting onto supermassive black holes and in some cases, they are characterized by the formation of two collimated relativistic oppositely oriented jets. An enormous amount of VHE radiation is emitted from the inner regions. When one of the jets is occasionally pointing toward the Earth the AGN is called blazar. Blazars are divided into two classes: flat spectrum radio quasars (FSRQs) and BL Lac objects (BL Lacs). FSRQs are more powerful and they are characterized by strong optical emission lines, while BL Lacs are less bright and they do not display significant emission lines. In FSRQs the VHE photons produced at the jet base interact with the optical photons of the broad line region (BLR) thereby disappearing by

15

producing an e^+e^- pair: in the BLR the optical depth τ is so high that no photon with energies above ~ 20 GeV is expected to leave the FSRQs. However, photons with energies up to ~ 400 GeV have been observed. In order to explain such a detection, one is forced to place the emission region beyond the BLR in order to avoid absorption. If we want instead to place the emission region, as in the standard AGN models, not too far from the center, then photon-ALP oscillations inside the jet magnetic field $Bjet = O(1G)$ can be invoked in order to reduce the effective BLR optical depth (51). In the left panel of Fig. 2.5 we can observe the dramatic reduction of the optical depth in the presence of photon-ALP interactions as compared to the standard τ: ALPs do not interact with BLR photons thereby increasing the effective VHE photon mean free path, thereby providing an explanation for photon emission well above 20 GeV without invoking ad hoc blazar emission models. BL Lacs do not present absorption regions as FSRQs so that VHE photons can escape from the central region unimpeded. In any case, photon-ALP conversion inside the jet magnetic field $Bjet = (0.1 - 1)$ G allows for the production of ALPs already in the source. The fraction of photon/ALP produced strongly depends on the values of the emission distance from the center, on $Bjet$ and on $g_{a\gamma\gamma}$ (52). The right panel of Fig. 2.5 shows that the estimate for the produced ALPs is fairly large with a reasonable choice of the parameters.
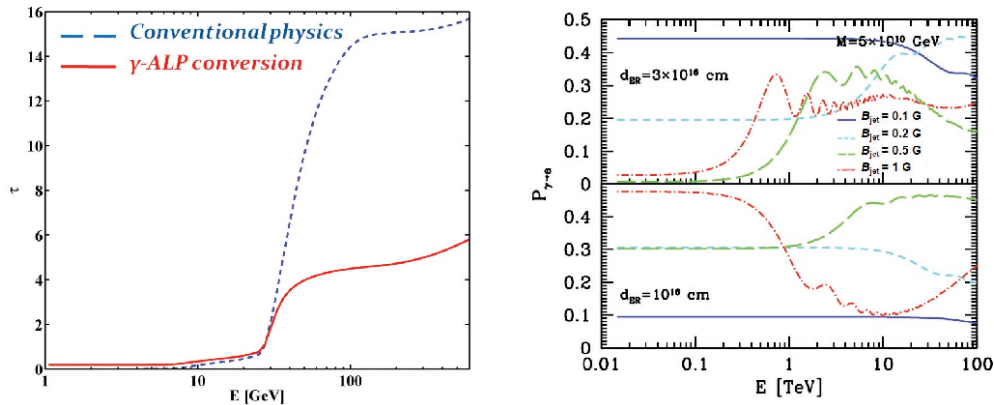
Figure 2.5: Photon-ALP interaction in blazars. In the left panel, for FSRQs it is report the BLR optical depth τ in the standard case and with photon-ALP interaction: $g_{a\gamma\gamma} \simeq 10^{-11} GeV^{-1}$ and $m_a < \mathcal{O}(10^{-10}$ eV$)$. In the right panel, for BL Lacs it is plot the photon-to-ALP conversion probability $P_{\gamma\to a}$ with $M \equiv 1/g_{a\gamma\gamma} = 5 \times 10^{10}$ GeV and different choices of the emission distance and of the jet magnetic field Bjet. Taken from (53).

The major problem of the study of these sources is linked to the average free path of the emitted photons, which are called VHEP (very high energy photons) due to the large energy transported: we are talking about energies higher than 100 GeV. This in fact is limited by the interaction of the gamma

photons with the background photons, which constitute background radiation emitted in the evolution of nearby galaxies. The interaction process is called photon-photon interaction ($\gamma\gamma \rightarrow e + e-$). So, a high-energy photon from a distant blazar has a non-negligible probability of scattering on such background photons, in the optical / infrared band, called EBL (extra-galactic background light) and therefore disappearing in $e + e-$ pairs. It follows that the radiation coming from such very distant objects should arrive on the Earth very little or even not arrive at all. However, this decrease can be calculated using current models (Franceschini et al. (54)). If we assume the oscillation mechanism between ALP and photon is present, the opacity associated with the gamma photon is considerably reduced since ALP does not interact with the EBL photons. In this case, the Universe would be more transparent to high-energy VHE radiation than it is in theories that take into account only the absorption with background photons and do not consider coupling to pseudoscalar particles. About this, recent observations have revealed a surprising degree of transparency of the Universe to γ radiation coming from distant sources that cannot be explained by the theory of absorption alone (1). Two complementary mechanisms have been proposed in this regard that also take into account the oscillations to explain these surprising observations: one of these supposes that the photon VHE-axion conversions occur in the magnetic fields around the sources and the conversion into photons occurs in the Milky Way, the other assumes that the oscillations occur in extragalactic magnetic fields. This second mechanism is what is properly called the DARMA scenario, from the initials of the physicists who first hypothesized it (De Angelis, Roncadelli and Mansutti). This would allow the VHEPs, in the presence of cosmic magnetic fields, to have a probability of conversion into ALP, not only near the blazar but during the entire travel: for this reason, ALPs are considered to be the mediators of the transparency of the Universe.

In reality, the extent of absorption by EBL is not yet well known, as the intensity and spectrum of these background photons are not well known and therefore it cannot be said how robust the interaction with VHEPs is. In this sense it would also be possible to resort to theories that do not need axions to explain the transparency of the Universe to VHE photons, even if the theories that take into account the coupling with such particles turn out to be a simple explanation of the transparency of the Universe.

This chapter is mainly based on Galanti, Roncadelli and Tavecchio papers [(21), (53), (30)], the review of Irastorza and Redondo (48), and other papers [(32), (31)].

3   Photon-photon interactions

Once the first cosmic sources, either stellar populations, galaxies, or gravitationally accreting Active Galactic Nuclei, started to shine at about redshift z ∼ 10, a large flow of low-energy photons went progressively filling up homogeneously the entire Universe. This photon field, covering a wide frequency range from the far-UV to the millimeter ($0.1 < \lambda < 1000$ μm) and growing with time down to the present epoch, is indicated as the Extragalactic Background Light (EBL). The fraction of the EBL that goes in wavelength from the UV to the near IR is called Cosmic Optical Background (COB) and the fraction going from the near IR to the far IR is called Cosmic Infrared Background (CIB). COB is powered by a dominant source of energy: thermonuclear burning in stars, whose past integral peaks in the EBL at around $\lambda \simeq 1$ μm, as a consequence of surface temperature of stars from few to about 100 thousand degrees. However, stellar activity often takes place in dust-opaque media, as is particularly the case for young massive stars, the most luminous, that form inside dusty molecular clouds. As a consequence, a quite significant fraction of the short wavelength UV-optical stellar photons is absorbed by dust grains and re-emitted by them in the IR via a quasi-thermal process at the equilibrium temperature of few tens of degrees. The EBL then has two fairly well characterized maxima at $\lambda \simeq 1$ μm and 100 μm corresponding to the integrated stellar photospheric and dust-reprocessed emissions, with a minimum between the two at $\lambda \simeq 10$ μm (Fig.3.2 right). The contributions to the EBL of the radio, UV, X-ray and gamma-ray extragalactic backgrounds are smaller by one to three orders of magnitude than the COB and CIB (55). Another important energy-generation process originates from gas accretion onto massive collapsed objects, like it typically happens onto super-massive black-holes (SMBH) in Active Galactic Nuclei and quasars. Similarly to stellar emission, gravitational accretion also emits fluently in the UV and the optical from the hot accreting plasmas, but again significant part of this radiation is absorbed by dust in the accreting matter and emerges in the IR. In spite of the higher mass-to-energy transformation efficiency η of the latter process compared to stellar nucleosynthesis, because only about one part of a thousand of the processed baryon material goes to accrete onto the SMBH, AGN accretion is deemed to contribute a minor fraction to the EBL compared to stars [(56), (57)]. Assuming a stellar efficiency of $\eta \sim 0.001$ and the AGN one $\eta \sim 0.1$ and similar evolutionary histories for the two (56), the average observed ratio of stellar mass to that of SMBH's in galaxies of about 1000 (58) implies that only about 10% of the EBL intensity can be ascribed to AGN activity. Astrophysical processes in individual sources so far described are easily detectable with current imaging telescopes above the map background. A question however remains how much these imagers can detect of more diffuse emissions, like could take place from low-density regions in the outskirts of galaxies or even from stellar populations

distributed in the intergalactic medium: all these would easily sink onto the background, and possibly remain completely undetectable. Extreme occurrences of this kind might be decaying particles emerging from the Big Bang or early populations of stars, like the so-called Population III stars often invoked to explain the early metal enrichment in the Universe [(59), (60)]. EBL intensity is usually given in units of $nW\ m^{-2}\ sr^{-1}$. Its measurement can be done directly, a method that poses considerable challenges. It requires the removal of strong foreground emission from interplanetary dust particles and from stellar and interstellar emission components from the Milky Way. As seen in Fig. 3.1 the major component is the Zodiacal light, including both Sun scattered light by Inter-Planetary Dust particles, and their quasi-thermal emission peaking at 10 μm. Contributions by the integrated emission of faint stars and by high-galactic latitude dust (cirrus) are also indicated. Even outside the terrestrial atmosphere, these emissions are so bright compared to the expected level of the EBL (that is around 10^{-8} W/m^2/sr) that any attempts of a direct measure are prone to uncertainties.
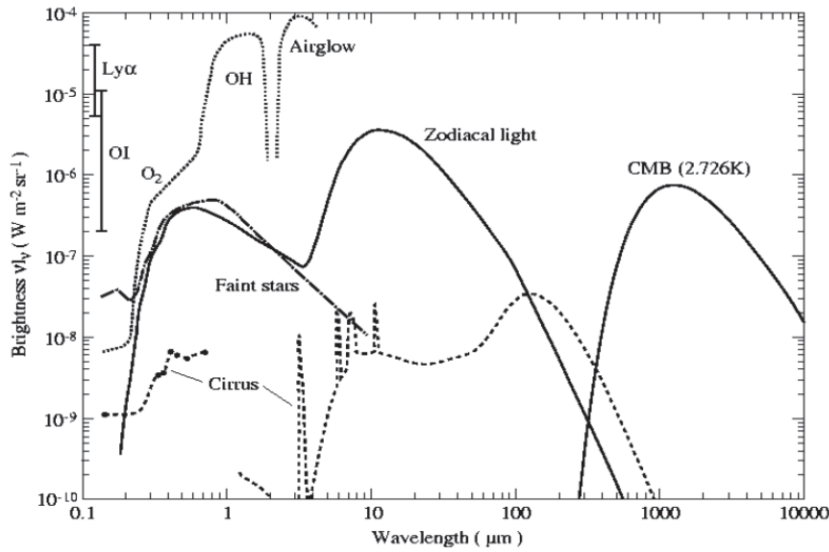
Figure 3.1: Overview of the various components of the total night sky background at high galactic and ecliptic latitudes. The Zodiacal Inter-Planetary Dust emission, Zodiacal scattered light, and starlight (bright stars excluded) are indicated. The interstellar (cirrus) emission is normalized to the minimum column density observed at high Galactic latitudes ($N_H = 10^{20}$ H atoms/cm^2). Atmospheric O_2 air glow and OH emissions in the near-IR, as well as the CMB, are also indicated. Taken from (61).

Nevertheless, thanks to the very sensitive instrumentation like Hubble Space Telescope and Spitzer from space and very large telescopes from ground, the baseline NIR-EBL is very well constrained and understood. For example, strict lower limits to the EBL intensity have been obtained by adding up the light emitted by resolved galaxies. Using data from HST, it was taken a solid angle portion of the sky

19

($50 \times 50 \ arcsec^2$) and they count the galaxies within that field for different wavelength bands. From this counts the EBL was calculated integrating the emitted flux times the differential number counts down to the detection threshold. This measurement is a lower limit since the low surface brightness regions of galaxies may be missed in the standard aperture photometry. Furthermore, a truly diffuse background will always remain undetected in such surveys. The same can be said for UV-optical wavelengths, where the EBL contribution is well constrained. In far-IR (5-300 μm), on the other hand, it is possible to distinguish two cases: before and beyond 100 μm. The total intensity observed, beyond 100 μm, is dominated by cirrus and CMB emissions. In this case the EBL can be safely extracted thanks to the a-priori knowledge of the CMB spectral intensity and the clear dependence of cirrus on Galactic coordinates. Instead, between 5 to 100 μm, the interplanetary-dust brightness and its weak dependence on the ecliptic coordinates (about a factor 2 from pole to equator) prevent it from being subtracted from the total sky maps. Thus, infrared telescopes from space can detect point sources, but are blind to diffuse emission, like extended halos of dust emission or truly diffuse processes, because of the huge background noise. For this reason, EBL is poorly constrained in the $\sim 5 - 60 \ \mu m$ wavelength region.

3.1 Modeling the EBL

Thanks to the variety of astronomical facilities, both from ground and from space, operative over the full wavelength range of 0.1 to 1000 μm, it is possible to set a reliable minimum boundary to the extragalactic radiation field from known sources, that in turn will set a minimal threshold to the cosmic photon-photon opacity. Many attempts have been published to model the known source contributions to the EBL based on the statistics of the multi-wavelength populations of galaxies and AGNs. The present-time EBL intensity can be obtained by the relation of the differential source number counts $N(S)$ [sources/unit flux-density interval], with the source flux density $S(v)$ [erg/s/Hz]:

$$I(v) = \int_{S_{min}}^{S_{max}} N(S) \ S \ dS \ \text{[erg/s/cm}^2\text{/sr]} \qquad (3.1)$$

or in the equivalent units of Watt/m^2/sr. N(S) is the immediate observable that can be obtained from a sky survey at frequency v. Instead, to estimate the opacity for a distant gamma-ray source, the intensity evolution with cosmic time must be considered. This approach is more complicated to take into account the progressive production of photons by the sources and their redshift effects. The EBL intensity in this case is:

$$I_{v_0}(z^*) = \frac{1}{4\pi}\frac{c}{H_0}\int_{z^*}^{z_{max}} \frac{dz\, j[v_0(1+z)]}{\sqrt{(1+z)^2[(1+z)^2(1+\Omega_m z)-z(2+z)\Omega_\Lambda]}} \qquad (3.2)$$

for a flat Universe with $\Omega_m + \Omega_\Lambda = 1$, with $j[v_0]$ the galaxy comoving volume emissivity:

$$j[v_0] = \int_{L_{min}}^{L_{max}} d\log L \cdot n_c(L,z) \cdot K(L,z) \cdot L_{v_0} \qquad (3.3)$$

L is the luminosity in [$erg/s/Hz$], K(L, z) is the K-correction, $K(L,z) = (1+z)L_{v_0(1+z)}/L_{v_0}$ and n_c the comoving luminosity function at the redshift z expressed in number of galaxies per Mpc^3 per unit logaritmic interval of the luminosity L at frequency v_0. The local background intensity as in eq. ($I(v)$) coincides with eq. ($I_{v_0}(z^*)$) for $z^* = 0$.

From eq. ($I_{v_0}(z^*)$), the photon differential proper number density [photons/cm^3/Hz] at the redshift z^* are given by:

$$\frac{dn_\gamma(\epsilon_0, z^*)}{d\epsilon} = \frac{4\pi}{c} \cdot I_{v_0}(z^*)\frac{1}{\epsilon} \qquad (3.4)$$

where $\epsilon_0 = hv_0$ is the photon energy.

In an attempt to constrain as much as possible the EBL flux density, both empirical and physical models have been created.

Physical models have been devised that predict the emissivity of cosmic sources based on a-priori physical treatment of their origin and cosmic evolution based on physical prescriptions. In particular, an approach of this kind was pioneered by Gilmore et al. (62), based on semi-analytic ΛCDM modelling of galaxy formation (63). An advantage of this is that the effects of different assumptions about the values of the cosmological parameters can be investigated, and that interpolations and, particularly, extrapolations outside the observationally constrained parameter space are physically motivated. A serious draw-back is that it is almost impossible by these means to achieve full compliance with the observational statistics and the model suffers rigidity to reproduce them. In a somewhat complementary fashion, the empirical models try to be as adherent as possible to the multi-wavelength observational data, including the source number counts, redshift distributions, and the redshift-dependent luminosity functions. The models here have to identify the main population components, like star-forming and quiescent galaxies, and Active Galactic Nuclei of various

categories, each one with its own statistical properties and, somehow physically motivated, redshift evolution. The latter are fitted with simple parametric functions, that are needed to interpolate binned and discretized data (like the redshift dependencies), and to extrapolate them to regions of the parameter space where they are not directly measured (like the luminosity functions at the lowest, unmeasurable, L). An important aspect about this approach and supporting it has been emphasized by Madau & Pozzetti (64): the observational number counts of extragalactic sources are so deep from the UV to the IR and cover such a large fraction of the flux-density range at the various λ in eq. ($I(v)$) that the contributions of sources below the flux detection limits give completely negligible contributions to EBL. The quality of these empirical models of the EBL then rests on their ability to offer precise fine-grade description of the data and the ability to account for all the available observational constraints. Models of this sort are discussed in particular in [(65), (66), (67), (68)]. In my thesis, to estimate the spectral contribution due to EBL, I used an empirical model known as Franceschini et al. 2017 (69). It is a backward evolution model which provides estimates of the EBL photon density using available information on the cosmic sources producing diffuse photons in the Universe from far-UV to the sub-millimeter wavelengths over a wide range of the cosmic epochs with the best possible time and spectral resolution and their redshift evolution. The proper photon density and redshift variation based on this model are reported in Fig. 3.2. This model exploits relevant data from the ground-based observatories in the optical, near-IR and sub-millimeter, as well as multi-wavelength information from the space-telescopes such as HST, ISO and Spitzer (*Spitzer* MIPS mid-IR data). Additional constraints are provided from direct measurements or upper limits on the EBL estimates by dedicated missions like COBE. Furthermore, in far-IR and submillimeter were used data obtained with the Herschel Space Observatory.
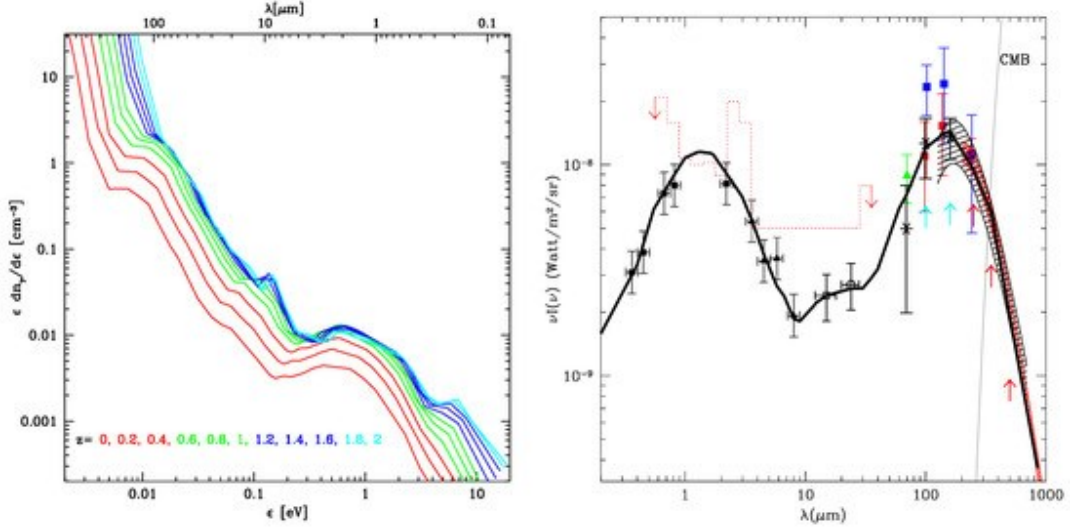
Figure 3.2: Left: the energy-weighted proper number density of EBL photons as a function of the energy ε. The various curves correspond to different redshifts, as indicated. The contributions of CMB photons appear in the fast rise below 0.01 eV. Right: the corresponding EBL spectral intensity (thick line). The data-points correspond to the integration of the known-source number counts as in eq. (3.1). Taken from (2).

As a consequence of the presence of such high-density diffuse background radiation, high-energy particles, both cosmic rays and photons, have a high chance of interaction. Gamma-ray photons, in particular, have a significant probability, increasing with energy, to collide with background photons and decay into an electron-positron pair:

$$\gamma_{VHE} + \gamma_{EBL} \longrightarrow e^- + e^+ \qquad (3.5)$$

hence essentially disappearing from view. Imagine the propagation of a monochromatic photon beam emitted by a blazar at redshift z and detected at energy E_0 within the standard ΛCDM cosmological model, so that the emitted energy E is $E_0(1 + z)$ owing to the cosmic expansion. Clearly, regardless of the actual physics responsible for photon propagation, the observed (Φ_{obs}) and emitted (Φ_{em}) differential photon number fluxes are related by

$$\Phi_{obs}(E_0, z) = P_{\gamma \to \gamma}(E_0, z) \, \Phi_{em}(E_0(1 + z)) \qquad (3.6)$$

where $P_{\gamma \to \gamma}(E_0, z)$ is the photon survival probability throughout the whole travel from the source to us. Within conventional physics the photon survival probability $P_{\gamma \to \gamma}^{CP}(E_0, z)$ is usually parametrized as

$$P_{\gamma \to \gamma}^{CP}(E_0, z) = e^{-\tau_\gamma(E_0, z)} \qquad (3.7)$$

where $\tau_\gamma(E_0, z)$ is the optical depth, quantifies the dimming of the source. Note that $\tau_\gamma(E_0, z)$ increases with z, since a greater source distance entails a larger probability for a photon to disappear from the beam. Apart from atmospheric effects, one typically has $\tau_\gamma(E_0, z) < 1$ for z not too large, in which case the Universe is optically thin up to the source. But depending on E_0 it can happen that $\tau_\gamma(E_0, z) > 1$, so that at some point the Universe becomes optically thick along the line of sight to the source. The value z_h such that $\tau_\gamma(E_0, z) = 1$ defines the γ-ray horizon for a given E_0, and it follows from Eq. (3.7) that sources beyond the horizon tend to become progressively invisible as z further increases past z_h.

 Once the source distance is known, a measure of τ_γ from a spectral fit depends only on the background photon density and some assumptions about the intrinsic spectrum. In general, the optical depth depends on the EBL photons density (n_{EBL}) along the line of sight and on the interaction cross section ($\sigma_{\gamma\gamma}$), according to the formula:

$$\tau(E, z_s) = c \int_0^{z_e} dz \frac{dt}{dz} \int_0^2 dx \frac{x}{2} \int_0^\infty d\mathcal{E} \frac{dn_{EBL}(\mathcal{E}, z)}{d\mathcal{E}} \sigma_{\gamma\gamma}(\beta) \qquad (3.10)$$

where $\beta \equiv \left(1 - \frac{4m_e^2 c^4}{s}\right)^{1/2}$, $s \equiv 2E\mathcal{E}x(1+z)^2$ and $x \equiv (1 - \cos\theta)$, with θ the angle between the momenta of two photons in the lab frame, and m_e the electron mass. For a flat Universe ($\Omega_m + \Omega_\Lambda = 1$):

$$\frac{dt}{dz} = \frac{1}{H_0(1+z)\sqrt{(1+z)^3 \Omega_m + \Omega_\Lambda}} \qquad (3.11)$$

where $\Omega_m \simeq 0.3$ and $\Omega_\Lambda \simeq 0.7$ are the density cosmological parameter associated with matter and cosmological constant respectively; and H_0 is the Hubble constant, whose currently estimated value (70) is around $67.4 \pm 0.5 \frac{km}{s\,Mpc}$. Despite it has sufficient energy, the gamma-photon cannot spontaneously generate electron-positron pair because this phenomenon would violate the photon moment and energy conservation law. Because EBL photon- γ photon interaction happened, it is necessary either some non-thermal plasma (which, however, we are unable to observe) or a low energy photon. In the latter case, defining with P_γ and P_{EBL} the momentum four-vectors of the gamma and the EBL photon, respectively:

24

$$P_\gamma = \left[E/c , E/c\, i_1 \right], P_{EBL} = \left[\mathcal{E}/c , \mathcal{E}/c\, i_2 \right] \tag{3.12}$$

where i_1 and i_2 are two imaginary versors indicating the direction of the two photons and such that $i_1^2 = i_1 \cdot i_1 = -1$ $(P_\gamma^2 = 0)$. Imposing the quadri-momentum conservation:

$$P_\gamma + P_{EBL} = P_3 + P_4 \tag{3.13}$$

$$P_\gamma{}^2 = P_{EBL}{}^2 = P_\gamma \cdot P_\gamma = P_{EBL} \cdot P_{EBL} = 0 \tag{3.14}$$

The interaction between the two photons of energy E and $\mathcal{E}$ produces an electron-positron pair only if the energy product of the two photons is of the order of the electron energy at rest square $(m_e{}^2 c^4)$:

$$E \cdot \mathcal{E} \geq \frac{2 m_e^2 c^4}{1 - \cos\theta} \tag{3.15}$$

Note that E and $\mathcal{E}$ change along the beam in proportion of $1 + z$. Putting $x \equiv \frac{h\nu}{m_e c^2}$, the cross section depends on the function:

$$x_\gamma x_{EBL} \geq \frac{2}{1 - \cos\theta} \tag{3.16}$$

The interaction probability therefore depends both on a threshold energy necessary for the process to take place and on the angle of interaction between the two photons. Therefore, for tail-on interaction $(\theta = 0)$ the pair production cannot take place. As can be seen in Figure 3.3, the maximum cross section is $\sigma_{\gamma\gamma} \approx \frac{\sigma_T}{5}$ at $\frac{x_\gamma x_{EBL}}{2} (1 - \cos\theta) \approx 2$. Just to have a reference, if we take a gamma photon, with frequency of $10^{27}\ Hz$ and $\theta = \pi$ (frontal collision), the cross-section peak corresponds to $\lambda_{EBL} \cong 5 - 20\ \mu m$.
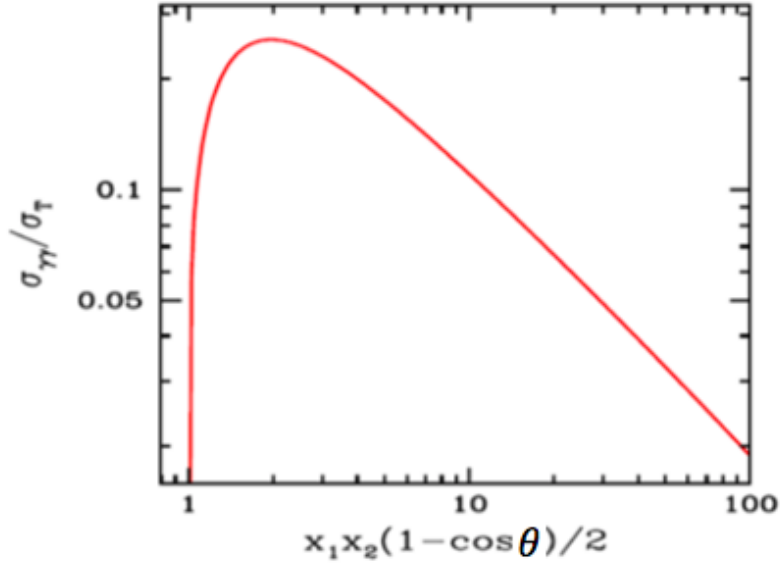
Figure 3.3: Photon-photon cross section as a function of $x_1 x_2 (1 - cos\,\theta)/2$.

Taking into account the EBL density (as z function) and the cross-section trend, it is possible to estimate, with eq. 3.10, the optical depth evolution as a function of redshift and the gamma photon energy (Fig. 3.4).
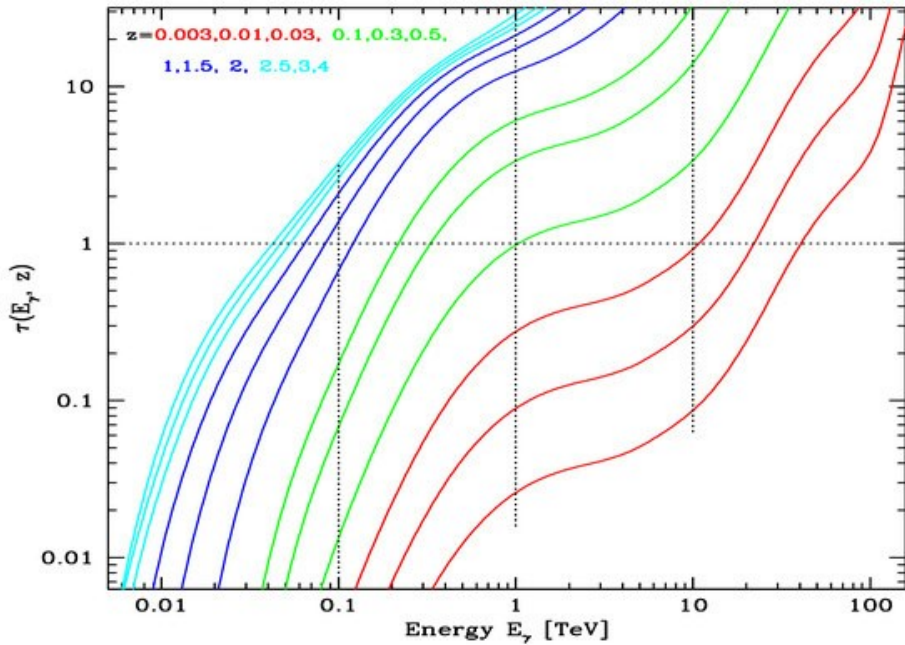
Figure 3.4: The optical depth by photon–photon collision as a function of the photon energy for sources located at $z =$ 0.003, 0.01, 0.03, 0.1, 0.3, 0.5, 1, 1.5, 2, 2.5, 3, 4, from bottom to top. The fast rise at the high τ and E_γ values is due to the large volume density of CMB photons. The graph is based on the model by (69) (54). Taken from (2).

From the plot in Fig. 3.4 it is also possible to see the contribution to the opacity coming from the high density of CMB photons, assuming a temperature of T = 2.738 K. This shows up as a fast increase of τ at high values of E_γ. From this figure it is very easy to understand why VHE observations are limited at high redshift. In fact, the optical depth associated with a photon of 1 TeV produced at redshift = 0.5 is approximately 6. In a context of classical physics (eq 3.7) this corresponds to a survival probability of $P_{\gamma \to \gamma}^{CP}(1 \text{ TeV}, z = 0.5) = e^{-6} \cong 2.5 \cdot 10^{-3}$. Clearly, farther the source is, lower is the survival probability. In this context, the reasoning on ALPs of the previous chapter is important. The photon is converted into ALP in the mixing phenomenon. During the ALP phase, there is no interaction between ALP and EBL: therefore, the photon optical depth decreases. So, it is possible to observe more distant sources because the emitted photons are less attenuated by the pair-production phenomenon.

Returning to the classical physics case, it would seem that the more energetic a photon is, the more likely it is to be absorbed: in reality this is not completely correct. In fact, up to $10^3 \ TeV$ this is exact but, observing at even higher energies (what could produce such photons?) the absorption decreases due to the cross-section function (Fig. 3.5).
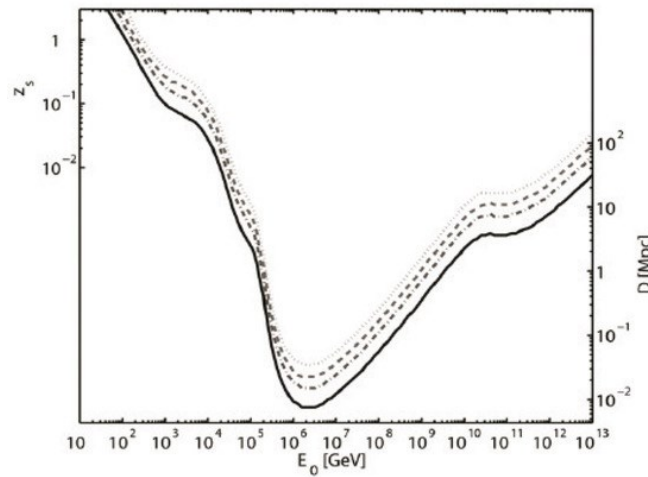
Figure 3.5: Graphical representation of the global photon–photon opacity. The graph shows the source redshifts z_s at which the optical depth takes fixed values as a function of the observed hard photon energy E_0; the y-scale on the right side shows the distance in Mpc for nearby sources. The curves from bottom to top correspond to a photon survival probability of $e^{-1} = 0.37$ (the horizon), $e^{-2} = 0.14$, $e^{-3} = 0.05$ and $e^{-4.6} = 0.01$. For $D > 8 \ kpc$ the photon survival probability is larger than 0.37 for any value of E_0. Taken from (2).

Absorption is maximum for photons of energy:

$$\varepsilon_{max} \cong 2(m_e c^2)^2 / E_\gamma \cong 0.5 \left(\frac{1\,TeV}{E_\gamma} \right) \qquad (3.16)$$

or in terms of wavelength:

$$\lambda_{max} \cong 1.24 \left(E_\gamma [TeV] \right) \mu m \qquad (3.17)$$

Hence, VHE γ-rays at a rest frame energy above 1 TeV are most likely absorbed by the mid and far-IR range of the EBL photons, while those in the 100 GeV to 1 TeV regime are sensitive to the EBL photons in the near-IR and optical bands. Below 100 GeV, it is mainly UV part of EBL-SED that causes the attenuation. Below 20 GeV, there is little absorption due to the increasing scarcity of the hard UV background photons. Thus, the attenuation of the VHE γ-ray photons by the EBL can in principle be used to estimate the EBL density at wavelengths corresponding to the observations of γ-rays from blazars at cosmological redshifts. This has been done in several studies with remarkable results. However, in this thesis, it was decided to take a further step: the observed spectra of the gamma sources were corrected, estimating the EBL with an established model (Franceschini et al. (54)). At this point I tried to understand how much ALPs may have changed the optical depth.

This chapter is mainly based on Franceschini's papers [(71), (69), (54), (72)].

4 Blazars and their VHE emission

Normal galaxies constitute the majority population of cosmic sources in the local universe. Although they may be quite massive (up to $10^{12} M_\odot$), they are not typically very luminous (never more luminous than $10^{11} L_\odot \sim 10^{44}\ erg/sec$). For this reason, normal galaxies have remained hardly detectable at very large cosmic distances for a long time, with recent advances mostly thanks to technological observational improvements.

For several decades, since the '60, the only detectable objects at large cosmic distances belonged to a completely different class of sources, which did not derive their energy from thermonuclear burning in stars. These are the Active Galactic Nuclei (AGN) and the galaxies hosting them are called active galaxies. An AGN is an object capable of generating extreme luminosity, that in some cases is 10^4 times the luminosity of the host galaxy, in a very compact region (probably $<< 1\ pc^3$, compared, for example, to the volume of the Milky Way that is of the order of $10^{12}\ pc^3$) (73). The radiation from this region can emerge over an extraordinarily broad range of frequencies. Apparently, the interest for the Active Galaxies as a population might seem modest, as in the local universe they make a small fraction of normal galaxies. However, their number increases considerably with increasing redshift.

There are four main categories of Active Galaxies and AGN: starburst, radio-quiet active nuclei (like optical quasar and Seyfert galaxies), radio bright active nuclei (like radio galaxies and radio quasars) and jetted active galactic nuclei (like Blazars).

Starburst galaxies are characterized by violent activity of star formation and an excess of infrared emission, selected in particular in the far-IR. Based on their bolometric luminosities, they are divided into three classes: $> 10^{11} L_\odot$ luminous (LIRG), $> 10^{12} L_\odot$ ultra-luminous (ULIRG), $> 10^{13} L_\odot$ hyper-luminous infrared galaxies (HYLIRG). To explain their star formation excess, these galaxies are believed to form by merging. The huge amount of dust present in these galaxies absorbs the intense radiation field produced by the stars, significantly decreasing the radiation pressure. For this reason, it is believed that in these galaxies auto-gravity takes over, favoring the formation of super massive black holes (SMBH) of $\sim 10^{10} M_\odot$. For this reason, starburst galaxies are currently believed to be the progenitors of the authentic AGN: radio-active nuclei. Unfortunately, observational verifications of the internal regions of starburst galaxies are very complex due to the obscuration by dust.

In the case of radio galaxies, the host galaxy turns out to be an early-type galaxy, that is an elliptical or S0 galaxy. The radio galaxies differ in two categories: radio-quiet and radio-loud. AGN radio loud, that are less common, emit most of their energy in a non-thermal way and have strong relativistic jets.

On the contrary the radio quiet, which represent the 85-90% of AGN, have mainly thermal emission. This subdivision could be due to different accretion states around the central BH or to the different spin of this. The spectra are similar between radio-loud and radio-quiet except concerning the radio emission, that in radio-quiet objects becomes almost negligible.

Radio-loud objects have emission contributions from both the jet(s) and the lobes that the jets inflate. These emission contributions dominate the luminosity of the AGN at radio wavelengths and possibly at some or all other wavelengths.
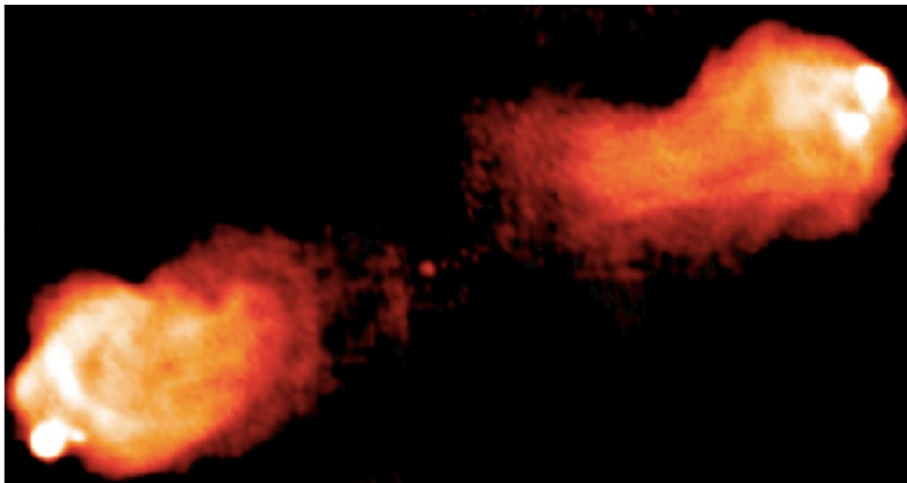
Figure 4.1: This image is a radio map (at a wavelength of 22cm) of the powerful radio galaxy Cygnus A, produced from observations at the Very Large Array by John Conway and Philip Blanco in 1994. The 2 x 1 arcminute image shows Cygnus A's famous double radio lobes, spanning over 500,000 light years.

For example at low radio frequencies ($\nu < 1\ GHz$) the two well separated lobes of the powerful radio galaxy Cygnus A in Fig 4.1, have radio spectra of power-law shape $S \propto \nu^{-\alpha_r}$, with $\alpha_r \sim 0.75 \pm 0.2$ (α_r being the radio spectral index), then consistent with what is predicted by the synchrotron theory. The optical galaxy counterpart of the radio source is typically situated at the center of a line connecting the two radio volumes. Often the radio volumes are related to a compact radio source by narrow radio bridges, named jets. Twin jets generated by the central accretion disc are shown in Figures 4.2. These beams, composed by hot and magnetized plasma, are extremely well collimated and can be extended on scales ranging from less than 1 AU to more than 1 Mpc.

Figure 4.2: Radio image of Cignus A with VLA, showing a radio jet linking the extended radio volumes and the central source.

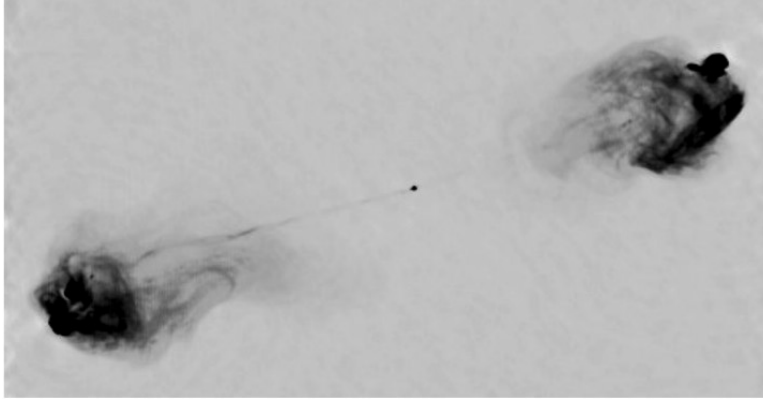The direction of the jet ejection is determined either by the angular momentum axis of the accretion disc or the spin axis of the black hole. The jet production mechanism and indeed the jet composition on very small scales are not understood at present due to the resolution of astronomical instruments being too low. The jets have their most obvious observational effects in the radio waveband, where very-long-baseline interferometry can be used to study the synchrotron radiation they emit at resolutions of sub-parsec scales.

In 1971 Martin Rees suggested, thanks to the discovery that the radio galaxies nuclei (and not just the lobes) also emit in radio band, that perhaps there was a single engine that powered these phenomena: a supermassive black hole, an object until then unthinkable, but which justifies the strong emissions detected. In fact, the black hole is the only astronomical object that has such a gravitational energy as can heat the gas to very high temperatures, so high to make it visible up to enormous distances.

The cold material close to a black hole forms the accretion disc. Dissipative processes in the accretion disc transport matter inwards and angular momentum outwards, while causing the accretion disc to heat up. The expected spectrum of an accretion disc peaks in the optical-ultraviolet waveband; in addition, a corona of hot material is formed above the accretion disc and can scatter photons for Inverse-Compton up to X-ray energies. The radiation from the accretion disc excites the cold atomic material close to the black hole and it radiates at particular emission lines. A large fraction of the AGN's radiation may be obscured by interstellar gas and dust close to the accretion disc, but (in a steady-state situation) this will be re-radiated at some other waveband, most likely the infrared. The compact radio emissions, coming from the galaxy center, show relatively flat radio spectra, with radio spectral indices $\alpha_r < 0.5$, and sometimes inverted spectra ($\alpha_r < 0$). There are two kinds of these flat spectra: spectra really flat and power-law shape (corresponding to low values of the energy spectral index, $p \sim 1$) are in particular associated to the category of radio-sources analyzed in this

31

thesis: the blazars; the second category are the spectra with multi-components, with evidences of self-absorption in systems of clouds emitting synchrotron with different particle densities (hence different radio optical depth). In this case we have spectra overall flat, but with many components. Observations based on radio imaging technique named Very Large Baseline Interferometry (VLBI) of the compact nuclear components have been performed with angular resolution down to millionths of arcsec, possible thanks to the very high surface brightness of these objects. It has been verified that on the smallest angular scales the same jet-like structures observed on the largest scales are found. The interpretation is that there should be a kind of "guns" inside the nucleus of these objects able to produce jets of plasma, particles and radiation extremely well collimated, able to transfer energy from the central source to the extended radio-volumes.

4.1 Non-thermal emission, gravitational origin

Radio-emitting Active Galactic Nuclei was the first evidence of relevant non-thermal emission by astrophysical sources and the existence of high-energy phenomena in the cosmos. That these emissions should be interpreted as phenomena involving non-thermal particles is indicated by the enormous values of the brightness temperature T_B ($\cong 10^{10} K$). T_B is the temperature that a black body should have to emit with a surface brightness I_ν:

$$T_B = \frac{c^2 I_\nu}{2k\nu^2} \qquad (4.1)$$

with frequency ν, light speed c and k the Boltzmann constant. The explanation is that these objects do not emit as black bodies, but their emission are synchrotron emissions due to ultra-relativistic electrons in a weak magnetic field. Nuclear emission occurs in fact from a small (unresolved) point region: the accretion disk ($\sim 10^{-2} pc$). This region is so small that it is not possible to interpret the enormous amount of radiant energy observed as due to a thermonuclear process. In fact, the fusion of hydrogen into helium presents an efficiency rate of conversion of matter into energy that is too low: $\Delta E \simeq 0.007 \, mc^2$.

The solution to explain the emission of AGNs is the transformation of gravitational energy into energy of particles and electromagnetic fields. The rate of efficiency with this method is highly dependent on the star compactness ratio ($\frac{M_*}{R_*}$):

$$\Delta E_{accr} = \frac{GM_*m}{R_*} \qquad (4.2)$$

In general, for a black hole we are in the order of 10%. This mechanism justifies, for example, the emission from the optician to the UV of quiet radio AGNs as due to the presence of an accretion disk around a non-rotating (or in any case weakly rotating) black hole. Radio-loud AGNs are instead interpreted as due to a strongly rotating accretion disk. The difference is due to the variation of the BH radius according to the rotation speed. In the case of BH strongly rotating the BH radius corresponds to the Schwarzschild radius ($R_S = 2\frac{GM_*}{c^2}$) while in the non-rotating case the last stable orbit of the gas correspond to $3R_{Schw}$. In addition, the efficiency of the central "engine" also depends on the angular momentum of the gas: in the case of gas rotating in the opposite direction of black hole, the efficiency is decreasing a lot ($\sim 5\%$). In the most efficient case possible, it will nevertheless never be possible to exceed a $\Delta E = 42\%$ corresponding to the Eddington limit since in this case the radiation pressure due to plasma is so great as to stop the growth itself. The matter fall in the accretion disk will accrete both the SMBH, producing an enormous amount of radiation, but will also accelerate the rotation of the BH itself. This justifies the evolution from quiet radio AGN to radio loud AGN in which relativistic jets are generated.

4.2 Blazar peculiar features

The last category of AGN are the blazars. These objects owe their name to a prototype object that was thought to be a variable star of the Lizard constellation: BL Lacertae (assumed to be about the thirtieth variable star of the constellation). About 10% of AGNs, besides accreting matter, are able to expel plasma in two oppositely directed jets. Their direction likely traces the rotational axis of a spinning black hole. The material inside these jets is moving at relativistic speeds. Therefore, the jet emission is highly beamed, and their appearance depends on the viewing angle. AGNs whose jets are pointing at us are called blazars. AGNs whose jets are pointing elsewhere are called radio–galaxies.

Unlike the other AGNs that have an inferred exponential spectral cut off at a few hundreds of KeV, blazars produce an extremely wide spectral energy distribution (SED) that extends from 10^7 to 10^{28} Hz. A typical spectrum is in Figure 4.3.
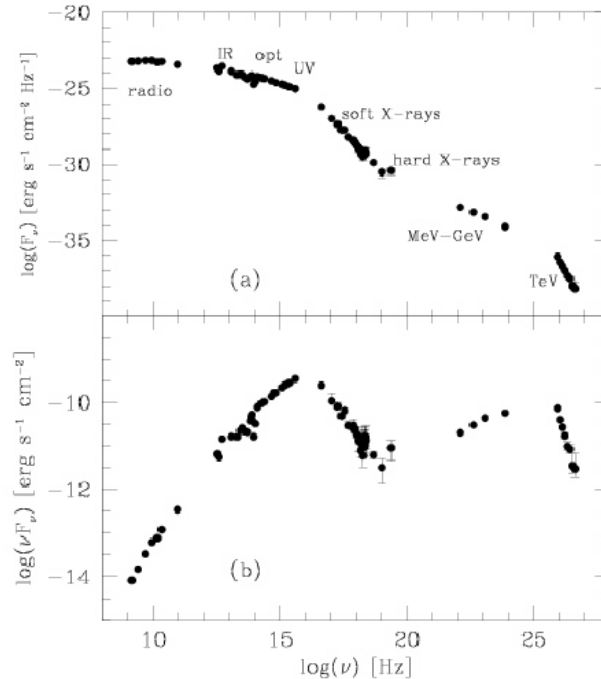
Figure 4.3: Broad-band spectrum of PKS 2155-304 ($z = 0.116$). Panel (a): spectral flux distribution from radio to TeV frequencies; panel (b): νF_ν representation of the spectrum, that emphasizes the frequencies at which most of the power is emitted. Taken from (74).

In general, the blazar spectrum, coming from a point-like object (not resolved), is well defined by a double power law. Indeed it presents two huge peaks: one between the millimeter and the soft-X (UV-X) and the other in the gamma band. These objects also show events of high variability (flash) approximately simultaneous to both peaks (this is due to the Synchrotron-Self Compton mechanism that powers the second peak). Although blazars are by nature thousands of times brighter than a normal galaxy these flashes can increase both intensity and spectral variability at all frequencies, from radio and optical (see e.g. (75), (76)) up to TeV energies (see e.g. (77), (78)), with daily to minutes timescales. Classic example is plot in Fig. 4.4, where the source flux grows 30 times in minutes.

Figure 4.4: Variability of PKS 2155-304 in 2007. Taken from (124).

While flux variability is common, and about a third of VHE AGN are only detected during flares. Most VHE AGN only show a factor of 2-3 in VHE flux variations with notable episodes (see e.g. (79)) of rapid minute-scale. On the contrary, large-scale (factor of 100) flux variations being very rare. It is worth noting that the observed time scales for these smaller variatio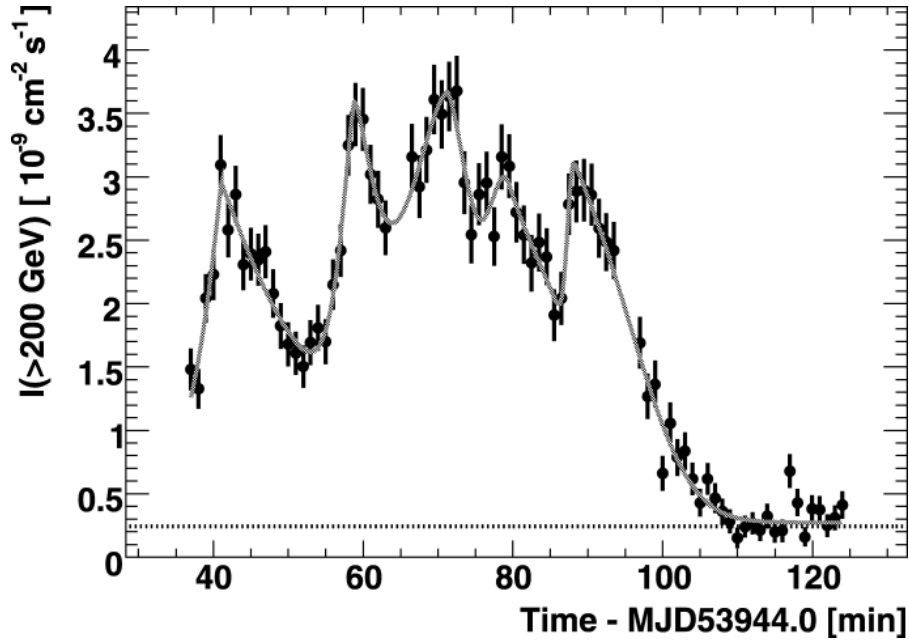ns (days to years) often depends on brightness of the objects in the VHE band, with shorter-duration variations only seen during isolated flaring episodes or for only the brightest objects. This could be a sensitivity effect, as many of the VHE AGN require long integration times for detection with current instruments. These astronomical objects therefore emit at $\nu > 10^{19}\,Hz$ but they make up a small slice of AGN ($1/10^4$ normal galaxies), i.e. 1‰ of radio-loud AGN. They are approximately 10^4 sources in all sky (71). This VHE photons reach energies up to 100 TeV, lower only than energy of cosmic rays (10^{20} eV = 10^8 TeV) and neutrinos. These energies are absolutely not comparable to current laboratory experiments (particle accelerators, 10 TeV) therefore the study of these sources guarantees an absolutely unique window on this spectral range.

Fossati et al. (1998) found that the spectral energy distribution shapes define a continuum of properties. The first peak (synchrotron) is anticorrelated with the source luminosity, moving from $\sim 10^{16} - 10^{17}\,Hz$ for less luminous sources to $\sim 10^{13} - 10^{14}\,Hz$ for the most luminous ones. Furthermore, the frequencies of the two peaks are correlated: the smaller the $\nu_{peak\ sync}$ the smaller the peak frequency of the high energy component. The X–ray spectrum becomes harder while the γ–ray spectrum softens with increasing luminosity, indicating that the second (Compton) peak of the

35

SEDs also moves to lower frequencies from $\sim 10^{24} - 10^{25} \, Hz$ for less luminous sources to $\sim 10^{21} - 10^{22} \, Hz$ for the most luminous ones.

Increasing $L_{5 \, GHz}$ increases the γ–ray dominance, i.e. the ratio of the power emitted in the inverse Compton and synchrotron components, estimated with the ratio of their respective peak luminosities. An extended version of the blazar sequence was presented by Ghisellini and Tavecchio (80) where additionally to the bolometric luminosity, the SED is linked to the mass of the black hole and the accretion rate.

About spectral features, the blazars with weak or absent optical spectral lines are named BL Lac objects, and the others received definitions that reflected their main properties: Optically Violently Variables, or Highly Polarized Quasars (e.g., (81)). More recently, the distinction within the blazar class was drawn between two types of objects: Flat Spectrum Radio Quasars (FSRQs) and BL Lacs. FSRQs present luminous broad emission lines, often accompanied also by prominent ultraviolet-optical continuum emission (blue bump) of thermal origin as normally seen in quasars. BL Lacs, where these broad emission lines are weak, with an equivalent width less than ~ 5 Angstrom [(82), (83)], or absent [(84), (85)]. Furthermore, a feature of FSRQs, which is not shared by BL Lacs, is the existence of a magnetized radio lobe with hot spots at the end of a jet. This distinction is reflected also in the radio polarization properties: at cm wavelengths BL Lacs tend to have polarization vectors nearly parallel to the jet, while in FSRQs the vectors cover a wider range of directions, favoring directions perpendicular to the jet [(86), (87)). Owing to these different properties, and in particular to the lack of a substantial thermal component (accretion disk and/or dusty torus), BL Lacs offer a more direct view into the primary energy-production mechanism, with respect to FSRQs.

BL Lacs differ in low (LBL), intermediate (IBL) and high (HBL) if synchrotron peak is at infrared ($\nu < 10^{14} \, Hz$), optical ($10^{14} < \nu < 10^{15} \, Hz$) or UV-X ($\nu > 10^{15} \, Hz$) frequency. While FSRQs are usually only low synchrotron peak objects. Different spectrum categories are illustrated in Fig. 4.5. It was initially supposed that BL Lacs represented the most extreme version of FSRQs, i.e. those with the most highly boosted continuum. Instead, it has been recognized later (e.g. (88)) that the amount of relativistic beaming and the intrinsic power in the lines are lower in BL Lacs than in FSRQs,

implying some intrinsic difference between the two classes. It seems that blazars SEDs form a sequence, according to their observed bolometric luminosity.

The high energy hump increases its relevance as we increase the bolometric luminosity. At low luminosities both humps have the same power, while the most powerful FSRQ have a high energy hump that is ten times the low energy one.

Nevertheless the continuity of several observational properties including the luminosity functions (89), the radio to X–ray SEDs (90) and the luminosity of the lines (91) suggests that blazars can still be considered as a single family.
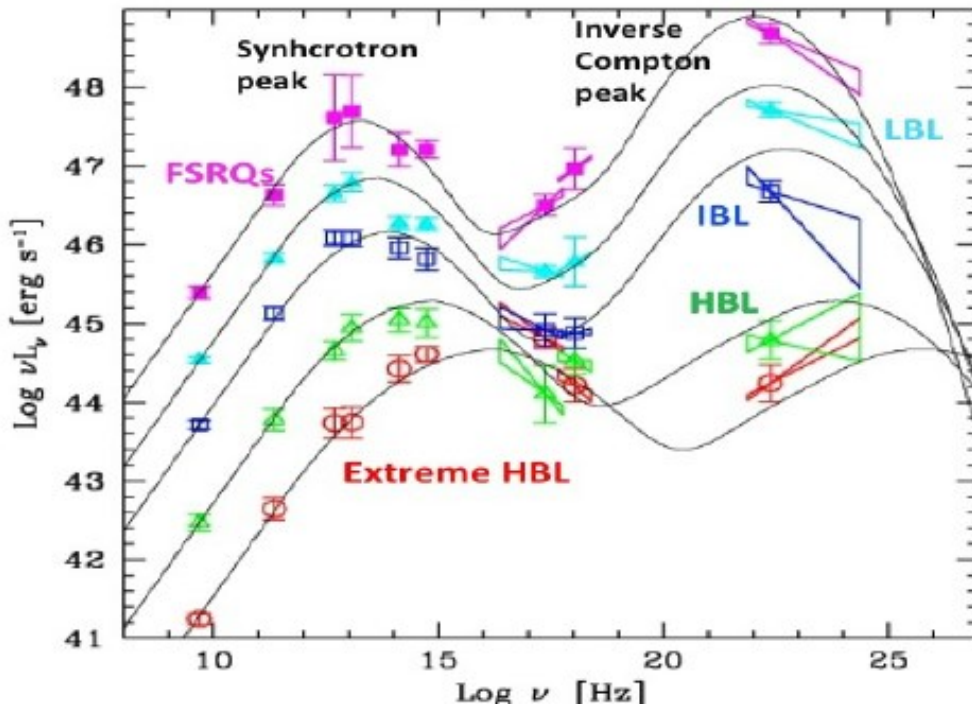
Figure 4.5: Overall spectral energy distributions of blazars. Note the differences of the relative intensities and frequencies of the two emission peaks for various types of objects. Taken from (74).

In Fig. 4.5, called blazar sequence, BL Lacs are the sources with lower luminosities and higher characteristic synchrotron and inverse Compton frequencies. The interpretation of this sequence is complex and somewhat controversial. The parameters that govern it are the cooling efficiency of the relativistic particles, the accretion efficiency and ultimately the mass of the central black hole: BL Lacs are those with lower efficiencies and lower masses [(92), (80), (93)]. A number of objects deviate at first glance from this scheme, having comparatively high total luminosities and high synchrotron peak frequencies [(85), (94)]. As previously mentioned, the central engine that powers the relativistic jet is assumed to be a rotating accreting black hole of about $10^8 M_\odot$. The mechanism

of energy extraction and particle acceleration along the jet is however not completely understood [see e.g. (95), (96)]. The dynamics of the jet may be rather complex and it has in some cases been interpreted in terms of helical structures tightly related to the black hole spin or to the orbital motion of a binary black hole system (97). On sub-parsec scales, jets are pervaded by magnetic fields of the order of 0.1-10 Gauss that may have tangled geometries and cause particles, leptons or hadrons, to radiate through the synchrotron mechanism.

BL Lacs are characterized by strong non-thermal emission at all frequencies. In the radio band, they exhibit bright (up to $10^{31}\ erg\ s^{-1}Hz^{-1}$, (98)), compact cores with power-law spectral continua with very flat shapes ($F_\nu \propto \nu^{-\alpha}$ with $\alpha < 0.5$), mostly produced by synchrotron radiation, often partially self-absorbed at the GHz frequencies.

At infrared-optical wavelengths the spectrum of BL Lacs also follows a power-law, when corrected for Galactic extinction and host galaxy contribution. The optical/near-infrared spectral indices are in the range $\alpha_\nu \sim 0.5 - 1.5$, i.e. they are steeper than in the radio (99). If the radio-to-optical spectrum is produced by the same optically thin synchrotron radiation component, the spectral steepening between these bands is naturally expected by increasing synchrotron losses at higher frequencies and adiabatic expansion of the jet plasma. The precise spectral slopes and their variability are also regulated by acceleration mechanisms and time-scales (100).

In the X-rays BL Lacs are powerful sources ($L_{1keV} \sim 10^{28} erg\ s^{-1}Hz^{-1}$), and in fact they were detected by many satellites in the last 45 years (e.g. (101)). The X-ray spectra are generally well described by single power-laws or curved slopes, depending on the emission mechanism. If this is synchrotron radiation, X-rays are generated by the highest energy electrons, so that the spectrum has a relatively steep spectral index ($\alpha\nu \sim 1.3$). If the cooling frequency (or break frequency) of the synchrotron spectrum is located in the X-ray range, the spectrum has a convex shape in this band. On the other hand, in a leptonic jet scenario (which it's favor with respect to the hadronic one), X-rays may be due to Compton up-scattering of lower energy photons by the same electrons that produce the synchrotron spectrum (synchrotron self-Compton), so that the X-ray spectral shape is flat ($\alpha_\nu < 1$). In BL Lacs where the synchrotron component peaks below the X-ray range, the X-ray spectrum is occasionally concave and joins smoothly with the high energy tail of the observed synchrotron spectrum.

The very fact that the jet being pointed to the observer may make the study of the jet morphology rather elusive. In the radio band, thanks to the high angular resolution, jet detection is possible and in fact a large fraction of objects classified as BL Lac show the signature of a jet, often with evidence of superluminal motion. The arcsec structures are well studied with VLA or similar instruments.

Radio jet sub structures are commonly detected with milliarcsec resolution when observed with the VLBI. At z ~ 0.1 one can thus explore structures down to parsec scale.

Some counterparts are found also in X-rays in Chandra images (angular resolution ~1 arcsec) at relatively high redshift. They are interpreted as a result of the Compton scattering cosmic microwave background photons off the most energetic electrons (102). Jet morphology in X-ray was studied in some details for a number of close-by BL Lacs, like PKS 0521–365 (103), and PKS 2201+044 and 3C 371 (90), which notably are systems where the beaming is supposed to be modest. On the other hand, the jet is rarely detected in the optical and near-infrared bands. This depends both on the more limited angular resolution with respect to the radio band and on the short lifetime of the high energy electrons producing the non-thermal emission of the jet. Because of the requirements on spatial resolution, in the optical and infrared the jet morphology was mainly studied with HST and with adaptive optics methods. A detailed study of the optical jet based on HST images was completed for PKS 0521–365, PKS 2201+04 and 3C 371 (104). The idea for the jets production is that the magnetic field is anchored to the plasma of the disk and it is more and more intense the closer you are to the black hole. This magnetic field comes from the galactic magnetic field which, by compressing the gas in the disk (in particular in the innermost parts of the disk), is substantially brought to the black hole interior limit. The black hole therefore has a magnetic field, necessarily treated by general relativity, which is propelled by the black hole itself. When the black hole rotates, it drags the magnetic field in a loop along the direction of the rotation axis of the black hole: the plasma is dragged by the lines of force of the magnetic field. It is like a corkscrew effect in which the magnetic fields (corkscrew) drag the plasma (cork). Since it is a magnetic field and not an electric filed, both positive and negative charges are carried out in both directions.

The absence of BL Lac emission and absorption lines involves serious problems in determining the redshift of the source. Only in epoch of low luminosity is possible to observe faint emission lines of the host galaxy. This is possible if the galaxy is sufficiently bright and close. Already for $z \gtrsim 0.8$ the host galaxy disappears due to cosmological beaming of surface brightness. In fact, the non-thermal continuum outshines both the superposed thermal contribution due to the stellar component of the host galaxy and the emission lines generated by fluorescence in clouds surrounding the central black hole, thus preventing to determine the redshift. Sometimes it is also possible to observe absorption lines of host galaxy if it is of the first morphological types. These galaxies have very little interstellar medium so only stellar absorption is observed.

Moreover, when spectral lines are detected, they are characterized by very small (few Angstrom) equivalent width and thus high-quality optical spectra in terms of Signal to Noise Ratio (SNR) and spectral resolution are required to reveal them.

Another method for obtaining redshift estimates is by photometry: considering the shift of the peaks towards the low frequencies as the brightness of the source increases. Considering these brightness fluctuations as pseudo regularities, it is possible to understand these objects as sample candles. The discovery of a number of BL Lac objects at z > 1 is fundamental to assess their luminosity function and cosmic evolution.

The lines lack is to be associated with a very particular issue process. Current theories envisage two hypotheses: hadronic and lepton emission. Hadronic emission involves heavy particles such as protons, neutrons, He nuclei and heavy nuclei. The interaction between a proton and a photonic field (interstellar cloud) produce pions and mesons with different charges. The neutral pion quickly decays into two very energetic photons: this mechanism explains, for example, the gamma emission of the Galaxy, in addition to non-thermal relativistic breemsstrahlung. The positive and negative pions instead generate pairs of neutrinos and a positron or an electron. This theory is currently the least credited for elucidating gamma emission associated with blazars. The lepton emission, on the other hand, involves light particles, especially electrons. In this case the emission mechanism that explains SED first peak is synchrotron, while the second peak is explained with Synchrotron Self-Compton. The synchrotron mechanism, due to the interaction of electrons with the intense magnetic field, is able to accelerate photons up to X-hard band (10^6 eV). The same electrons that produce this photonic field (typically in radio to UV) scatter the same photons they generated, increasing their energy up to gamma band. This is due to enormous electronic density that Inverse Compton scattering produce. However, few photons produced in first synchrotron peak are strongly pushed to higher energy. If the "soft" scattered photons originate from an external source, e.g. starlight or the microwave background, the mechanism is known as External Inverse Compton (EIC).

Current studies converge to support two main general paths by which the energy that is carried by a relativistic jet can be dissipated and made available for the acceleration of relativistic particles: for magnetically dominated jets (i.e., jets with a magnetization parameter σ > 1, where we define σ = $B^2/4\pi\rho c^2$, with B being the magnetic field and ρ as the plasma density) simulations show that a sizable part of the initial magnetic energy can be dissipated through (relativistic) reconnection, being easily triggered during the non-linear stages of jet instabilities (e.g., Kelvin–Helmholtz or current-driven kink instabilities). Particle- in-cell (PIC) simulations show that, in current sheets associated with magnetic reconnection, particles can be efficiently accelerated forming non-thermal energy distributions; for weakly magnetized flows, instead, the most likely dissipation sites are shocks, where the formation of non-thermal populations occurs through the classical diffusive shock acceleration (DSA) mechanism.

The observed radiation shows a degree of linear polarization of up to 30% from the radio band to the UV band (not measure in X-band yet), which agrees well with synchrotron emission. The apparent motions of the jets are superluminal: this is due to the relative motion projected into the sky, in which the emitting plasma blobs move at ultra-relativistic speeds towards the observer. From the radio interferometry observations, the velocity appears superluminal, of the order of 3-5 c and can be up to 20c (105). The plasma emission is fired in a direction that forms an angle θ with the line of sight. The jet sky projection (BC) is $vt_1 \sin \theta$, with v the jet speed and t_1 the light time spent to arrive from A to us (see Fig. 4.6). Focus is that plasma speed is very closed to photon speed: therefore, light time spent to travel from A to B is about the same as jet to coming to C. The light time coming from C to us (t_2) is the sum of t_1 and light travel time from B: $t_2 = t_1 + \frac{D - vt_1 \cos \theta}{c}$. In observer frame, transverse speed (on sky plane) is $v_{app} = \frac{vt_1 \sin \theta}{t_2 - t_1} = \frac{v \sin \theta}{1 - \beta \cos \theta}$ with $\beta = \frac{v}{c}$. Instead of β, Lorentz factor $\Gamma = (1 - \beta)^{-1/2}$ is often use.
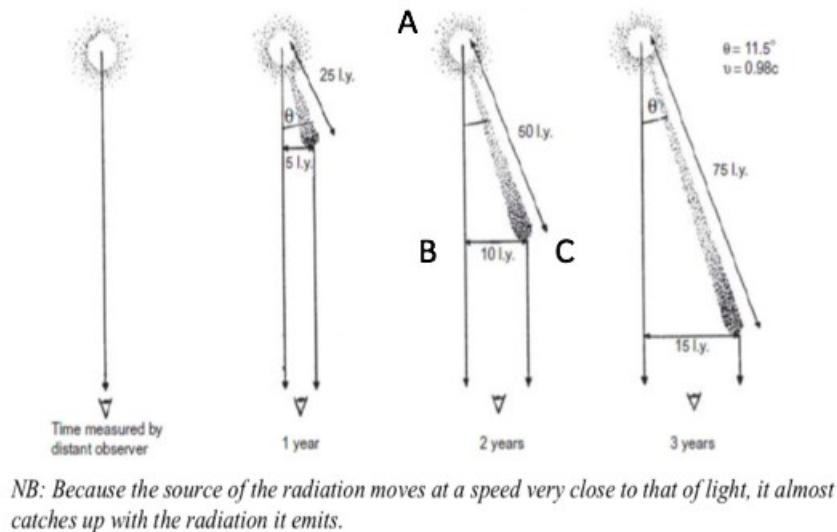
Figure 4.6: Superluminal motions scheme.

As seen in Fig. 4.6, plasma apparent speed is strongly dependent on its velocity and θ. If θ is high, jet and line of sight axes are not parallel therefore the relativistic effects are small. Instead if plasma velocity grows, the cloud apparent speed can also be ten! However, this is only one of several relativistic effects that modify the spectrum observed. The nucleus of these galaxies is absolutely similar to that of radio galaxies but due to the orientation the non-thermal emission of synchrotron and that of Inverse Compton are strongly amplified by the relativistic beaming effect. The brightness is so high, due to the beaming effects, that it dominates the brightness of

the entire galaxy hosting the blazar (explain the absorption lines absence). To take into account both the plasma speed and the observation angle, is used a factor that combines the two parameters: the relativistic doopler factor $\delta = \frac{1}{\Gamma(1-\beta\cos\theta)}$. Its evolution as a function of θ is reported in Fig. 4.7.
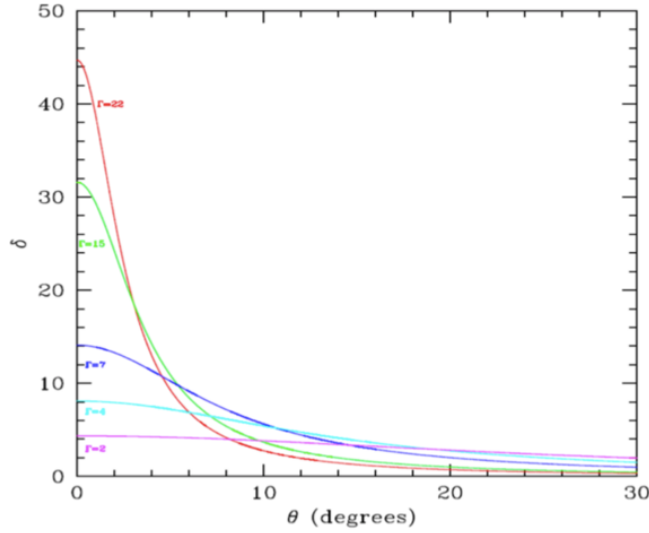
Figure 4.7: Evolution of relativistic doopler factor as a function of θ. Different colors correspond to different Lorentz factors.

If the jet is exactly in the line of sight ($\theta = 0°$) the relativistic doopler factor is $\delta \cong 2\Gamma$. As seen in plot, relativistic effects are negligible already for not so big angle ($\theta = 30°$). Indeed, the estimated viewing angles for blazar are $\theta \lesssim 10°$, where the plasma moves with a Lorentz factor Γ of the order of ~ 10, and occasionally as high as ~ 50. For small angles, however, the effect is enormous and modifies all observable quantities: blue-shifts the observed spectrum, foreshortens the observed time-scales, magnifies the luminosities at all wavelengths and modify also volume, intensity, emissivity, solid angle. The intrinsic values of these parameters can be obtained from the observational ones based on the following table:

Observed frequency:	$v = \delta \times v'$
Observed time-scale:	$\Delta t = {\Delta t'}/{\delta}$
Observed volume:	$V = \delta \times V'$
Observed solid angle:	$\Delta\Omega = \delta^2 \times \Delta\Omega'$
Observed emissivity:	$j(v) = \delta^2 \times j'(v')$

Observed intensity:	$I(v) = \delta^3 \times I'(v')$
Observed flux density:	$S(v) = \delta^3 \times S'(v')$

The jet modeling usually used is based on the relativistic doopler factor and not on the Lorentz factor: therefore, there will be a degeneration between θ and v. It is possible, for example, to break this degeneration with a morphological study. Analyzes of this type, based on the Synchrotron Self-Compton model, are able to describe well the two-peak spectrum for large values of δ.

An interesting question can be raised about the statistical properties of the blazar population, their number in comparison with other classes of AGNs and radio galaxies. Assuming that the peculiar properties of the population are due to the beaming effect and a random distribution of the source-intrinsic orientations, the fraction of blazars with respect to the total radio-galaxy population is simply given by a direction-integral:

$$\frac{N(\theta < \widehat{\theta})}{N_{TOT}} = \frac{\int_0^{\widehat{\theta}} d\Omega}{4\pi} = \frac{1}{4\pi} \int_0^{\widehat{\theta}} \sin\theta \, d\theta \, d\phi \approx \frac{1}{2\Gamma^2} \tag{4.4}$$

We may start considering if the parent un-beamed population are normal radio galaxies. Assuming differential number counts of radio galaxies as $dn/dS = 4\pi \cdot 300 \, S^{-2} \, (Jy^{-1})$, the total number of objects down to $0.001 \, Jy$ (about the flux limit above which normal radio galaxies dominate the counts statistics) would be approximately 3×10^6 all-sky, about 1% of which would show some blazar activity, or approximately 10^4 blazars all-sky. This is not inconsistent, for example, with the blazar statistics that we can infer from the Fermi all-sky survey, that has already discovered 3000 blazars. If we consider that the Fermi flux limits in gamma-rays are relatively shallow, the statistics are not inconsistent.

Beaming relativistic effect is also important to explain a particular effect: Compton catastrophe. In this case the energy density of radio photons is so high that most of the electrons energy losses are due to self-Compton Synchrotron rather than to synchrotron emission.

An electron in a plasma permeated by a magnetic field is subject to energy losses due to both synchrotron emission and Inverse Compton. For both processes there is an energy loss rate:

$$-\left(\frac{dE}{dt}\right)_{sync} = \frac{4}{3}\sigma_T u_B \beta^2 \Gamma^2 \qquad (4.5)$$

$$-\left(\frac{dE}{dt}\right)_{IC} = \frac{4}{3}\sigma_T u_\gamma \beta^2 \Gamma^2 \qquad (4.6)$$

where u_B and u_γ are the energy densities of the magnetic and photon-gamma filed, respectively. Instead σ_T is the Thomson cross section. The two equations have the same shape except for the energy field nature with which electrons interact. Comparing the previous relationships, assuming that in the electron frame $h\upsilon \ll m_e c^2$, we obtain regardless of the electron energy:

$$\eta = \frac{(dE/dt)_{IC}}{(dE/dt)_{sync}} = \frac{u_\gamma}{u_B} \qquad (4.7)$$

where η is the energy loss rates ratio of an ultra-relativistic electron for inverse Compton and synchrotron in the presence of radiation and magnetic fields. The energy losses for inverse Compton become important if η is greater than 1: in this case the radio photons produced by synchrotron are scattered at higher energies by the same relativistic electrons that emitted them. Consequently, as soon as η becomes greater than 1, electrons quickly lose their energy due to inverse Compton scattering by scattering photons at much higher energies, and the radio source thus becomes an extremely powerful source of X and γ-rays.

Let us consider a compact source of synchrotron radiation, such that radiation is self-absorbed. From the bolometric brightness in the radium we obtain the energy density of the radiation field, $u_B = B^2/2\mu_0$, where μ_0 is the magnetic permeability in vacuum, and consequently η is:

$$\eta = \frac{L_{IC}}{L_{sync}} = \left(\frac{T_B}{10^{12}K}\right)^5 \nu_9 \qquad (4.8)$$

where T_B is the brightness temperature, which constitutes the lower limit for the source temperature, and corresponds to the temperature of a black body that emits a flux S_ν equal to that measured for the object in question at a given frequency; thermodynamically, no object can emit radiation with a greater intensity than a black body at the same temperature. The critical brightness temperature for which $\eta = 1$ is:

$$T_B = 10^{12} \, \nu_9^{-1/5} [K] \qquad\qquad (4.10)$$

where ν_9 is the frequency in GHz at which the brightness temperature is measured. Based on this result, no compact radio source could have a T_B greater than $10^{12} \, K$ without being subject to catastrophic energy losses due to inverse Compton scattering. In fact, IC diffusion can take away large amounts of energy from electron, especially if second-order collisions become important, those in which a photon undergoes two consecutive interactions before leaving the source. This occurs, as previously mentioned, in compact sources in which the radiation energy density becomes comparable with the energy density of the magnetic field. Under these conditions, if the source electrons have a very high amount of energy, this will be quickly radiated by IC scattering. The catastrophe occurs when the object has a brightness temperature $T_B > 10^{12} \, K$.

The more compact sources, studied in the centimeter wavelengths with the VLBI, have $T_B \sim 10^{12} \, K$ therefore lower than the Compton limit. The Compton catastrophe had an important consideration with the discovery of the rapid variations that the radio flow of AGNs presents on a time scale of hours or days. The variability time scale is used to estimate the object physical size $D \sim c\Delta t$, the source light-crossing time. The object dimensions are therefore smaller than those measured by observations, leading to a brightness temperature value of the order of $10^{13-14} \, K$, greater than that provided by the Compton limit. The problem was solved considering the increase of the specific intensity due to relativist beaming.

This chapter is mainly based on Franceschini's High-Energy notes and (74).

5 The blazar sample and Cherenkov observations

5.1 Imaging Atmospheric Cherenkov Telescopes

Gamma-ray observations first became possible in the 1960s. These observations are much more problematic than X-rays or visible light detection, because gamma-rays are comparatively rare, even a "bright" source needing an observation time of several minutes before it is even detected, and because gamma rays are impossible to focus, resulting in a very low resolution. The most recent generation of gamma-ray telescopes (2000s) have a resolution of the order of 6 arc minutes in GeV range (detecting the Crab Nebula as a single "pixel"), compared to 0.5 arc seconds seen in low energy X-ray (1 keV) range by the Chandra X-ray Observatory (1999), and about 1.5 arc minutes in high energy X-ray (100 keV) range seen by High-Energy Focusing Telescope (2005). Lower energy photons (HE), between 0.2 and 200 GeV, are detected with direct observations. In 2008 the Large Area Telescope (LAT) on board the Fermi mission was launched in orbit for the investigation of this spectral range. However, in very high energy range (VHE: above 100 GeV) the observation technique is completely different, working with a collaboration of ground-based Imaging Atmospheric Cherenkov Telescopes (IACTs). LAT could also observe at VHE, but the difference is due to the detection area. In fact, the photon flux decreases according to a power law as energy increases. VHE photons are extremely energetic but rare ($\mathcal{O}(10^{-11})$) photons per cm^2-second (a few photons per m^2-year) above 1 TeV for strong sources), so we needed a huge photon collector, but LAT's dimensions are $1.8\,m \times 1.8\,m \times 0.72\,m$. The most interesting case is using the entire atmosphere, above a certain site, as a photon collector. The Cherenkov telescopes try to do that: not detecting gamma-rays "directly" but the optical-UV Cherenkov signal of the shower generated by gamma photons. There are three operating IACT systems: High Energy Stereoscopic System (H.E.S.S.), Major Atmospheric Gamma Imaging Cherenkov Telescopes (MAGIC) and Very Energetic Radiation Imaging Telescope Array System (VERITAS), which have detected blazars out to redshift $z \simeq 0.9$ and reach energies at most up to $\mathcal{O}(10\,TeV)$. The technical characteristics of major VHE telescopes are illustrated in appendix. MAGIC is an array of two telescopes with a large surface (17 meters of diameter) in Canarias island. Together with VERITAS, they cover the northern hemisphere. Indeed, HESS in Namibia detects the photons coming from the Milky Way bulge and the other sources of southern hemisphere. HESS and VERITAS are both made up of four 12 meters optical reflectors each. In 2012 HESS also had a fifth 28-meters telescope positioned in the center, which allowed to lower the observation threshold to 20 GeV.

The IACTs AGN program focuses on making precision measurements of their VHE spectra and variability patterns, while leveraging contemporaneous multi-wavelength (MWL) observations from both ground, and space-based facilities. The main component is a long-term study of the existing VHE blazar population in a manner that emphasizes the regular search for, and intense observation of, major flaring episodes. Independent of any successful flare identification, the regular sampling of each blazar aims to build high-statistics data sets to enable fully-constrained modeling of each VHE blazar's SED. The long-term MWL light curves should also allow for flux and spectral correlation studies that may indicate commonalities in the origin of each AGN's emission. IACTs AGN studies are also useful for a variety of cosmological measurements and have been used to constrain the strength of the intergalactic magnetic field and the EBL density.

5.2   Sample at VHE

Until 1996 only three VHE sources had been identified: the supernova remnant NGC 1952 (Crab Nebula) and two blazars very close to us (Markarian 421 and Markarian 501, $z = 0.0308$ and $z = 0.034$ respectively). After reaching over 100 sources in 2011, almost 250 sources were reached today also thanks to the HESS upgrade. Of these, about 19% are pulsars, 11% are supernovae and there are also 11 binaries and 6 Gamma Ray Bursts (GRBs). In addition, there are also 75 unidentified. The main emitting sources at VHE are blazars (32%). As seen in the previous chapter, blazars differ according to their energy spectrum in two different categories: FSRQ and BL Lac. By observing the image in Figure 5.1 you can see the distribution in the sky of the sources differentiated according to their classification (TeVCat catalogue[3]).
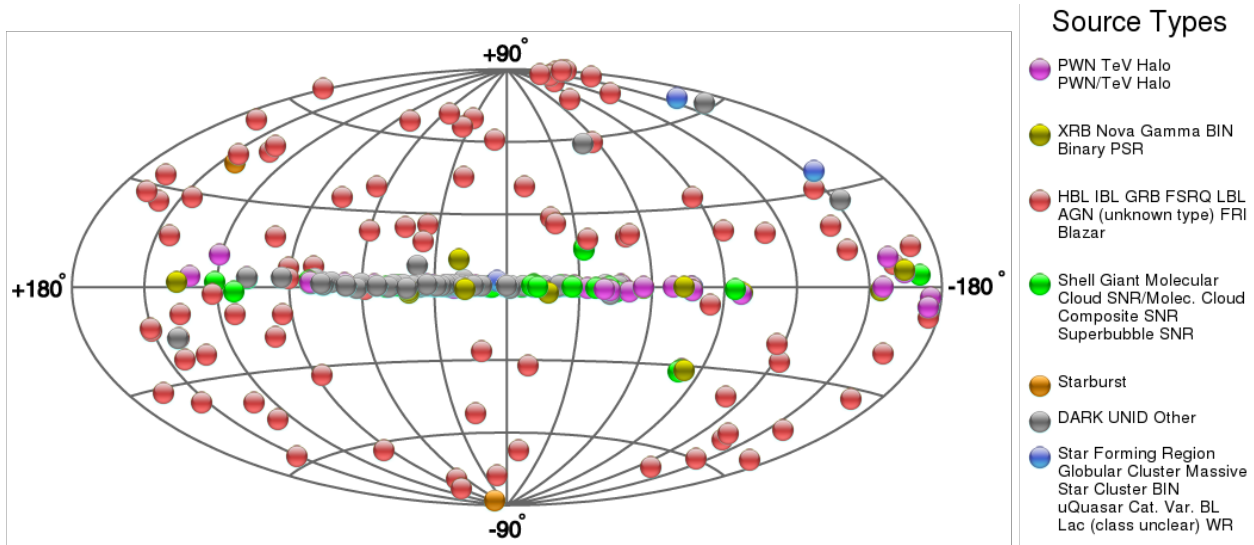
---

[3] http://tevcat.uchicago.edu

Figure 5.1: Sky map of VHE objects. Taken from TeVCat.

The blazars well classified (FSRQ, HBL, IBL and LBL) are illustrated in red. The other source types are indicated in legend. Over 60 BL Lacs objects have been detected by IACTs, only about 8 FSRQs are known to emit in this energy range. Among BL Lacs, 55 are classified as HBL, 10 like IBL and 2 like LBL. Furthermore, there are 5 objects whose blazar sub-classifications are uncertain. The VHE blazar catalogue covers a redshift range from $z = 0.030$ to $z = 0.944$, noting that ~80% of the objects have either $z < 0.3$ or uncertain redshift. The general proximity of these objects is due to a combination of energetics requirements and the effects of the extragalactic background light which attenuates VHE photons in an energy, and distance, dependent manner.

Also the observations conducted in the MeV-GeV range from satellites (first the Compton Gamma-Ray Observatory in 1991-2000 and recently the orbiting Fermi Gamma-ray Satellite and AGILE), that are less disturbed by EBL, detected large numbers of extra-galactic sources that turned out to be blazars, with very few exceptions. Among the associated blazars in the Fermi-LAT Fourth Source Catalog (4FGL) there are 694 FSQs compared to 1131 BL Lac objects. There are a few probable reasons that contribute to the difference between the BL Lac-FSRQ ratio detected at HE and VHE. As seen in the previous chapter, the peak of the gamma-ray emission in the spectral energy distribution of FSRQs is usually shifted to lower energies compared to BL Lac objects. Also, some of the source may have enhanced internal absorption in the radiation field of the Broad Line Region via e^+e^- pair production process.

The sources observed so far at VHE are limited due to a lot of intrinsic problems: the strong variability of the sources ($\sim 1/3$ visible only during flare), the gamma-photon interaction with EBL and the small intrinsic amount of sources. Also there are some observative problem due to the small field of

view of the IACTs. However, a follow up approach is widely used to study the VHE gamma-ray emission from blazars: it consists of alerts of enhanced activity at lower frequencies with instruments with greater field of view.

To understand how Cherenkov telescopes work, it is necessary to take a step back and understand, thanks to theory, what happens when ultra-relativistic particles and VHE photons enter in atmosphere.

5.3   Interaction between gamma photon and atmosphere

The gamma ray path is not very quiet but it is rich in interactions both with matter and with other photons. As seen in chapter 3, the photon-photon interaction typically occurs in the path between the emitting source and the entry into the atmosphere. The gamma photons - matter interaction typically occurs in the upper troposphere (10 km). This last interaction, in addition to the photon energy variation, differs if the interaction occurs with electrons or with the nuclei of the medium. If the photon has relatively low energy (<1 MeV) and interacts with an electron, there can be two effects: the photon can be absorbed by the electron and disappear, releasing an electron (photoelectric effect) or transferring part of the energy to the electron (Compton effect). More energetic photons usually interact with the atomic nucleus field by generating an electron-positron pair (pair production).

The number of photons that have not interacted as a function of the depth of penetration (x) into the material is equal to $N(x) = N(0)e^{-\mu x}$. The absorption coefficient μ (probability of interaction per unit of length) is given by the product of the number of atoms per unit of volume, N, and the cross section σ: $\mu = N\sigma$. In case of photons the cross section σ is given by the sum of different contributions: photoelectric (σ_{pe}), Compton (σ_C) and pair production (σ_{pair}) cross sections; therefore the total absorption coefficient can be expressed as sum of the absorption coefficients relating to the various reactions: $\mu = \mu_{pe} + \mu_C + \mu_{pair}$. However, as seen in Figure 5.2, already for $E > 10 \, MeV$ the pair production absorption coefficient is dominant.
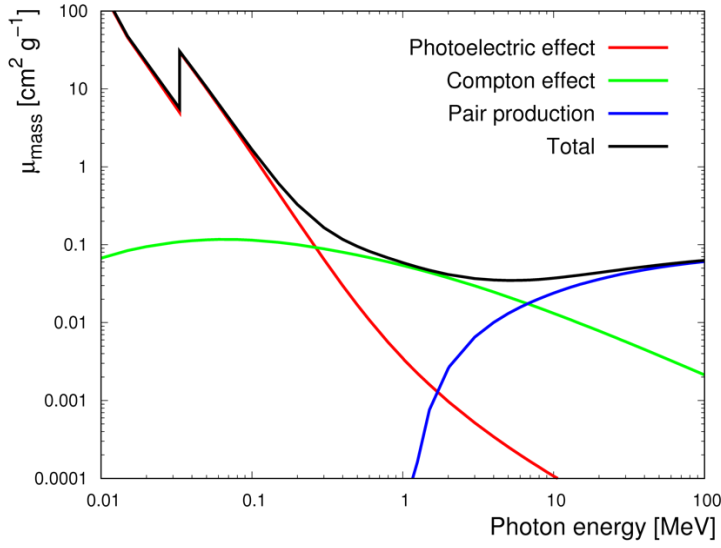
Figure 5.2: Contribution of photo-electric effect, Compton scattering and electron-positron pair production, to obtain the total absorption coefficient for X-rays and γ-rays. Taken from (106).

Pair production, also known as photonuclear effect, occurs for photons with energy greater than 1.022 MeV ($E\gamma > 2\,mc^2$), corresponding to the mass of two particles that are generated by the phenomenon. This phenomenon cannot take place in a vacuum because the invariant mass of the system would not be conserved (zero that of the photon, greater than $2\,mc^2$ that of the electron-positron pair). It is therefore necessary to have a nucleus (but an electron is also enough) to absorb the impulse excess. However, the cross section for the creation of pairs through interactions with electrons is very much smaller. All the energy beyond the 1.022 MeV threshold is equally distributed between the two particles in the form of kinetic energy.

The cross section for pair production at VHE:

$$\mu_{pair} = \frac{7}{9} L_R^{-1} \qquad (5.1)$$

with L_R the radiation length: a rather complex parameter that depends on the characteristics of the medium itself (density, atomic weight and atomic number). A beam of high energy photons therefore attenuates exponentially according to a characteristic length μ_{pair}^{-1} and therefore a photon has a conversion probability equal to $(1 - e^{-\mu_{pair} \cdot x})$ in crossing a material of thickness x.

When electromagnetic radiation passes through different medium, its behavior varies according to the value of a parameter: the refractive index of the medium n_r. This index determines how much the

path of light is bent, or refracted, when entering a material. The interaction between the light and the medium reduced the speed of propagation of the light:

$$n_r = \frac{c}{v_f} \qquad (5.2)$$

where c is the speed of light in vacuum and v_f is the phase velocity of light in the medium. Nothing can travel faster than the speed of light in a vacuum ($n_{r,vacuum} = 1$), but in a medium with refractive index higher than 1, it can be surpassed. Indeed, light travels 0.03 percent slower in air so ultra-high energy particles can travel faster than light in air. According to the theory of relativity, no information can travel faster than the speed of light in vacuum, but this does not mean that the refractive index cannot be less than 1. The refractive index measures the phase velocity of light, which does not carry information. The phase velocity is the speed at which the crests of the wave move and can be faster than the speed of light in vacuum, and thereby give a refractive index below 1. This can occur close to resonance frequencies, for absorbing media, in plasmas, and for X-rays. In fact, for medium constituted by free-to-move charges, the refractive index is strongly linked to frequency:

$$n_r = \sqrt{1 - \left(\frac{w_P}{w}\right)^2} \qquad (5.3)$$

where w_P is the medium frequency (plasma for example) and w is the radiation frequency. In this case the only way to observe the radiation after the crossing is if $w > w_P$. Because if $w < w_P$, the interaction radiation-medium is so strong that the refraction index became negative. This means that the radiation is completely reflected and cannot cross the plasma. Linked to the phase velocity is the group velocity: that is the velocity of the wave packets for a multi-frequency signal.

$$v_{group} = v_f - \frac{\partial n}{\partial k} \frac{ck}{n^2} \qquad (5.4)$$

with k the wave vector. Except for the vacuum, $\frac{\partial n}{\partial k}$ is always greater than zero (dispersive medium): however, the phase velocity is always higher than the group velocity.

As an example, the radiation emitted by a pulsar covers a large range of spectral frequencies: in this case the photons at different frequencies travel through the plasma at different speeds. The observed pulsation spectrum is therefore scattered. In the X-ray regime the refractive indices are lower than but very close to 1 (exceptions close to some resonance frequencies). As an example, water has a

refractive index of 0.99999974 for X-ray radiation at a photon energy of 30 keV (0.04 nm wavelength).

In the case of a continuous medium in which the electrons are not free to move but can only oscillate at a certain frequency (bound stage) the electromagnetic radiation will have different characteristics depending on the molecules that make up this medium. For this kind of medium, called dielectric medium, the refraction index is typically greater than one. Therefore, for formula 5.2 the speed of radiation in this medium is smaller than c. Thus, an ultra-relativistic particle could enter the atmosphere at a faster speed than light.
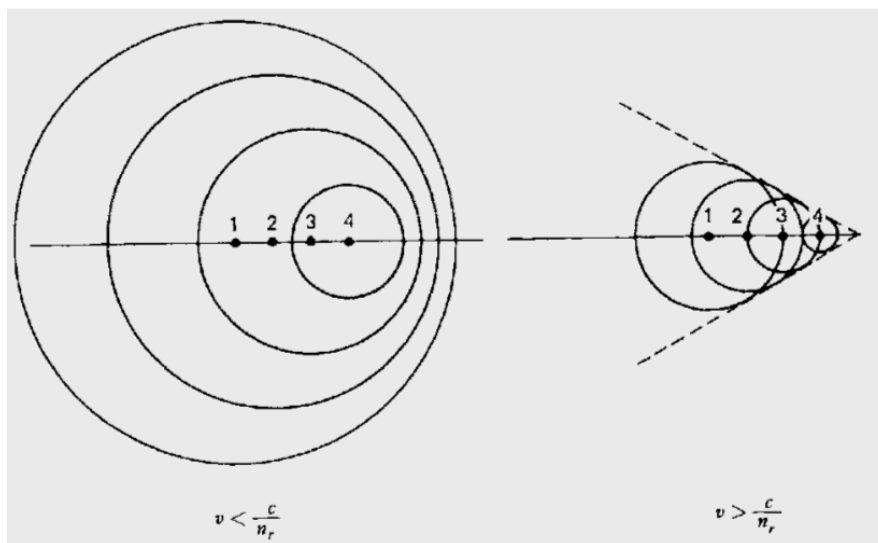
Figure 5.3: Propagation of wave fronts generated by a particle moving with velocity v through a dielectric medium.

If the particle passing through the medium is charged it generates an electromagnetic field that polarizes the atoms of the medium itself. Since positrons and usually cosmic rays (they are atomic nuclei) are positively charged, polarization deforms atoms by bringing their electrons closer to the charged particle (for extra-atmospheric electrons it will be clearly the opposite) (Fig. 5.4). As mentioned, this polarization field will have different speeds depending on the refractive index of the medium. Once out of the polarization field (as the charged particle moves away) electrons tend to return to their equilibrium position by emitting photons. This happens only if the medium is bound stage, since by conducting medium the electrons return to equilibrium without emitting photons. Under normal conditions ($v < c/n_r$) the polarization has spherical symmetry and the emitted photons interfere destructively, so no radiation is observed. Instead, in superluminal conditions ($v > c/n_r$), like for a cosmic-ray (10^{20} eV) or electrons/positrons ultra-relativistic, the charged particle

is faster than the polarization field, so the medium is polarized only "behind" the particle. The angle of the polarization cone obviously depends on the speed of the particle ($v_p = \beta\, c$) and the refractive index:

$$\cos\theta = (\beta\, n_r)^{-1} \tag{5.5}$$
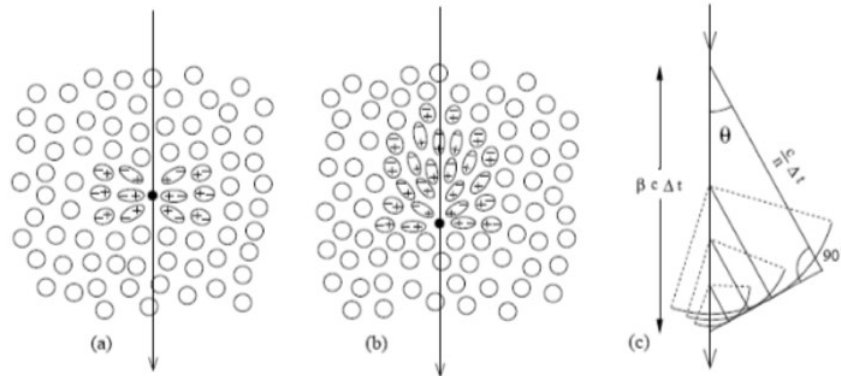
Figure 5.4: Interaction between a charged particle and a dielectric medium. In (a) a particle with $v < {}^c/_{n_r}$, in (b) a supeluminal particle $v > {}^c/_{n_r}$. In (c) a geometrical illustration of the phenomenon.

Therefore there is no more spherical symmetry, so the produced radiation is observed at a bluish-UV frequency, from 5000 to 1000 angstroms, called Cherenkov radiation (discovered by Russian physicist Pavel Cherenkov in 1934). This radiation is not directly produced by gamma photons but by electrons and positrons interaction, generated by pair productions, with the atmosphere. Since Cherenkov radiation is at much lower frequency, it is much more easily observable than direct gamma observation.

The process is actually even more complex: after the first pair production, electrons and positrons will interact with low energy surroundings light by inverse Compton:

$$e^-_{ultra\ \text{relativistic}} + \gamma_{low\ energy} \Longrightarrow e^-_{low\ energy} + \gamma_{VHE} \tag{5.6}$$

The gamma photon produced will interact again with medium: results are cascades of subatomic particles also known as air or particle showers. This process is called: electromagnetic shower. The number of photons (or electrons) produced is proportional to initial energy of the gamma ray. A similar process, which interests cosmic rays coming from space, is called hadronic shower. The path

between the pair production and the next will be of the order of the radiation length L_R (eq. 5.1). The products of these processes have less and less energy as the number of generations increases. When the electrons reduce their energy below the critical energy, the energy losses by ionization will dominate, and the cascade will stop.

Then Cherenkov emission is due to molecular dipoles generated by the interactions between ultra-relativistic electrons and positrons, formed for pair production, and medium. The propagation cone of the cascade is more or less one degree at 10 km of altitude. The light is spread over a large area (250 m in diameter) at the ground-base. With a single telescope it is difficult to reconstruct the exact geometry and trace the energy of the primary gamma photon. Therefore, to improve the angular resolution, the stereoscopic technique is used, i.e. the same event is observed from different angles using multiple telescopes. By combining the images obtained, it is possible to trace the trajectory of the swarm of particles and then define axis and vertex of the Cherenkov cone, essential data for determining gamma photon energy and direction of arrival. Furthermore, using different telescopes increases the detection range. Hess, for example, covers a field of view of ~ 5 ° with angular resolutions of ~ 0.1 °.

Cherenkov radiation has often been called Cherenkov flash because the emission time is of the order of few billionths of second. Therefore, high-speed cameras are needed to detect the flash.
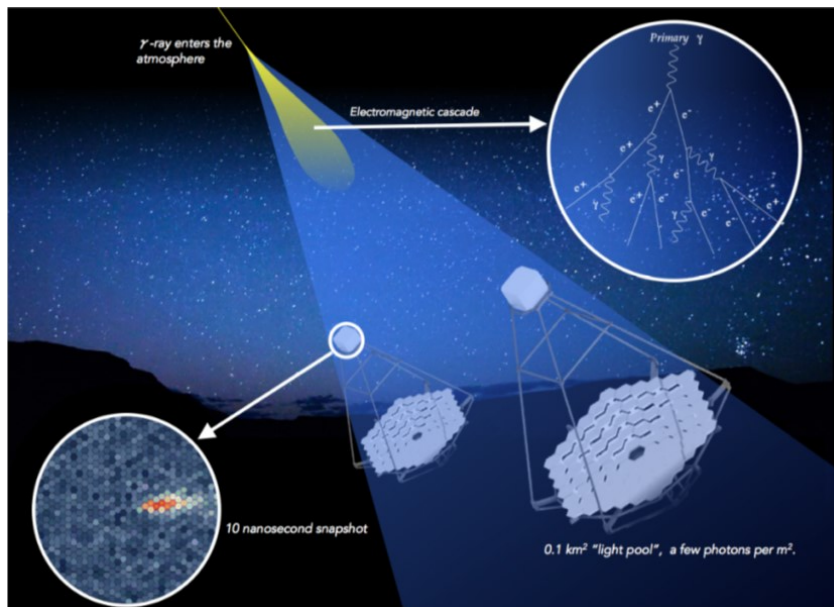

Figure 5.5: Illustrative image of a γ-photon path as it passes through the atmosphere. Taken from (107).

Given the significant developments in this energy band, Cherenkov Telescope Array (CTA) will be the next generation ground-based observatory for gamma-ray astronomy at VHE. This project will be the world's largest and more sensitive high-energy gamma-ray observatory. Building on the technology of current generation ground-based gamma-ray detectors, CTA will be ten times more sensitive and have unprecedented accuracy in its detection of high-energy gamma rays. Current gamma-ray telescope arrays host up to five individual telescopes, but CTA is designed to detect gamma rays over a larger area and a wider range of views with more than 100 telescopes located in the northern and southern hemispheres and a detection area. The size of the mirrors is important for tracking gamma photons of different energy. In fact, telescopes of different sizes are used to optimize signal collection: for example, for CTA will be used three classes of telescope types to cover the full CTA energy range (20 GeV to 300 TeV). For its core energy range (100 GeV to 10 TeV), CTA is planning 40 Medium-Sized Telescopes with diameter of 12 meters and a field of view of about 8 degrees. Furthermore, eight Large-Sized Telescopes (23 meters diameter) are planned to extend the energy range below 100 GeV because photons of weaker intensity are detectable only thanks to larger telescopes since this radiation will emerge little compared to the diffuse atmospheric radiation. On the contrary, growing in energy, the Cherenkov flash becomes more and more intense so the size of the telescope can decrease. For this reason, also 70 Small-Sized Telescopes with diameter of 4-5 meters, that observe above few hundreds TeV, are planned.

As for the distances between the telescopes, because the observed photons decrease a lot as the energy increases, it is convenient to increase the spacing to increase the signal collection area (however, taking into account the field of view). The exact spacing tends to be uncritical within a range of $\sim$ 70 m to 150 m.

As said, both gamma photons and cosmic rays generate particle showers. Fortunately, the cosmic rays, which are much more frequent (γ_{VHE} from the Crab Nebula $\leq$ 1/1000), produce a signal much more strewn on the camera: diffuse and incoherent (Fig. 5.6). The gamma-photons produce a well collimated signal, which depends on the inclination of the source with respect to the telescope axis (if the source were exactly on axis you would see a dot, at most a little strewn). If the source is a little off-axis you see a kind of cigar.

For every single signal from a source you get: if the signal coming from a gamma-photon or a cosmic-ray, the particle direction and its energy. So, you can obtain the source spectrum.
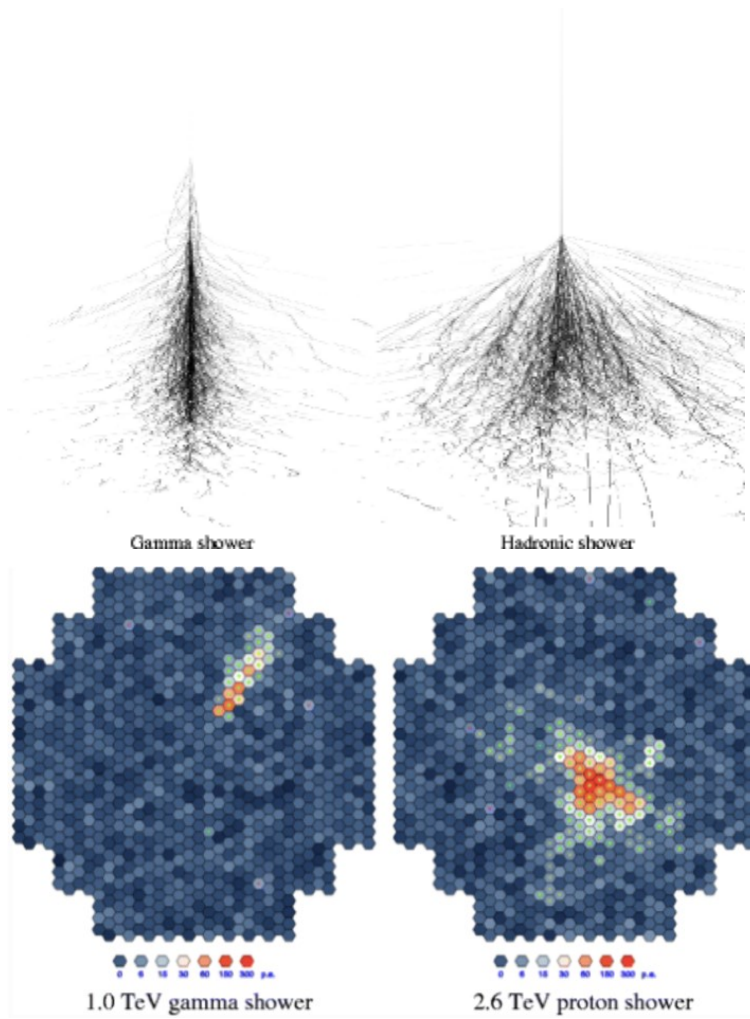
Figure 5.6: Comparison between a gamma shower (left) and a hadronic shower (right). The two signals on the camera are clearly different. Taken from (107).

This chapter is mainly based on Franceschini's High-Energy notes, (106) and CTA project (108).

6 Spectral analysis, EBL photon-photon corrections and ALP corrections

Not all high-energy spectral sources were used for this study, but only blazars BL Lac. Both HBL and IBL were analyzed in the same way, however a distinction between them will be highlighted in some figures below. For this analysis it was essential to know the redshift, the observed spectrum and the energy range in which every blazar is observed. The spectrum threshold energy was in VHE i.e. $E_0 > 100\ GeV$. These parameters were obtained by the TeVCat reference catalogue. From this, for each source, the redshift and the paper/papers presenting the observed spectra were taken (usually due to articles of large IACT collaborations). If a source in TeVCat did not present one of these two factors, a literature search was carried out. All BL Lacs presenting this information were used for this study. Furthermore, if a source had multiple observation spectra, the analysis was done for all spectra separately. In four cases the blazar did not present a precise redshift, as there is debate in literature on what is its exact value. For this reason, the same observed spectrum has been corrected considering different redshifts. However, the correction for only the most accredited redshift was included in the overall data analysis. The list of all the sources analyzed is shown in Table 1. A preliminary analysis of the observed energy range as function of z is shown in Fig. 6.1. This energy range is delimited by the maximum and minimum energy point of the observed spectrum; their average value for the single observation is indicated with a dot in the plot. The points with a white interior are associated, as will often happen in this thesis, with sources with uncertain redshift. In case of overlap the points in the plot are slightly shifted for clarity. The colored areas indicate the energy ranges that contain 80% of the sources. Given the great difference between sources with $z < 0.2$ and sources with higher redshift, we wanted to underline this discrepancy by using two independent colored areas. The average energy range for sources at $z < 0.2$ is obviously higher than that for sources at $z > 0.2$ due to the absorption of VHE photons for EBL. For the same reason the average energy range for $z < 0.2$ is very much larger.
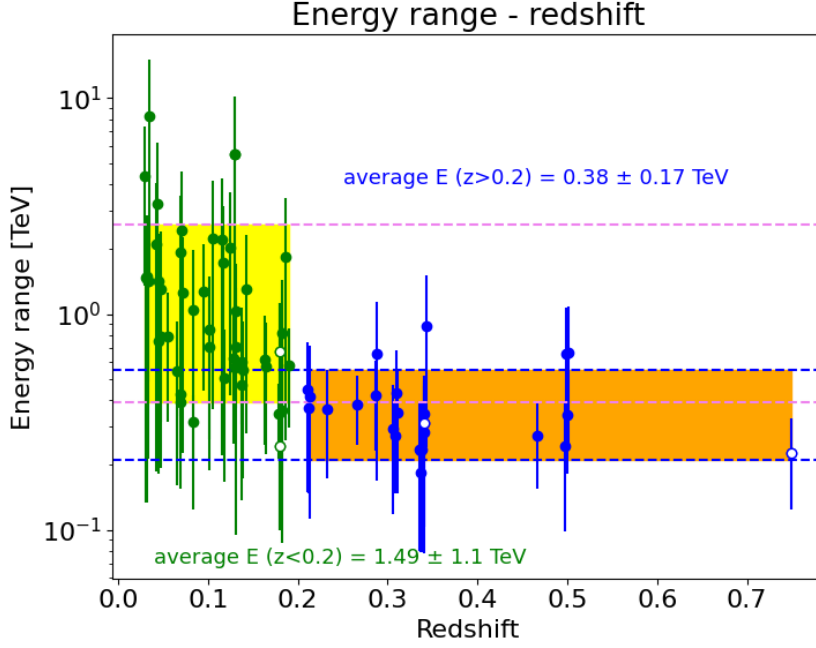
Figure 6.1: The two colored areas indicate the regions that contain 80% of the energies around the two average values, respectively within and beyond z=0.2. The average energy value of the yellow area is $\bar{E}_{z<0.2} = 1.49 \pm 1.1\,TeV$ and of the orange area is $\bar{E}_{z>0.2} = 0.38 \pm 0.17\,TeV$. The yellow area contains 38 data, the orange area 20. Without considering redshift limit, the total area containing 85% sources (62 objects) would be described by $\bar{E} = 1.11 \pm 0.9\,TeV$. The energy ranges are shown in Table 1.

All observed spectra are fitted by a single power law, neglecting a possible small curvature of some spectra in their lowest energy part, and so they have the form:

$$\Phi_{obs}(E_0, z) = \widehat{K}_{obs}(z) E_0^{-\Gamma_{obs,pp}(z)} \tag{6.1}$$

where E_0 is the observed energy, while $\widehat{K}_{obs}(z)$ and $\Gamma_{obs,pp}(z)$ denote the normalization constant and the observed slope, respectively, for a source at redshift z. As a reference energy $E_{0,*}$ is often used, the flux normalization constant $\widehat{K}_{obs,pp}(z)$ is generally defined at different energy for different sources. Since $E_{0,*}$ depending on the author's choice, the formula used in the papers is:

$$\Phi_{obs}(E_0, z) = K_{obs,pp}(z) \left(\frac{E_0}{E_{0,*,pp}}\right)^{-\Gamma_{obs,pp}(z)} \tag{6.2}$$

where $E_{0,*,pp}$ generally is 200, 250 or 300 GeV. Therefore, the normalization constant $K_{obs,pp}(z)$ changes depending on the value of the reference energy used. So, for the sake of comparison among

all observed flux normalization constants, we need to perform a rescaling $\hat{K}_{obs}(z) \rightarrow K_{obs}(z)$ in the observed flux of the considered blazars in such a way that $K_{obs}(z)$ coincides with $\Phi_{obs}(E_0, z)$ at the fiducial energy $E_{0,*} = 300 \; GeV$ for every source. Correspondingly, the observed flux takes the form:

$$\Phi_{obs}(E_0, z) = K_{obs}(z) \left(\frac{E_0}{300 \text{ GeV}} \right)^{-\Gamma_{obs}(z)} \tag{6.3}$$

$E_{0,*} = 300 \; GeV$ was used in all calculations of this thesis. The observed photon energies E_0 and the observed fluxes $\Phi_{obs}(E_0, z)$ were recovered from the tables within the papers. However, in the absence of these, the "Digitizelt" program was used to derive them directly from plots in papers. The energy ranges are shown in Table 1.

The observed spectrum is $\Phi_{obs}(E_0, z) \equiv dN_{obs}/(dA \; dt \; dE_0)$, where N_{obs} is the photon number count and A is the detector area, and likewise the emitted flux is $\Phi_{em}(E) \equiv dN_{em}/(dA \; dt \; dE)$, where N_{em} is the number of emitted photons and A is the area of the emitting region, while $E \equiv (1 + z)E_0$. Emitted spectra of both leptonic and hadronic photon emission models have, to a good approximation, a single power-law behavior: $\Phi_{em}(E) = K_{em}E^{-\Gamma_{em}}$. As for the observed spectrum, K_{em} indicates the normalization constant and Γ_{em} the spectrum slope. The relationship between $\Phi_{obs}(E_0, z)$ and $\Phi_{em}(E)$ can be generally expressed as:

$$\Phi_{obs}(E_0, z) = P_{\gamma \rightarrow \gamma}(E_0, z) \cdot \Phi_{em}(E_0(1 + z)) \tag{6.4}$$

where $P_{\gamma \rightarrow \gamma}(E_0, z)$ is the photon survival probability from the source to us, which is usually written in terms of optical depth $\tau_\gamma(E_0, z)$ as:

$$P_{\gamma \rightarrow \gamma}(E_0, z) = e^{-\tau_\gamma(E_0, z)} \tag{6.5}$$

The aim of this thesis is to verify if there is a correlation between the emitted spectrum slope (Γ_{em}) and redshift. In general, the spectral slope varies from spectrum to spectrum (even for the same source in different period) due, as seen in chapter 4, to the strong variability over time of the spectrum of these sources. However, rather similar values are expected as the redshift increases.

Instead, according to several observational works (1), sources at high redshift have a low emission index (Γ_{em}): that is, sources with high z would have a harder spectrum.

Excluding the hypothesis that this is an intrinsic effect, there are three other possibilities to explain the phenomenon: the EBL high-redshift correction is not very reliable, there is a selection effect or

the presence of ALPs. As explained in chapter 3, despite the various observational difficulties, the correction for EBL is rather well constrained. There are in fact several models (with different hypotheses and procedures) that attempt to estimate this contribution and provide rather similar values. Although there are differences among the various models, these are not sufficient to explain the difference in slope of high redshift sources.

About cosmological evolutionary effects in the sources, a lot of papers (1) suppose that they are certainly harmless up to redshift $z = 0.6$. A second selection effect is the dimming bias. It means that as we look at larger distances only the brighter sources are observed while the fainter ones progressively disappear. This arises from two distinct effects: Malmquist bias and EBL absorption. The latter is clearly very important because it significantly modifies the spectrum shape. Otherwise Malmquist bias is associated to the fact that the really emitted luminosity goes like the inverse of the square distances. This effect does not affect the shape of blazar spectra and so it cannot be responsible for the high redshift BL Lac spectral anomaly. Furthermore, as seen in chapter 4, increasing the blazar luminosity, γ–ray spectrum softens are expected at VHE. Although the dimming bias can never be avoided, several papers agree to exclude the dimming bias from the root of the problem (1). The last one selection effect is the volume dimming. Looking at greater distances entails that larger regions of space are probed, and so, under the assumption of a uniform source distribution, a larger number of brighter blazars should be detected. This purely geometric argument was treated with accuracy in Galanti et al. (1): they strongly argued that it is not responsible for this correlation. The third hypothesis consists in hypothesizing the presence of the ALPs described in chapter 2. These particles would in fact result in a lower absorption of high-energy photons: in this way the spectrum would be softer.

In practice, I proceeded step by step: first I made an analysis of the observational data to have reference spectra to compare with the correct ones. Then I applied the correction for EBL in conventional physics (CP) to all spectra using the Franceschini model (54). Having obtained all the spectral indices with their respective normalizations, I observed if indeed the evolution with the redshift of Γ_{em} is decreasing. Since this has been confirmed, I decided to apply a second type of correction based on ALPs, using the Galanti's theoretical model (21). To show the results, the chapter was divided into three subsections: observational analysis, EBL correction with conventional physic and EBL correction with ALPs.

6.1 Observational analysis

Starting from the observed energies and fluxes, we wanted to calculate, first of all, the corresponding observed spectral indices with the relative normalization constants. For this I created a program on Python that calculates the numerical best-fit associated with the function in eq. (6.3). This program was used to determine the spectral parameters of each spectrum shown in this thesis. The result for the PG 1553 + 113 source, observed with the HESS telescope in 2005, is shown in Fig. 6.2.
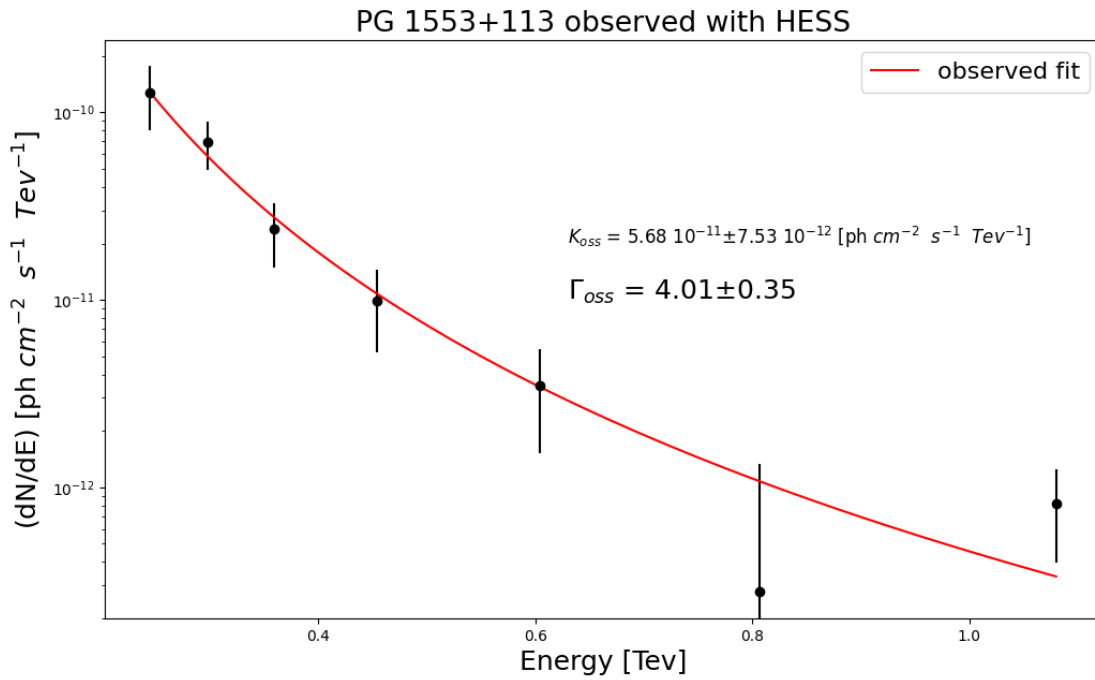
Figure 6.2: PG 1553+113 observed spectrum obtained from HESS data. The normalization constant and the spectrum index, generated by the Python program, are illustrated in the plot.

The algorithm used is the Levenberg-Marquardt Algorithm (LMA), a generally efficient and reliable numerical procedure for finding local minima, which is applied to the chi-square minimization (χ^2). For this method it is necessary to provide initial values to the routine, from which it can start looking for the minimum. In the case of "complicated" functions, or when it is a priori possible that there is more than one local minimum in χ^2, the initial conditions should be such as to provide a "reasonable" (initial) match with the data to be rented. If this does not occur, it is possible that the minimization algorithm does not converge, or that it converges to values that, based on physical considerations, are clearly wrong. Fortunately, this is not the case, since the function considered is a simple single power law for which it is possible to determine reasonable values of the parameters simply by inspecting the data. In addition to normalization, spectral index and related errors, the program returns

two factors: the normalized covariance c [4] (or correlation coefficient) and the ratio between the chi-square (χ^2) and the number of degrees of freedom of the system ($ndof$). The first element indicates how much the two parameters (K_{obs} e Γ_{obs}) are related to each other: that is, how much the variation of one parameter can be "compensated" by the variation of the other. Conventionally, the parameters are called strongly correlated (or anticorrelated, in case of negative sign) if $|c| \gtrsim 0.8$ and totally correlated (or anticorrelated) if $|c| \approx 1$. Instead, a null covariance, a practically impossible case in the best-fit of physical interest, indicates that the parameters are completely independent from each other, that is, the variation of one is not at all correlated with that of the other. For PG 1553 + 113 the correlation coefficient was found to be $c = 0.48$, so we can consider K_{obs} e Γ_{obs} on average correlated. The second factor that produces the program is the reduced chi-square ($\tilde{\chi}^2$). This is used to check if the experimental data are well expressed by a theoretical model described by a power law function. When $\tilde{\chi}^2 \sim 1$, it means that the single power law does not accurately describe the data. Over 75% of the spectra seems to provide comforting values with respect to the power law. For example, for the spectrum of PG 1553 + 113 the $\tilde{\chi}^2 = 0.475$ with $ndof = 5$. Being more precise, you could compare the values resulting from the program with the tabulated chi-square values: in particular, for this source the probability of finding a chi-square smaller (better) than the obtained value is less than 25 %. However, sometimes the number of bins (and therefore the degrees of freedom) of the single spectrum is rather low, so the test is not fully reliable in the single spectrum. On the other hand, if we consider all the data, we can confirm that single power law describes the shape of the spectrum of blazars very well. Furthermore, according to several studies, spectral shapes more complex than a simple power law do not result in a significant improvement in the fit. The results of the spectral indices and relative normalization coefficients for all the analyzed spectra are reported in columns 5 and 6 of Table 1.

Plotting the value of the observed spectral indices as a function of redshift, we realize the influence of EBL on the observations (Figure 6.3). In fact, at high redshift the spectra turn out to be much softer since the photons of higher energy (about 1 TeV) are more likely to be absorbed during the long journey to us. For example, let's consider two photons: one of 100 GeV energy and one of 1 TeV. As

---

[4] Let us imagine having a function $f(\alpha, \beta)$ that depends on two variables α, β and suppose that these variables correspond to two measurable quantities. Their measurement gives the values α_i, β_i, with i running from 1 to N, the total number of measurements. Using the average values $\bar{\alpha}$ e $\bar{\beta}$ we obtain the covariance: $\sigma_{\alpha\beta} \equiv \frac{1}{N-1}\Sigma_i(\alpha_i - \bar{\alpha})(\beta_i - \bar{\beta})$.

clearly visible in Fig. 3.4 of chapter 3, the curves of different redshift seem to have the same slope and therefore you could think that the difference in absorption between the two photons is the same regardless of the redshift. However, this is not the case, because the ordinate is a logarithmic function, so the difference in optical depth is much greater at high redshift. From eq. (3.10) and eq. (6.5), it results that the survival probability decreases a lot: that is, the ratio between the number of photons at 1 TeV and those at 100 GeV that reach us will be much lower for a high z source than for a blazar near us. The Fig. 6.3 exploits data from only sources whose redshift is considered known in TeVCat (from this point: z TeVCat sources). Instead Fig. 6.4 also takes into account sources whose redshift is quite well constrained but not completely. For these sources, in fact, recent research suggests redshift values that are not entirely consistent. These four sources are illustrated with an empty dot. In both plots, three spectral fits with functions of increasing degree were made to describe the data. These fits were obtained with the same program explained above. Clearly the constant function (pink dashed curve) does not describe the data well but has been included to highlight the evolution of the spectral index with redshift. The best fit straight lines representing the data are shown in red, while the best fit parabolas are shown in blue. Among the curves in Fig. 6.3, the one with the best $\tilde{\chi}^2 = 7.35$ ($ndof = 66$) is the parabola, even if the straight line has a rather similar value. Considering all data, it results $\tilde{\chi}^2 = 6.99$ with $ndof = 70$. The coefficients of the curve with the best $\tilde{\chi}^2$ are always written in plots. To better compare the two cases, in Fig. 6.4 has been inserted the green line indicating the best fit parabola of z TeVCat sources. The two best-fit parabolas are practically coincident.

Figure 6.3: Scatter plot between observed VHE spectral index of the z TeVCat BL Lacs with redshift. The red and blue solid lines are the best-fit straight line and parabola respectively. The dashed line is the best-fit of degree zero. It is also illustrated the equation of the curve with the best reduced chi-square. The spectral indices of this plot are summarized in Table 1.
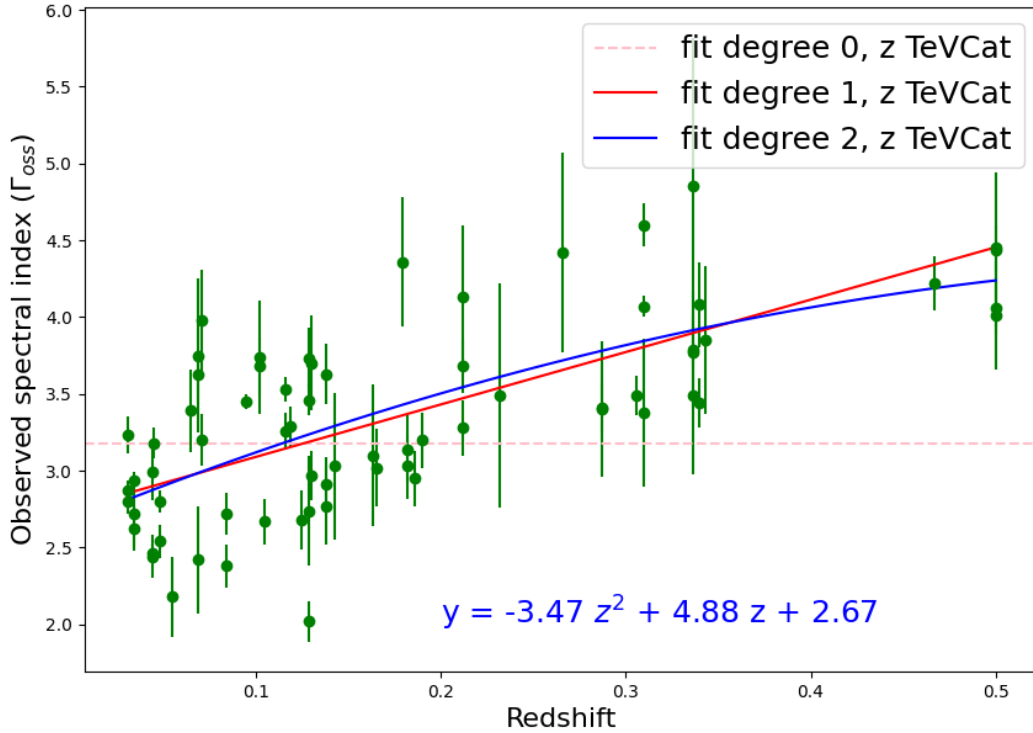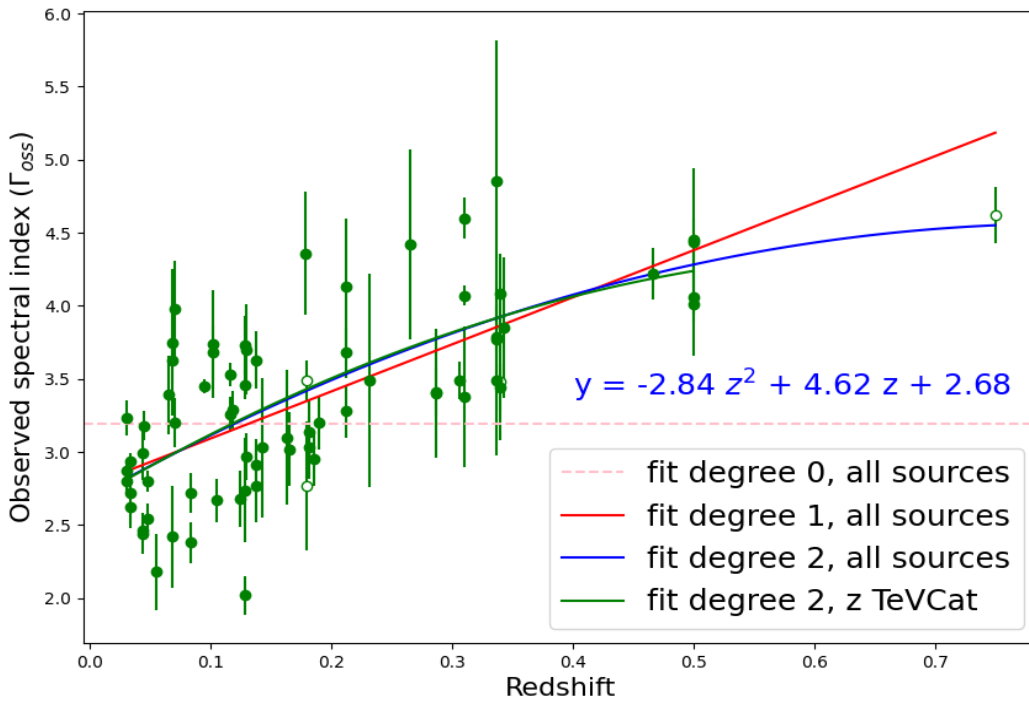

Figure 6.4: Scatter plot between observed VHE spectral index of all BL Lacs with redshift. The red and blue solid lines are the best-fit straight line and parabola respectively. The dashed line is the best-fit of degree zero. It is also illustrated the equation of the curve with the best reduced chi-square. The spectral indices of this plot are summarized in Table 1.

6.2 EBL correction through conventional physics

The second step was to carry out the correction for EBL to estimate the fluxes emitted by the sources, according to standard physics. To do this we used the model of Professor Franceschini described in chapter 3. In this model it is necessary to insert the redshift of the source and some information about the normalization factor to be used. Once these standard data are supplied, the program generates an output file in which it lists the corrections to be made for each observed energy (E_0). For each source the file produces a table, which in the first column presents 500 observed energy values starting from $E_0 = 0.9 \cdot 10^{-4}\ TeV$ up to $E_0 = 0.96807 \cdot 10^3\ TeV$. In the second column there are the same E_0, but expressed in GeV, while in the third column the program calculates the optical depths (τ_γ^{FR}) associated with each observed energy. The last column calculates $e^{\tau_\gamma^{FR}}$, i.e. the probabilities of each gamma photon to generate electron-positron pair-production before being detected. The trend of $e^{\tau_\gamma^{FR}}$ as a function of the observed photon energy for a source at redshift 0.5 is on the left in Fig. 6.5. This graph was obtained by means of a spline, that is a function, consisting of a set of connected polynomials, the whose purpose is to interpolate a set of points, called nodes, in a certain interval. Furthermore, this function is continuous in all nodes. Clearly the nodes are none other than the points $(E_0, e^{\tau_\gamma^{FR}})$ obtained as output from the correction program for EBL. The spline used here is of third degree, that is, it generates a set of continuous cubics that can be differentiated twice within the interpolation interval. As seen above, the difference in photon absorption probabilities of $E_0 > 200\ GeV$ at different redshifts is enormous. This is evident by comparing the two images in Fig. 6.5 indicating the absorption for a source at $z = 0.5$ and one at $z = 0.034$.
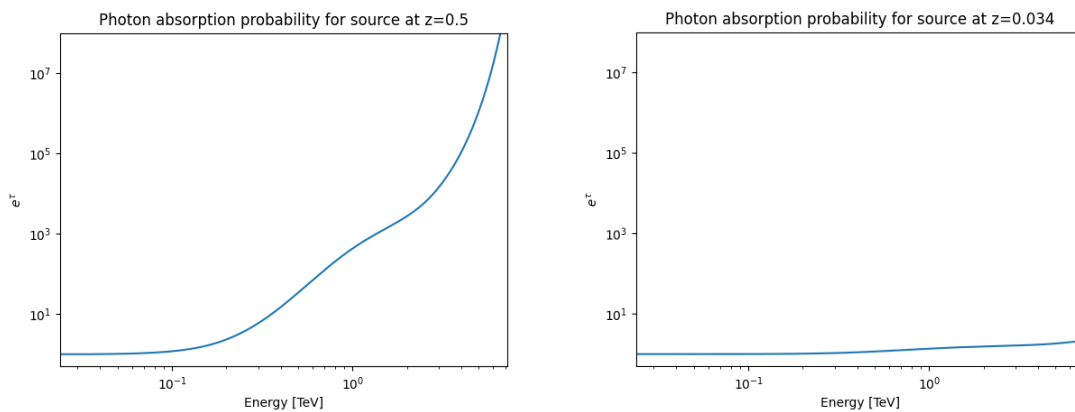
Figure 6.5: Photon absorption probability for sources at $z = 0.5$ (left) and $z = 0.034$ (right).

To determine the flow of energy E_0 emitted by the source, we simply multiplied the observed flow by the probability that that photon has of being absorbed:

$$\Phi_{em}^{CP}(E_0(1+z)) = e^{\tau_\gamma^{FR}(E_0,z)}\Phi_{obs}(E_0,z) = e^{\tau_\gamma^{FR}(E_0,z)}K_{obs}(z)\left(\frac{E_0}{E_{0,*}}\right)^{-\Gamma_{obs}(z)} \quad (6.6)$$

Because of the presence of the exponential in the r.h.s. of the previous equation, $\Phi_{em}^{CP}(E_0(1+z))$ cannot behave as an exact power law. However, it is expected to be closed to it. Therefore, I best fit (BF) $\Phi_{em}^{CP}(E_0(1+z))$ to a single power-law expression in the same way as the observed flow:

$$\Phi_{em}^{CP,BF}(E_0(1+z)) = K_{em}^{CP}(z)\left(\frac{E_0(1+z)}{300\ GeV}\right)^{-\Gamma_{em}^{CP}(z)} \quad (6.7)$$

over the energy range $\Delta E_0(z)$ where a source is observed, and so E_0 varies inside $\Delta E_0(z)$ (which changes from source to source). Correspondingly, the resulting values of $\Gamma_{em}^{CP}(z)$ and $K_{em}^{CP}(z)$ for all the sources are indicated in Table 2.
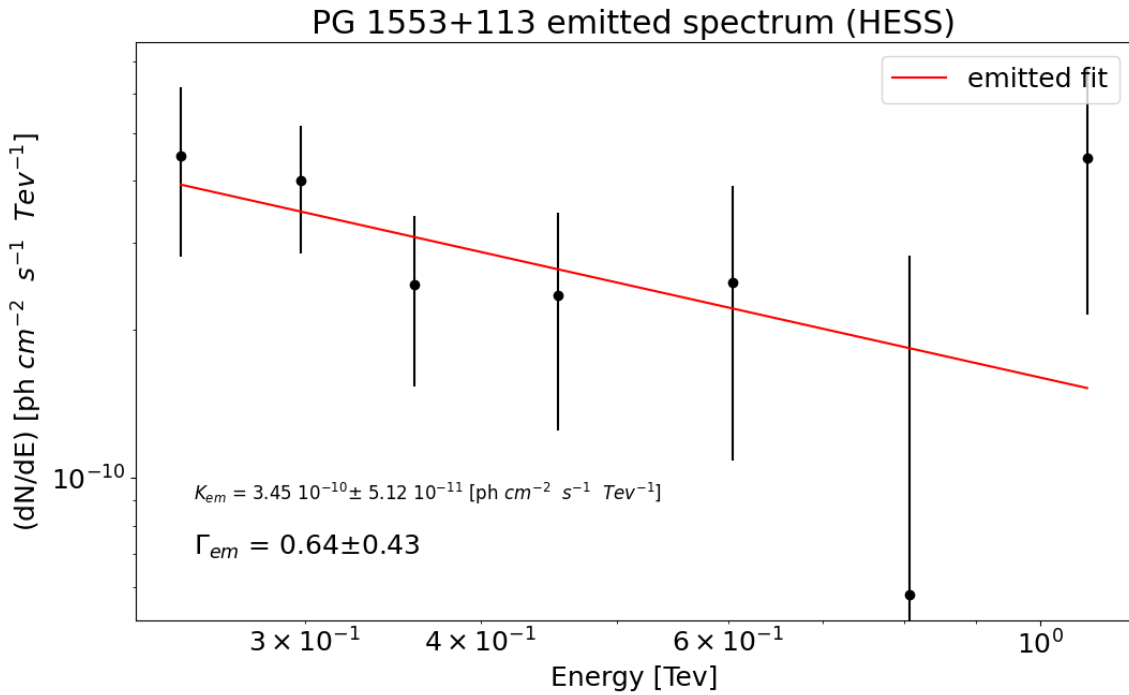
Figure 6.6: PG 1553+113 emitted spectrum obtained from HESS data. The normalization constant and the spectrum index, generated by the Python program, are illustrated in the plot.

The correct graph for EBL always for the source PG 1553 + 113, observed with HESS, is shown in Fig. 6.6. Also in this case the spectral index and the normalization constant are not correlated since $c = 0.51$. The $\chi^2 = 2.81$ ($ndof = 5$) gave slightly greater results than the observed fit but still well below the limiting case: $\tilde{\chi}^2 \sim 1$. The numerical best-fit program that was used is the same as that applied for the observed flow. And it is the same that was used to derive the normalization constant and the slope of all the spectra analyzed in this thesis work.

More significant is the plot that includes both spectral fits: the one associated with the observed spectrum and the corrected one (Fig. 6.7). In this way it is easy to understand how the correction for EBL involves a strong hardening of the spectrum due to a greater absorption of photons at $E_0 \sim 1\ TeV$ compared to less energetic photons.
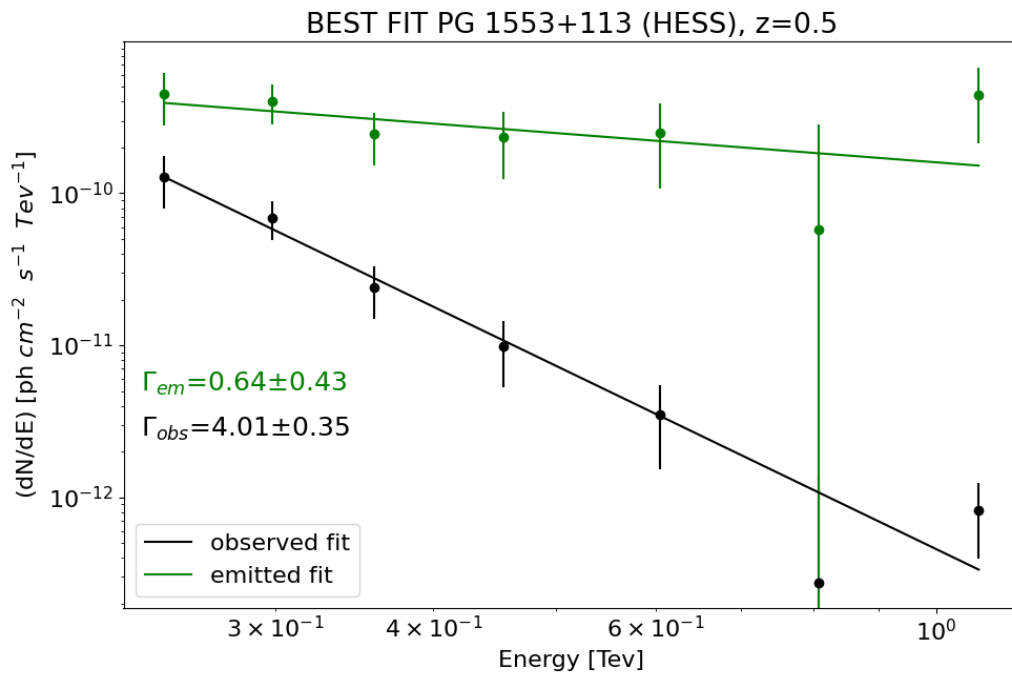
Figure 6.7: emitted and observed spectra obtained from HESS data for the source PG 1553+113. The green line is the emitted best fit, the black line the observed. The two spectral indices are illustrated in the plot.

These correction steps have been carried out for all the sources considered. Among the sources of uncertain redshift, a very interesting example is RGB J2243, one of the most distant blazars ever observed at VHE. The first time an attempt was made to place a first constrain on its distance dates back to 2010 when Meisner & Romani (109) set a lower limit on the redshift from studies on its host galaxy. In fact it has been claimed (110) that BL Lac host galaxies detected with HST imaging are remarkably uniform giant ellipticals with absolute magnitude in R band: $M_R = -22.9$; accordingly

host detections can give redshift estimates and upper limits on the host flux can give lower limits on the distance. They were unable to resolve the host, therefore, a lower limit on the redshift, $z > 0.39$, was calculated using the upper limit of the host galaxy flux. A second attempt to constrain the redshift of RGB J2243 was made in 2017 by Abeysekara et al. (111), who applied a model proposed by Georganopoulos et al. of 2010 (112) to put an upper limit on the redshift. This method does not assume any source emission models but requires almost simultaneous observations at VHE and HE (Fermi-LAT telescope). The only assumption is the observed VHE component of the energy spectrum is softer than the extrapolation of the Fermi-LAT GeV energy spectrum. The Georganopoulos model allows to obtain the maximum possible optical depth due to the discrepancy between the observed VHE flux $F(E)_{obs}$ and the flux derived at energy E from the extrapolation of the GeV energy spectrum $F(E)_{ext}$:

$$\tau_{max}(E) = \ln\left(\frac{F(E)_{ext}}{F(E)_{obs} - 1.64 \times \Delta F(E)_{obs}}\right) \qquad (6.8)$$

where $\Delta F(E)_{obs}$ accounts for the error in the VHE flux measurements. The upper limit of $\tau(E)$ can be translated into an upper limit on the redshift by comparing with EBL models. This redshift limit is obtained by finding the value of z which minimizes the difference between the optical depth of the model $\tau(E, z)$ and $\tau_{max}(E)$. This work was applied to different EBL correction models obtaining three upper limits: $z < 0.9$, $z < 1.0$ and $z < 1.1$. In the case of softening of the intrinsic energy spectrum at VHE the redshift upper limit would be lower. On the contrary, an intrinsic hardening of the VHE spectrum would increase the derived upper limit. In general, spectral hardening at TeV energies is not expected, however some hadronic models predict a spectral hardening at high energies (e.g. (113)). In fact in 2019, Sahu et al. (114) using a photohadronic model and performing a statistical analysis, bound the redshift in the range $0.75 < z < 1.1$. All these models were found to be quite consistent with each other; in contrast to the 2018 observations of Gonzalez et al. (115) obtained with the OSIRIS Multi Object Spectrograph (MOS) on the RGB J2243 environment provided completely different values. Since the spectra of neither the BL Lac nor its host galaxy show any spectral feature, they observed 4 galaxies in the MOS field of view with redshift between 0.5258 and 0.5288. Making use of a statistical analysis to test the possibility that RGB J2243 may be a member of that group, they found a probability between 86% and 93%. For these reasons, in this thesis it was decided to carry out the analysis for three different cases: $z = 0.5$, $z = 0.75$ and $z = 1.1$. The emitted spectra are illustrated, together with the observed spectrum, in Fig. 6.8. As previously imaginable, the greater the distance from the source, the harder the emitted spectrum is. This is simply due to the greater photons probability to interact with EBL.

In all subsequent analyzes, only the case $z = 0.75$ was used as it is considered more accredited.
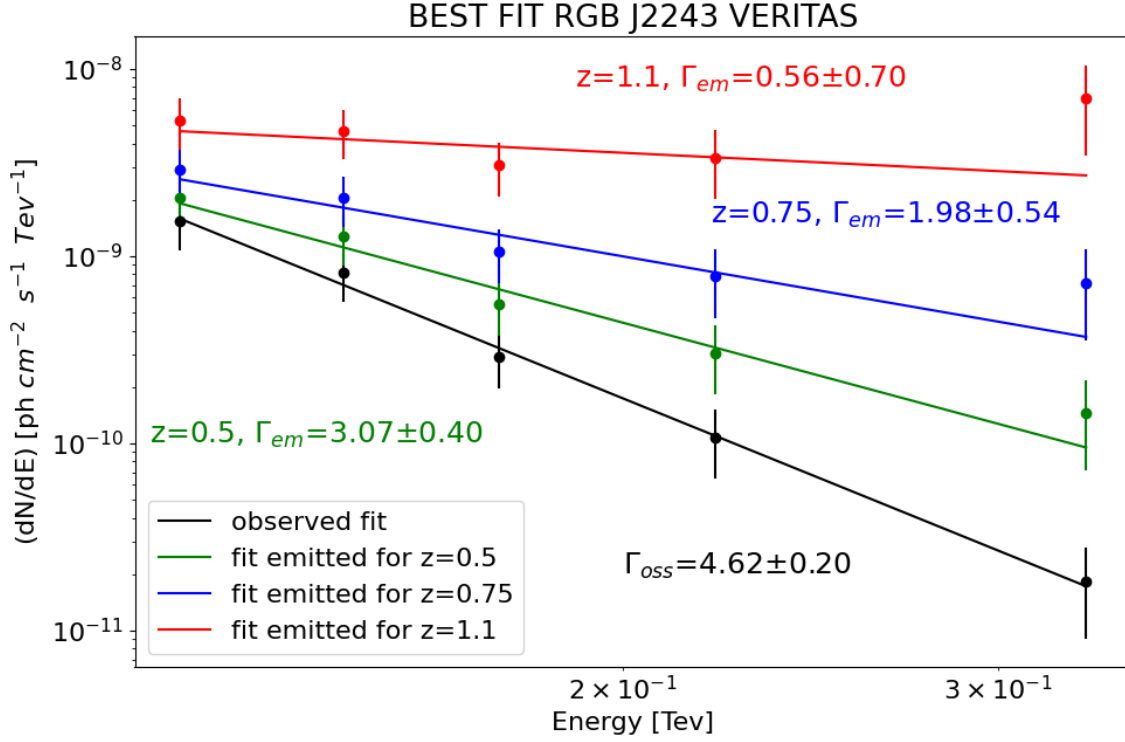
Figure 6.8: The emitted and observed spectra obtained from VERITAS data for the source RGB J2243. The emitted best fit considering $z = 0.5$, $z = 0.75$ and $z = 1.1$ are illustrated in green, blue and red, respectively. The black line is the observed best fit. The spectral indices are illustrated in the plot.

As previously mentioned, the main purpose of this thesis is to verify the trend of the spectral indices emitted as a function of the redshift. Fig. 6.9 collects the emitted spectral indices obtained from all analyzed spectra as a function of redshift. If, as with RGB J2243, a source has more than one redshift, only the most reliable z will be taken, according to the studies in letterature. Instead, if a source has more than one spectrum, it will have more than one point in the plot. All data are indicated with green point but, those associated to an uncertain redshift, have a white interior. As in Fig. 6.3 and 6.4, also in this case it was decided to find the best-fit curves. Three spectral fits with increasing degree functions were made to describe the data. The dashed pink horizontal line indicates the fit of degree 0, the red one of degree 1 and the parabola in blue is the spectral best-fit of degree 2. The trend predicted by the theory is the pink one, that is, regardless of the distance from us, the intrinsic spectra should have the same slope. However, the chi-square suggests that the blue parabola is the function that best describes the data. The reduced chi-square values result in increasing order of degree of the

function: $\tilde{\chi}_0^2 = 8.98\ (ndof = 72)$, $\tilde{\chi}_1^2 = 8.53\ (ndof = 71)$, $\tilde{\chi}_2^2 = 8.42\ (ndof = 70)$. These values are rather large since in general the data are not very consistent with each other.
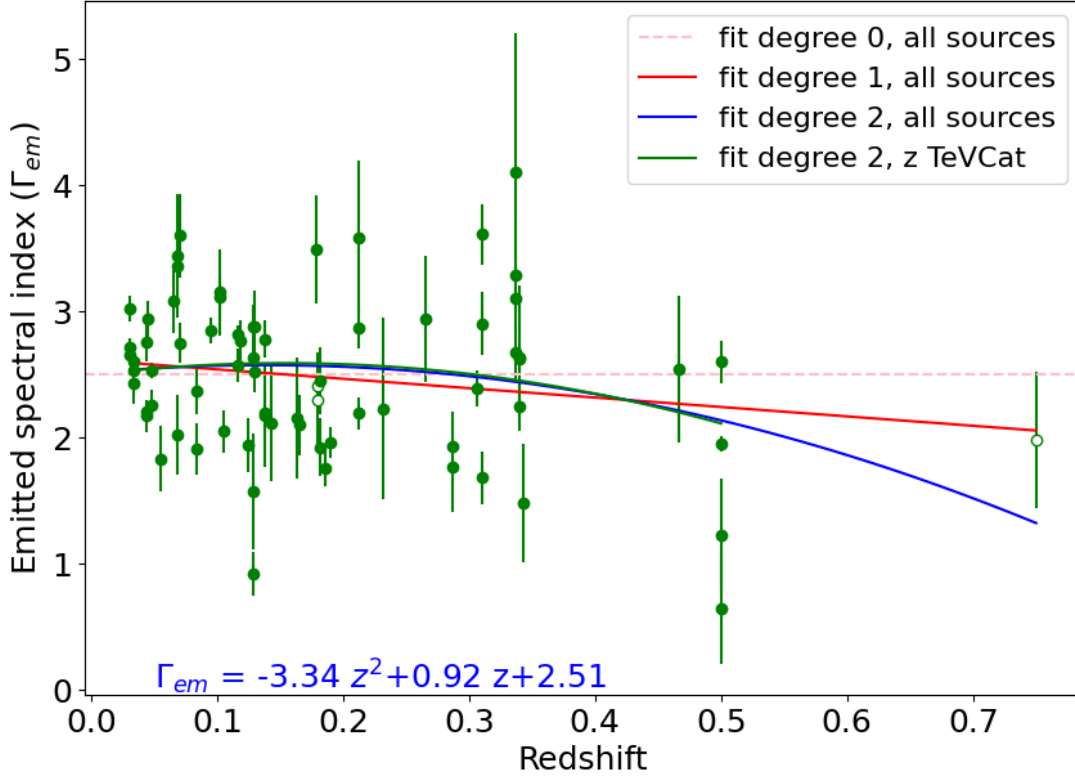
Figure 6.9: Scatter plot between emitted VHE spectral index of all BL Lacs with redshift. The red and blue solid lines are the best-fit straight line and parabola respectively. The dashed line is the best-fit of degree zero. It is also illustrated the equation of the curve with the best reduced chi-square. In green the curve with the best reduced chi-square for z TeVCat BL Lacs. The spectral indices of this plot are summarized in Table 2.

Clearly the points obtained for the high-redshift RGB J2243 source greatly influence the trend of the spectral index. However, even without considering this source, and in general the sources with uncertain z, there is still a decrease in the emitted spectral index as the redshift increases. The best fit function that presents the lower chi-square reduced is the green parabola in Fig. 6.9: $\Gamma_{em}^{CP}(z) = -3.99z^2 + 1.22z + 2.49$ with $\tilde{\chi}_2^2 = 8.87\ (ndof = 66)$. This curve will be often use in the next plot to provide a comparison. For this reason, this curve will be indicated as reference curve. Compared to similar works found in the literature, the evolution of the spectral index with redshift is rather flat but still suggests a hardening of the intrinsic spectrum of high redshift sources. Indeed, keep in mind that $\Gamma_{em}^{CP}(z)$ is the exponent of the emitted energy entering $\Phi_{em}^{CP}(E, z)$, in the two extreme cases $z = 0$ and $z = 0.75$ we have:

70

$$\Phi^{CP}_{em}(E, 0) \propto E^{-2.49}, \qquad\qquad \Phi^{CP}_{em}(E, 0.75) \propto E^{-1.16} \qquad\qquad (6.9)$$

In Fig. 6.10 the results obtained here (green line) are compared with the work of Galanti et al. (1) (black line). The difference at high redshift is notable since in this work other spectra of PG 1553+113 were used which present $\Gamma^{CP}_{em}(z)$ higher. In any case, what they both agree on is a hardening of the spectra emitted at high redshift.
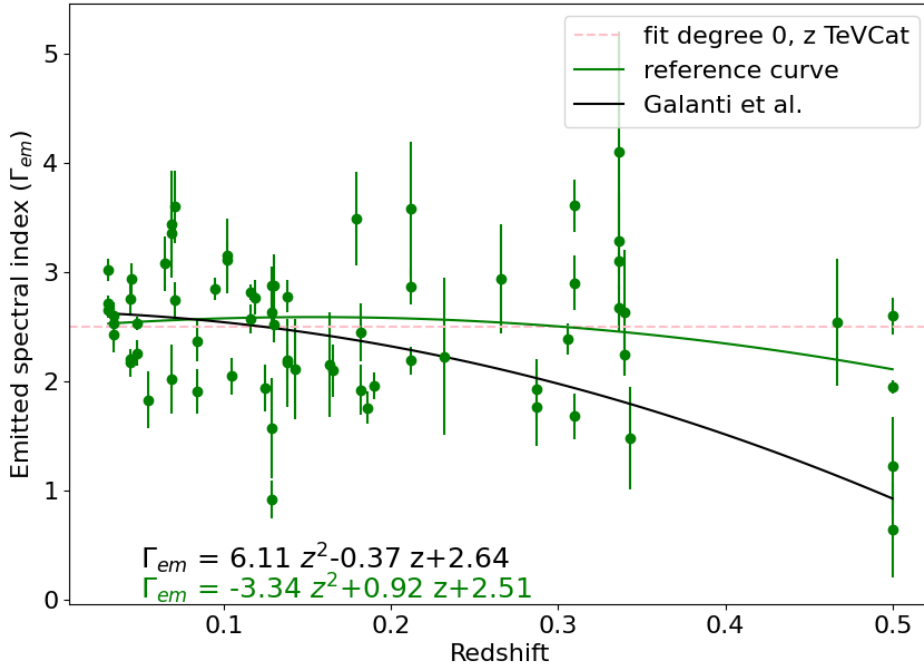
Figure 6.80: Scatter plot between emitted VHE spectral index of z TeVCat BL Lacs with redshift. The green parabola is the reference curve (more details in text) and the black parabola is the curve with the best reduced chi-square found by Galanti et al. *(1)*. The spectral indices of this plot are summarized in Table 2.

The data used so far considers all the blazars studied in this thesis, regardless of their spectral type, since the vast majority are HBL. Figure 6.11 shows the blazars observed, highlighted in different colors according to their classification: in red are indicated the IBL, in green the HBL and in blue the uncertain sources. However, it was decided to create the same previous plot but considering only the sources cataloged as HBL in TeVCat (Fig. 6.12). Hence, the dashed pink, the red and blue curves are always the best-fits of different degree but obtained using only HBL blazars. While the continuous purple curve is the reference curve, inserted here for comparison. This time the curve with the best reduced chi-square is the straight line: $\tilde{\chi}^2_1 = 6.94 \, (ndof = 54)$. Furthermore, the yellow area

indicates the region between the straight lines with different errors associated with the coefficients: $\Gamma_{em}^{CP} = (a + da)z + (b - db)$ and $\Gamma_{em}^{CP} = (a - da)z + (b + db)$.

Comparing the purple and red curves, it is even more evident how for only HBL sources the emitted spectral index decreases as the redshift increases.

For completeness in Fig. 6.13, the two best-fit straight lines are compared: one considering only the HBL with z TeVCat (green line) and one considering also the two HBL sources whose z is uncertain (yellow line).
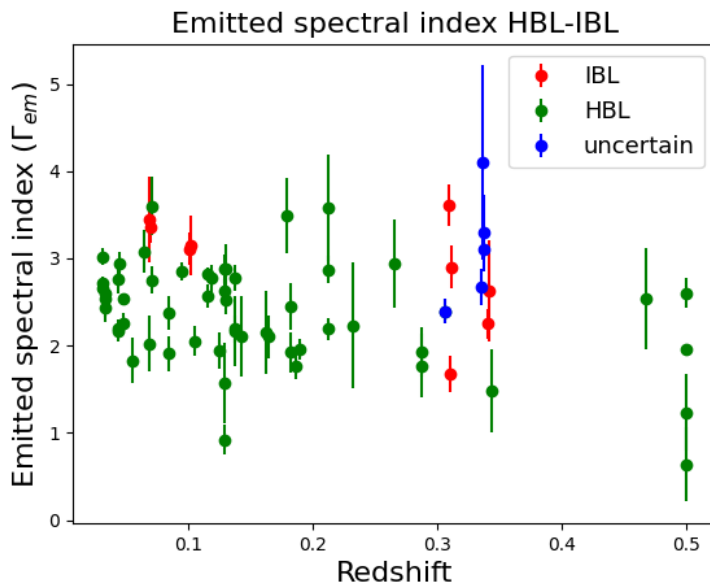
Figure 6.11: Scatter plot of z TeVCat sources showing their spectral classification.

Figure 6.12: Scatter plot between emitted VHE spectral index of z TeVCat HBLs with redshift. The red and blue solid lines are the best-fit straight line and parabola respectively. The yellow area indicates the region between the straight lines

72

with different errors associated with the coefficients: $\Gamma_{em}^{CP} = (a + da)z + (b - db)$ and $\Gamma_{em}^{CP} = (a - da)z + (b + db)$. The dashed line is the best-fit of degree zero. In pink the reference curve. It is also illustrated the equation of the curve with the best reduced chi-square. The spectral indices of this plot are summarized in Table 2.
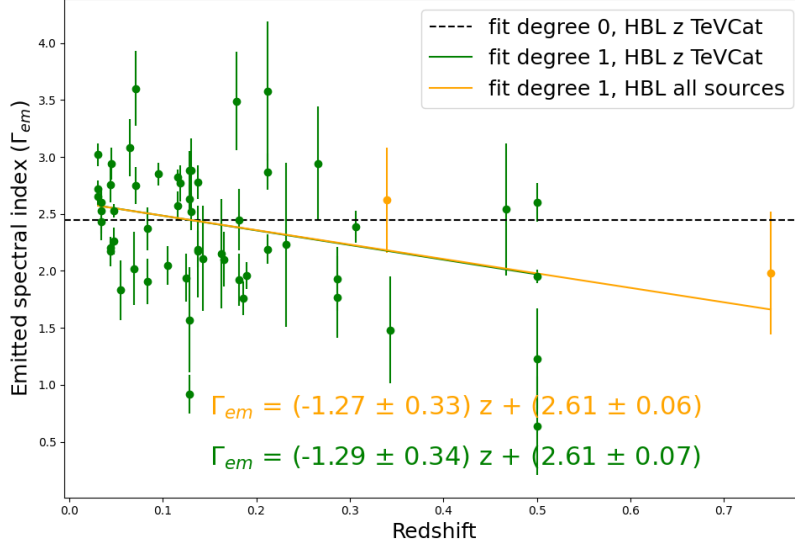
Figure 6.13: Scatter plot between emitted VHE spectral index of HBLs with redshift. Green points are z TeVCat HBLs, yellow points the HBLs with uncertain redshift. The green and yellow lines are the best-fits of degree 1. The spectral indices of this plot are summarized in Table 2.

The last one possibility of analysis of the emitted flow was made by analyzing only one data per source. Given that different sources have more than one spectrum, it was decided to calculate the average spectral index in these cases ($\bar{\Gamma}_{em}^{CP}$). For each source this value was obtained through a simple average of the different spectral indices emitted, weighted by the relative errors. In formula:

$$\bar{\Gamma}_{em}^{CP} = \frac{\sum_{i=1}^{N} \Gamma_{em,i}^{CP}/\sigma_{em,i}^2}{\sum_{i=1}^{N} 1/\sigma_{em,i}^2} \qquad (6.10)$$

with $\sigma_{em,i}$ indicating the error associated with the i-th emitted spectral index and N the total number of spectra observed for a certain source. The overall error ($\bar{\sigma}_{em}$) on this weighted average was calculated as follows:

$$\bar{\sigma}_{em} = \sqrt{\frac{1}{\sum_{i=1}^{N} 1/\sigma_{em,i}^2}} \qquad (6.11)$$

As in the Fig. 6.12, in Fig. 6.14 the best-fits of different degree are indicated to describe the data but this time are used the average emitted spectral indices calculated with the eq. 6.10 and eq. 6.11. In this plot is also include the reference curve in purple. The curve with the best $\tilde{\chi}_2^2 = 11.18$ ($ndof = 35$) is the blue parabola, whose coefficients are indicated in the plot.
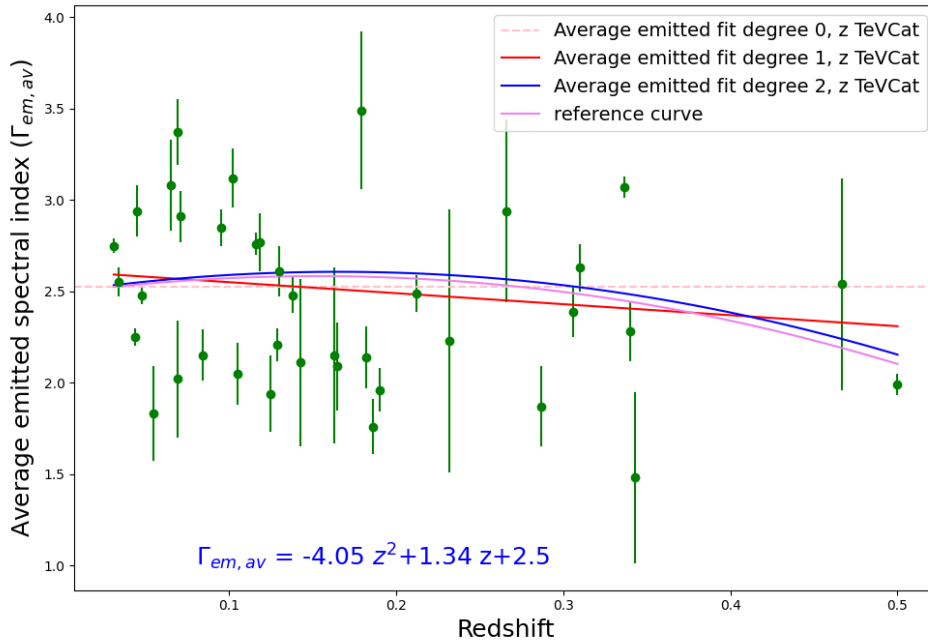
Figure 6.14: Scatter plot between average emitted VHE spectral index of TeVCat BL Lacs with redshift. The red and blue solid lines are the best-fit straight line and parabola respectively. The dashed line is the best-fit of degree zero. It is also illustrated the equation of the curve with the best reduced chi-square. In pink the reference curve. The spectral indices of this plot are summarized in Table 8 as Method I.

There is also another way to describe $\overline{\Gamma}_{em}$ of a source. Instead of calculating them from the weighted average of all the spectral indices describing that source, you can determine the best-fit obtained from all the points of all the spectra describing that source. In this way, the average emitted spectral index is calculated giving more prominence to all the spectral data. For this reason, it is indicated as $\overline{\Gamma}_{em,all}$. The results suggest even harder spectra at high z and a lower reduced chi-square: $\tilde{\chi}_1^2 = 4.89$ ($ndof = 36$) due to the red line in Fig. 6.15.

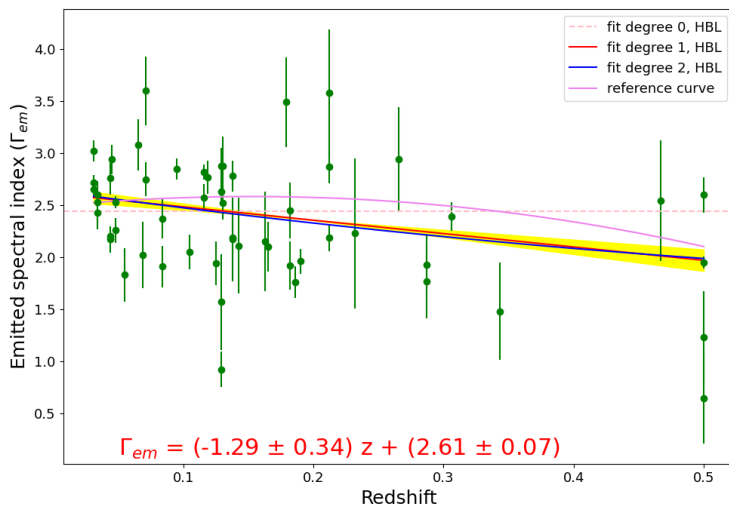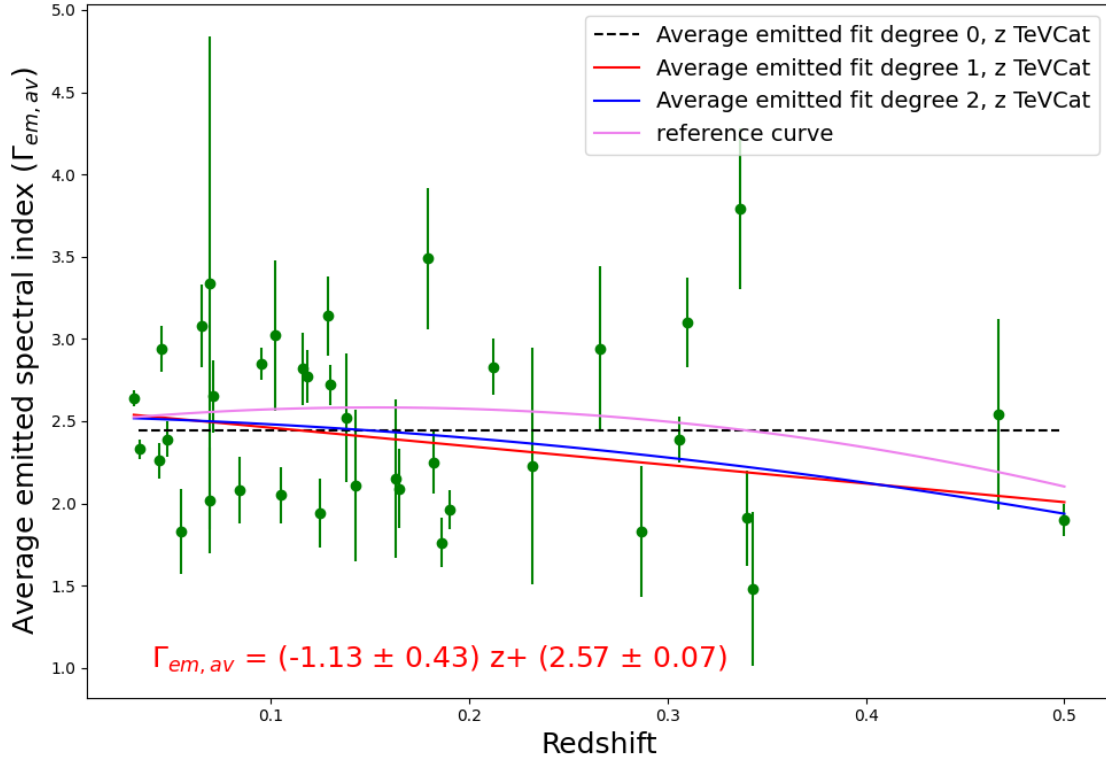Figure 6.15: Scatter plot between average (II method) emitted VHE spectral index of TeVCat BL Lacs with redshift. The red and blue solid lines are the best-fit straight line and parabola respectively. The dashed line is the best-fit of degree zero. It is also illustrated the equation of the curve with the best reduced chi-square. In pink the reference curve. The spectral indices of this plot are summarized in Table 8 as Method II.

Considering the data taken into consideration, it apparent that the emitted spectral index becomes harder as the redshift increases. As previously stated, this eventuality does not seem to have a valid physical explanation but could be the result of an interaction between photons and ALPs. Certainly, however, the high redshift statistic is still affected by uncertainties. In fact, few sources have been observed up to now at $z > 0.3$. The hope is that the new set of IACT telescopes by exploiting the greater sensibility and the greater field of view could expand the database of high-redshift blazars.

6.3 EBL correction through ALPs

In light of the current data, it was decided to actually quantify the possible contribution of ALPs on the emitted spectra. To do this I created a Python program based on the theoretical model of Galanti, Roncadelli and De Angelis (21). As seen in chapter 2, the ALPs most characteristic feature is to couple to two photons with a coupling constant $g_{a\gamma\gamma}$ according to the Feynman diagram shown in Fig. 6.16.
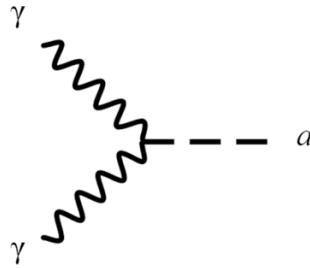
Figure 6.16: Photons-photos-ALP vertex with coupling constant $g_{a\gamma\gamma}$.

Clearly, in the presence of the extragalactic magnetic field B one photon line in Fig. 6.16 represents the B field, while the other photon line the E field of a propagating photon, and so we see that in such a situation energy-conserving conversions between VHE gamma-rays and ALPs take place. Because these conversions repeatedly occur as a photon/ALP beam emitted by the source propagates towards us, photon-ALP oscillations show up. Accordingly, photons acquire a split personality, travelling for some time as real photons, which suffer from EBL absorption, and for some time as ALPs, which are unaffected by the EBL.

Taking together the effects of EBL and photon/ALP conversion in the intergalactic magnetic field (IGMF), lead to a double process: an attenuation and an enhancement of the photon flux at Earth, depending on distance, magnetic fields and energy considered. As mentioned, the enhancement in the flux is possible since ALPs travel without obstruction through the EBL, and a fraction of them can convert back into photons before reaching the Earth. However, the ALP mechanism can also lead to a further attenuation of the photonic flux due to the loss of photons detected as they are transformed into ALPs.

Considering ALPs, the $\tau_\gamma(E_0, z)$, chosen before to be equal to $\tau_\gamma^{FR}(E_0, z)$, gets replaced by the effective optical depth $\tau_\gamma^{ALP}(E_0, z)$ which is almost always smaller than $\tau_\gamma^{FR}(E_0, z)$ and

$\tau_\gamma^{ALP}(E_0, z)/\tau_\gamma^{FR}(E_0, z)$ turn to be a monotonically decreasing function of both E_0 and z. Therefore, using ALP equation the formula (6.5) gets replaced by:

$$P_{\gamma \to \gamma}^{ALP}(E_0, z) = e^{-\tau_\gamma^{ALP}(E_0, z)} \qquad (6.11)$$

For clarity, the term "intrinsic spectrum" will be used when referring to the correct one with ALP hypothesis (in order not to confuse it with the emitted spectrum).

The crux of the argument is that even a small decrease of $\tau_\gamma^{ALP}(E_0, z)$ with respect to $\tau_\gamma^{FR}(E_0, z)$ gives rise to a large increase of the photon survival probability as compared to the case of CP. So, the main consequence of photon-ALP oscillations is to substantially attenuate the EBL absorption, thereby enlarging the cosmic transparency above $E_0 \gtrsim 500\, GeV$. It goes without saying that all this takes place for a specific set of allowed values of the model parameters. The first input parameter is the ALP mass, which was set at $m_{ALP} = 10^{-10} eV$. A value in good agreement with astrophysics bound found in literature [(44), (45)].

A second very important parameter is the extragalactic magnetic field B. The photon and ALP transfer functions could be easily calculated if we knew the exact configuration of the magnetic field along the line of sight to a gamma-ray source. Unfortunately, our knowledge of extragalactic magnetic fields is limited (116), and not even the approximate strength and coherence length are known. We have to rely on models of extragalactic magnetic field to study the impact of photon-ALP oscillations on the photon propagation. According to the studies of Rees and Setti (117) and soon thereafter by Hoyle (118), the existence of energetic quasar outflows should give rise to extragalactic magnetic fields, since the ejected material is ionized and so the magnetic flux lines are frozen in. For this model the outflows form bubbles with magnetic fields that typically spread over ~ 4 Mpc with field strengths of the order of 1 nG. Another idea was put forward in 1999 by Kronberg, Lesch and Hopp (119), which consists in galactic superwinds emitted by primeval galaxies ($z > 6$) which magnetize the extragalactic space and produce magnetic fields in the $0.1\, nG < B < 1\, nG$ range on the Mpc scale, in agreement with observations of Lyman-alpha forest clouds (120), Faraday rotation measures (121) and other constraints (122). Because these models predict statistical properties of the magnetic field, they can be used to infer the probability distribution of the photon and ALP transfer functions. This is achieved by simulating a large number of magnetic field configurations along the line of sight and solving the propagation equations for each of the generated field configurations individually. The mean and variance of the transfer functions is obtained by aggregating the data. This approach is computationally demanding but flexible with regards to the magnetic field input. Furthermore it is a more general model, in fact it is also used considering ALPs coming from supernovae (123) (124) and quasar (125).

Alternatively, extragalactic magnetic fields may originate from inflation, in which case the magnetic field power spectrum could be scale-invariant at large scales [(126), (116), (127)]. However, this hypothesis concerns cosmological distances.

As seen in chapter 2, the ALP correction model predicts that B is modelled as a domain-like network, where B is homogeneous over a domain of size L_{dom}. The strength B changes slightly in all domains, but its direction changes randomly from one domain to the next. An upper limit of 1.7 nG was also placed on the extragalactic magnetic field in the study by Psjirkov et al. of 2016. For these reasons B around 1 nG was chosen even if, in Galanti's theoretical model, its value is strictly connected to $g_{a\gamma\gamma}$. In fact, the second free parameter of the model is ξ, defined by the product of the magnetic field and the coupling constant:

$$\xi \equiv \left(\frac{B}{1\,nG}\right)\left(g_{a\gamma\gamma}10^{11}GeV\right) \qquad (6.12)$$

This dimensionless value is used to quantify the intensity of the ALP contribution: however, there is no linear relationship but a more complex contribution that we will see shortly. The last free parameter of the program is the coherence length L_{dom}: Galanti et al. model suggest the range $1\,Mpc \lesssim L_{dom} \lesssim 10\,Mpc$. This analysis is framed within the standard ΛCDM cosmological model with $\Omega_M = 0.3$ and $\Omega_\Lambda = 0.7$, and so the redshift is the natural parameter to express distances. Therefore the individual intervals are constant in redshift and not in the distance in Mpc proper. The coherence length of the magnetic field was set at $\Delta z = 0.001$, which correspond to approximately, for $z = 0$, $L_1 = 4.27\,Mpc$, obtained by[5]: $L(z_a, z_b) = 2.96 \times 10^3 \ln\left(\frac{1+1.45\,z_b}{1+1.45\,z_a}\right)$. Therefore, the path up to the source PG 1553+113 ($z = 0.5$), will be divided into 500 intervals of slightly different size in Mpc. As said previously, the magnetic flux lines can be thought as frozen inside the IGM medium because of the high conductivity. Therefore, flux conservation during the cosmic expansion entails that B scales like $(1 + z)^2$, so that the magnetic field strength in a domain at redshift z is $B(z) = B(z = 0)(1 + z)^2$.

As seen in chapter 2, we can distinguish three cases of different mixing regime based on the energy value compared to the low-energy threshold E_L and high-energy threshold E_H. Using formulas of chapter 2 with data used for this analysis and $g_{a\gamma\gamma} = 10^{-11}GeV^{-1}$, the threshold energies are: $E_L \cong 10\,GeV$ and $E_H \cong 840\,GeV$. The range of this interval (ΔE) is however very sensitive to the variation of the coupling constant since $E_L \propto g_{a\gamma\gamma}^{-1}$ and $E_H \propto g_{a\gamma\gamma}$. Most of the spectral data falls within

---

[5] It is an approximation of the formula: $L(z_a, z_b) = \int_{z_a}^{z_b} dz\, \frac{dl(z)}{dz} \cong 4.29 \times 10^3 \int_{z_a}^{z_b} \frac{dz}{(1+z)[0.7+0.3(1+z)^3]^{1/2}}\, Mpc$

this range so it is correct to assume that we are in strong mixing conditions. In this regime the conversion probability in the single domain is of the order of 0.1-0.5, so we expect that along the entire journey there are several transpositions from photon to ALP. Above E_H, the conversion probability decreases very quickly as the energy increases but for the values used in this thesis (photons observed up to some TeV) this probability is still considerable. In fact, it is not necessary to have a conversion probability of a few tenths to have visible effects in the spectrum since each beam crosses a large number of domains. Therefore even photons of several tens of TeV can generate significant corrections to the spectrum. However, for these particularly energetic photons the CMB dispersion term $\propto E$ (which will be described later) dominates with respect to the term at E = constant. The oscillation length in strong-mixing regime is:

$$l_{osc} \cong \frac{2\pi}{g_{a\gamma\gamma} B} \tag{6.13}$$

corresponding to $\sim 200\ Mpc$ using $g_{a\gamma\gamma} = 10^{-11} GeV$ and $B = 1\ nG$. Since $l_{osc} \gg L_{dom}$, even a smooth transition from one domain to another would be perceived as abrupt and non-adiabatic by the photon-ALP system, which justified the approximation of discontinuous transitions between the domains.

Since we are clearly in the regime $E \gg m_a$ the photon/ALP beam propagation equation (2.4) of chapter 2 can be rewritten as Schrodinger-like equation with t replaced by the coordinate y along the beam:

$$\left(i\frac{d}{dy} + E + \mathcal{M}(E, y)\right)\psi(y) = 0, \tag{6.14}$$

assuming that the monochromatic photon/ALP beam of energy E travels along the y direction in a magnetic field. The vector $\psi(y) = \begin{pmatrix} \gamma_1(y) \\ \gamma_2(y) \\ a(y) \end{pmatrix}$ where $\gamma_1(y)$ and $\gamma_2(y)$ are the photon amplitudes with polarization along the x and z axis, respectively, while $a(y)$ is the ALP amplitude. The $\mathcal{M}$ matrix, already encountered in chapter 2, is the mixing matrix. It is very important because it contains all the factors that correct the observed spectra. This matrix depends on three parameters:

$$u(E) \equiv -\frac{m_a^2}{2E} \tag{6.15}$$

$$v(y) \equiv \frac{g_{a\gamma\gamma}B_T(y)}{2} \tag{6.16}$$

$$w(E) \equiv w_1(E) + w_2(E) + \frac{i}{2\lambda_\gamma(E)} \tag{6.17}$$

with $w_1(E) \equiv -\frac{w_{pl}^2}{2E}$ and $w_2(E,y) \equiv \left[1.42 \times 10^{-4}\left(\frac{B_T(y)}{B_{cr}}\right)^2 + 0.522 \times 10^{-42}\right]E$. Without going into detail on how these equations were obtained and how to solve eq. 6.15 (for more details see (21)), it is important to understand the different contributions. The axion mass as said is a free parameter but according to current research would be around $10^{-10}\ eV$: this parameter is critical in constraining the low-energy threshold, which the strong mixing starts. A rather negligible term, in this context, because extremely small is the plasma frequency (w_{pl}). This parameter was set at $10^{-29}\ GeV$, as suggested by several studies (1). Another relatively small term in this context is the first term in $w_2(E,y)$: it takes into account the one-loop QED vacuum polarization. This term is damped by the critical magnetic field $B_{cr} \simeq 4.41 \cdot 10^{13}\ G$ [(128), (129) (130)]. The second term in $w_2(E,y)$ is the photon dispersion on the CMB (131).

The dominant factors are $v(y)$ and the mean free path $\lambda_\gamma(E)$. From the comparison between analytical and numerical models performed by Galanti and Roncadelli (21), it results that the transverse magnetic field can be estimated on average $B_T = \sqrt{2/3}\ B$. In any case, having no certain values of B, the value around $1\ nG$ is a good estimate. As mentioned, the value of the magnetic field is strictly linked to the coupling constant. In fact, the product of the two terms (ξ) enters the mixing matrix, which makes it practically impossible to distinguish the contribution of the two components individually. The second dominant factor is the mean free path $\lambda_\gamma(E)$ for the reaction $\gamma\gamma \to e^+e^-$: so, it comes into play taking EBL-absorption into account. The $\lambda_\gamma(E)$ value can be estimated by considering two similar sources with same flux located at both edges of the n-th domain along the line of sight. Applying equations 6.4 and 6.5 to these sources and drop cosmological evolutionary effects in a single domain because the domain size is so small compared to cosmological standards, the mean free path of the n-domain results:

$$\lambda_\gamma^{(n)}(E_0) = \frac{L_{dom}^{(n)}}{\tau_\gamma(E_0,n\Delta z)-\tau_\gamma(E_0,(n-1)\Delta z)} \tag{6.18}$$

where the optical depth is again evaluated by Franceschini's EBL model (54). The program has therefore worked on each domain as described in the previous lines, finding the values that

characterize it. The only variable within the mixing matrix is the angle that defines the direction of the magnetic field with respect to the direction of the photons. This value was randomly generated in each domain. The program has therefore found the solution (U_n) of equation 6.15 in each domain. To consider the entire path from the source to us, we proceeded, as described by the model, by running the production of solutions (U_n) along all the domains. Finally, the photon survival probability was calculated (with eq. (38) of (1) "supplementary material") assuming that the emitted beam consists 100% of unpolarized photons. This whole process, called realization, is done using a random angle for each domain. However, this value can greatly influence the final result, so, to obtain an accurate survival probability, it is necessary to mediate over a very large number of realizations (I take 5000 realizations) randomly choosing the values of all angles for every realization. Taking the arithmetic mean of the individual survival probabilities, we found the average probability $P_{\gamma \to \gamma}^{ALP}$: this value is the best estimate we can obtain even if clearly this is not what happens, since the beam follows a single realization of the considered stochastic process at once. Given the huge number of realizations, the program takes a long time to perform the correction, therefore I used the Atacama super-computer located at the University of Padua.

To confirm that some values, although present, are not very significant in the ALP correction, it can be noted that by setting extremely small values of ξ, the plot of the spectrum produced by the ALP correction program matches perfectly with the EBL-photon correction model. An example of this is shown in Fig. 6.17, where the PG 1553 + 113 source was analyzed with the HESS data, the value of $\xi = 0.005$, $L_1 \cong 4.27\ Mpc$ ($\Delta z = 0.001$) and $m_{ALP} = 10^{-10} eV$. As you can see in the figure, the green curve that describes the spectrum emitted in CP and the blue one that takes into account the ALP correction, are so similar that they are completely overlapped. This means that if ξ is small the m_{ALP} and the w_{pl} are not enough to generate enough spectrum changes. The most significant values for the ALP correction program are the magnetic field and the coupling constant, both contained in ξ. Since the green and blue fits were obtained using different programs, this also served as a verification of the correctness of the two programs.
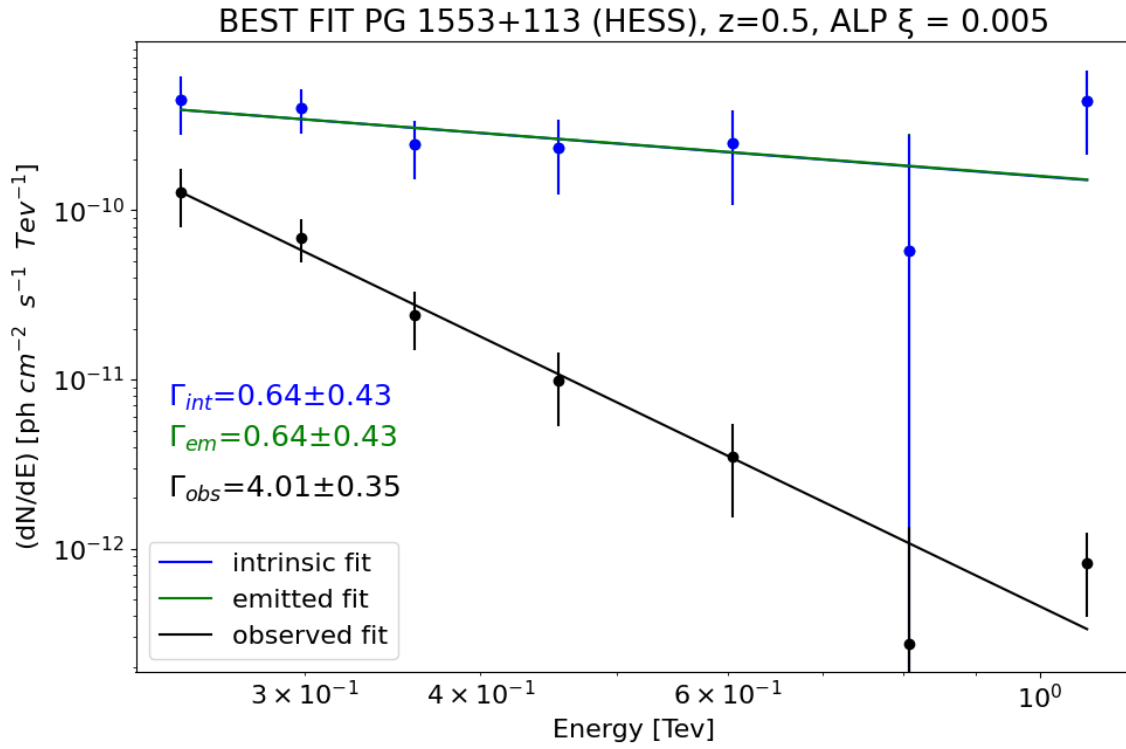
Figure 6.17: PG 1553+113 spectrum obtained from HESS data. The observed, emitted and intrinsic spectra ($\xi = 0.005$) are shown in black, green and blue respectively. The corresponding spectral indices, generated by the Python program, are illustrated in the plot.

By placing values of ξ more similar to expectations, such as for example $B = 1 \, nG$, $g_{a\gamma\gamma} = 10^{-11} GeV^{-1}$ ($\xi = 1.0$), the ALP correction is much more significant, see Fig. 6.18.
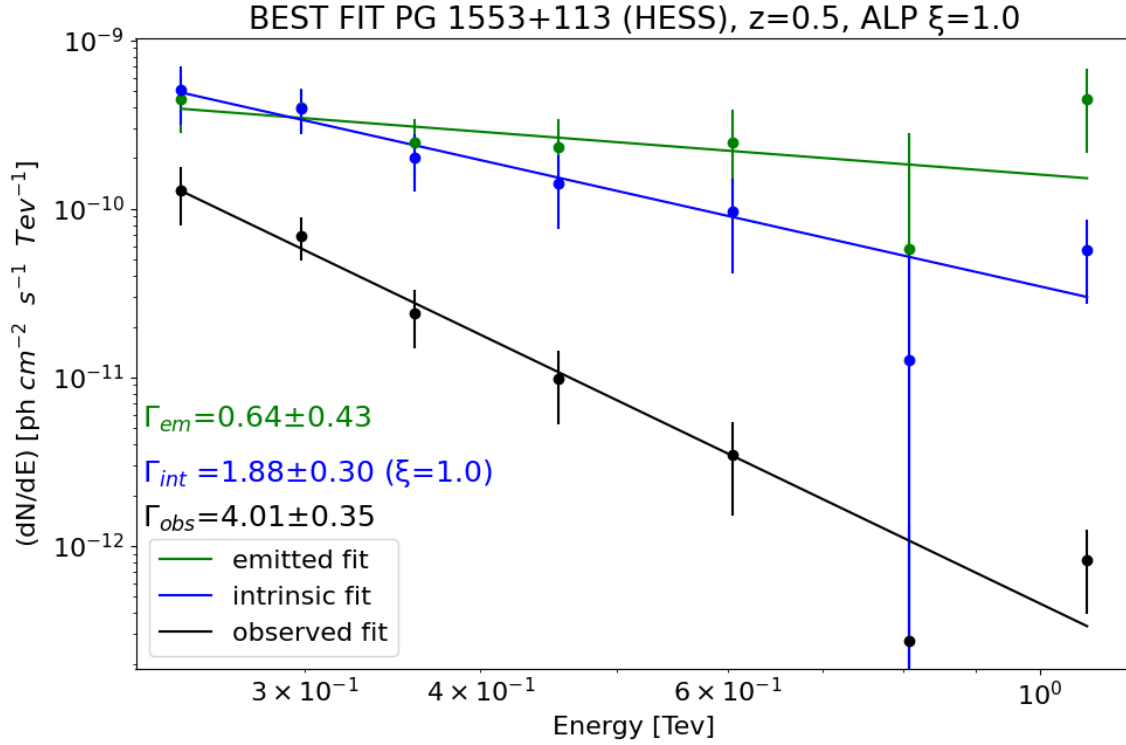
Figure 6.18: PG 1553+113 spectrum obtained from HESS data. The observed, emitted and intrinsic spectra ($\xi = 1.0$) are shown in black, green and blue respectively. The corresponding spectral indices, generated by the Python program, are illustrated in the plot.

The best fit values for the ALP correction, always obtained with the program described above, are shown in Table 3. It can be seen that at energies lower than $300\ GeV$ the intrinsic spectrum has a flux greater than that emitted, while at higher energies the opposite happens. This is due to the combined effect of EBL and ALP. EBL simply absorbs photons while ALPs, due to their lack of interaction with matter, produce two effects on the flux: that of damping the absorption due to the EBL but also a decrease in flux due to the fact that the photons in the form of ALP cannot be detected by telescopes. At low energies, where the absorption of photons by EBL is not very marked, the second factor prevails, therefore there will be a greater "absorption" due to ALPs compared to the case of conventional physics. Instead, as seen in chapter 3, above $300\ GeV$ the damping for EBL is much more efficient therefore the main contribution of the ALPs is to prevent photons from being absorbed: therefore an effective mean free path of photons (in the presence of interaction with le ALP) larger than in the case of EBL alone.

The combined result of the two processes is a softer spectrum than CP. This type of correction has not been made only for $\xi = 1.0$ but also for four other values of ξ: 0.1, 0.5, 2.0, 5.0. In Figure 6.19 it

is possible to compare the different contributions for PG 1553+113 observed with VERITAS. As long as ξ has low values (blue line) the spectrum corresponds to the spectrum in CP condition, but already for $\xi = 0.5$ (yellow line) a variation of the low energy spectrum is noted. As mentioned, this variation is to be associated with photons not perceived by the detectors. By further increasing the contribution of B or $g_{a\gamma\gamma}$, it is noted that even the most energetic part of the spectrum is corrected due to the decrease in the photon-EBL interaction. It would seem that increasing ξ the spectrum tends to become softer, but in reality this is not always true, because the probability of photon-ALP conversion under strong mixing regime conditions in the single domain is: $P_{\gamma \to a}(L_{dom}) \simeq \sin^2\left(\frac{g_{a\gamma\gamma} \, B \, L_{dom}}{2}\right)$ therefore it oscillates due to the sine function. However, for small values of ξ the sine argument becomes very small and therefore for Taylor the approximation $\sin x \to x$ is valid. In fact, observing the first columns of Table 3, it can be seen that as the parameter ξ increases, the ALPs contribution is increasingly influential in the modification of the spectrum.
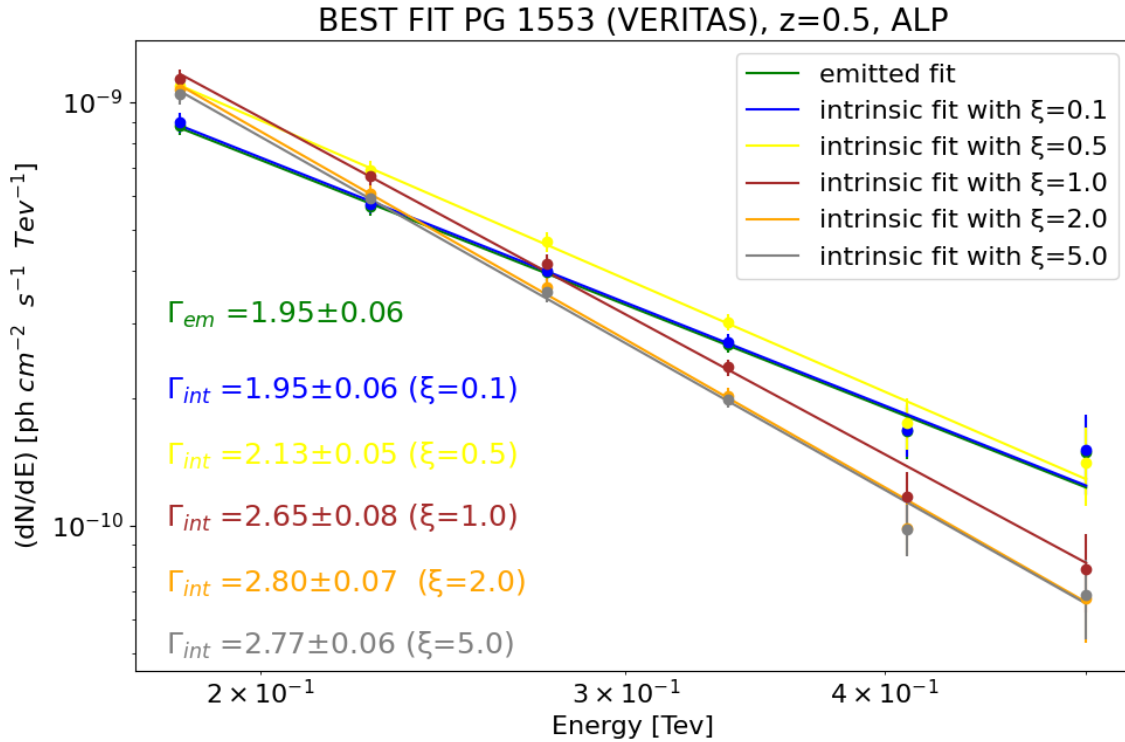
Figure 6.19: PG 1553+113 spectrum obtained from VERITAS data. The different values of ξ are shown in the legend. The corresponding spectral indices, generated by the Python program, are illustrated in the plot.

It should also be noted that the conversion probability varies from one domain to the next: in fact, both L_{dom} and, above all, the magnetic field have different values in different domains. Fig. 6.20 shows the conversion probability, as a function of the energy, for two different domains: $z = 0.001$ (blue curve) and $z = 0.467$ (red curve). Since the magnetic field is bigger at high redshift, the conversion probability increases moving away from us. In fact, the red line is upper than the blue. The gray line is indicative of $P_{\gamma \to a}(L_{dom}) \simeq \sin^2\left(\frac{g_{a\gamma\gamma} B L_{dom}}{2}\right)$ using $\xi = 5.0$ and L_1. It has been indicated to confirm how this function is well representative of the data used in this thesis; in fact, it matches almost perfectly with the blue line between ten and a thousand GeV.
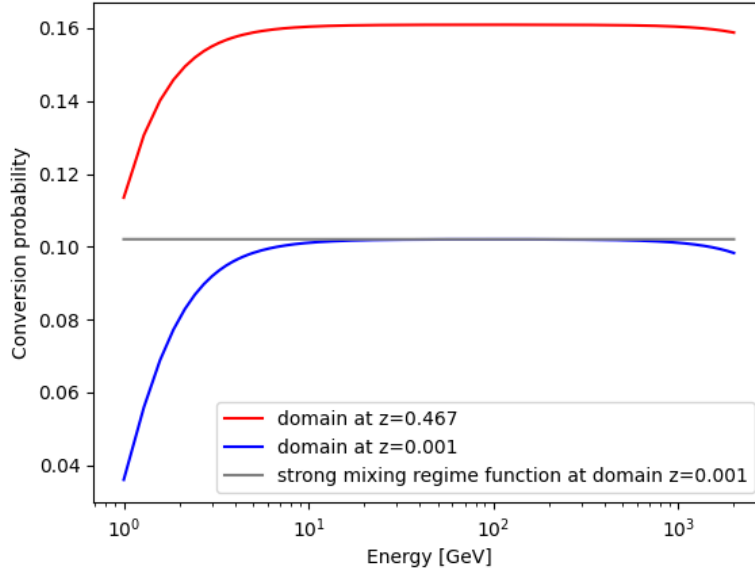
Figure 6.20: $\gamma \to a$ conversion probability function for two different domains: $z = 0.001$ and $z = 0.467$. The gray line shows the strong mixing regime at domain $z = 0.001$.

The correction using the values of ξ: 0.1, 0.5, 1.0, 2.0, 5.0 was applied to all the spectra examined. It may be interesting to compare this correction also for a low redshift source such as Markarian 180, observed with the MAGIC telescope. In this case, only two spectral corrections are shown in Figure 6.21 to make the plot clearer. In fact, for $\xi = 0.1$ and $\xi = 0.5$ the spectrum is very similar to the fit emitted (green line). However, it is also possible to observe the other spectral parameters from Table 3. The gray best fit indicates the analysis for $\xi = 5.0$ while the red line for $\xi = 1.0$. What is to be emphasized is that the ALP corrections, regardless of the value of ξ, provide an intrinsic flux greater than that in CP. This means that the source is too close to us to highlight the contribution of the lack of EBL-ALP interaction. The loss of photons due to the conversion to ALP prevails. However, the

spectrum is softer because the more energetic photons have a greater opacity than EBL and therefore the EBL-ALP no interaction is more influential than at low energies. To confirm this, we can see some values. The gray line intrinsic flux for the photons of lower energy ($E_1 = 0.183\,TeV$) is: $\Phi_{int,5.0}^{ALP}(E_1) \cong 2.98 \cdot 10^{-10} cm^{-2} s^{-1} TeV^{-1}$, and for those of higher energy ($E_4 = 1.310\,TeV$) it is: $\Phi_{int,5.0}^{ALP}(E_4) \cong 8.06 \cdot 10^{-13} cm^{-2} s^{-1} TeV^{-1}$. In the same way the fluxes for the green line are: $\Phi_{em}^{CP}(E_1) \cong 1.98 \cdot 10^{-10} cm^{-2} s^{-1} TeV^{-1}$ and $\Phi_{em}^{CP}(E_4) \cong 6.09 \cdot 10^{-13} cm^{-2} s^{-1} TeV^{-1}$. So, the ALP correction at E_1 is $\Delta\Phi(E_1) = \Phi_{int,5.0}^{ALP}(E_1) - \Phi_{em}^{CP}(E_1) = 10^{-10} cm^{-2} s^{-1} TeV^{-1}$, while at E_4 is: $\Delta\Phi(E_4) = 1.97 \cdot 10^{-13} cm^{-2} s^{-1} TeV^{-1}$. The correction due to ALPs contribution is much more influential at low energies for low redshift sources.
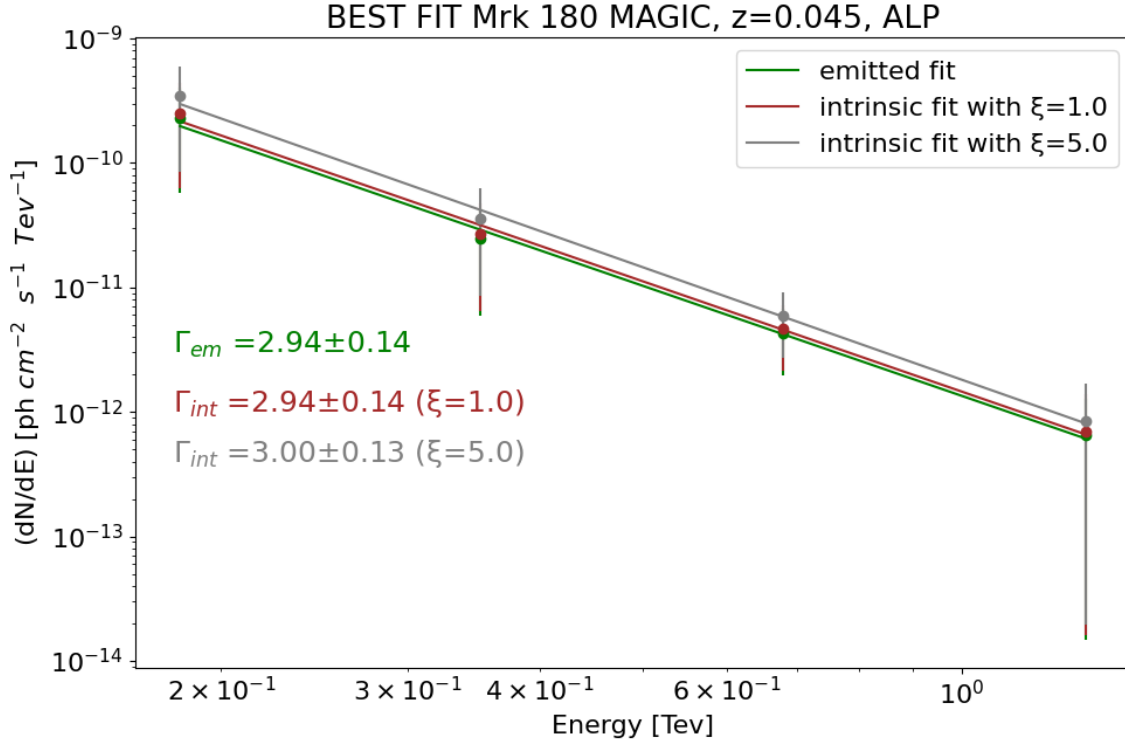
Figure 6.21: Mrk 180 spectrum obtained from MAGIC data. The different values of ξ are shown in the legend. The corresponding spectral indices, generated by the Python program, are illustrated in the plot.

The spectral index-redshift plot obtained for the EBL correction was replicated for each value of ξ. Is the trend horizontal this time? The results using all the analyzed sources and $\xi = 0.1$, are reported in Fig. 6.22. As in the previous case, the sources of uncertain redshift are indicated with a white circle. The red line and the blue parabola are the best fit functions of degree 1 and 2 respectively, in same

way the black dashed horizontal line is the best fit of degree 0. The reference curve considering all sources (blue curve in Fig. 6.9) is also indicated in pink. As imaginable, the intrinsic and emitted trend are very similar because in this case (low value of ξ) the ALP correction modifies the spectra only a little.
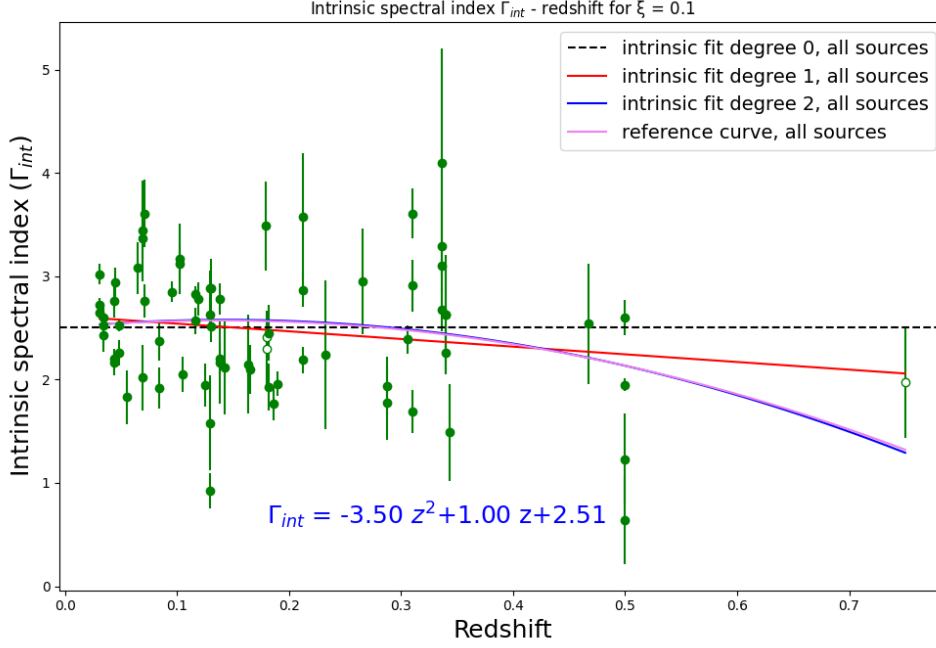
Figure 6.22: Scatter plot between intrinsic VHE spectral index of all BL Lacs with redshift (with $\xi = 0.1$). The red and blue solid lines are the best-fit straight line and parabola respectively. The dashed line is the best-fit of degree zero. It is also illustrated the equation of the curve with the best reduced chi-square. In pink the reference curve considering all sources. The spectral indices of this plot are summarized in Table 3.

The same graph was replicated for all ξ in Figures 6.23. By increasing ξ we see how step by step the red and blue curves show higher Γ_{int} at high redshift. In fact, the two curves move further and further away from the reference curve. The curves with the best reduced chi-square have always reported their equation in the plots. The values of the best $\tilde{\chi}^2$, with the respective fit parameters, are shown in Table 4. Calculating for example the difference between Γ_{int} of the reference curve and that of the curve with the best $\tilde{\chi}^2$ at $z = 0.5$, it results: $\Delta_{0.5,\xi=0.1} = 0$, $\Delta_{0.5,\xi=0.5} = 0.15, \Delta_{0.5,\xi=1.0} = 0.43, \Delta_{0.5,\xi=2.0} = 0.73, \Delta_{0.5,\xi=5.0} = 0.71$. As predicted by the theory, the contribution of ALPs increases the average value of the intrinsic spectral indices, especially for high redshift sources.

Table 4:

ξ	$\tilde{\chi}_0^2$	$\tilde{\chi}_1^2$	$\tilde{\chi}_2^2$	$ndof$ $(best\ \tilde{\chi}^2)$	$|c|$ $(best\ \tilde{\chi}^2)$
0.1	8.96	8.50	8.38	70 (parabola)	0.96
0.5	8.44	8.04	8.09	71 (straight line)	0.72
1.0	6.82	6.84	6.88	72 (horizontal line)	
2.0	6.74	6.51	6.60	71 (straight line)	0.70
5.0	9.90	9.78	9.91	71 (straight line)	0.71

Intrinsic spectral index Γ_{int} - redshift for ξ = 0.5

Γ_{int} = (-0.64 ± 0.30) z+ (2.60 ± 0.07)

Intrinsic spectral index Γ_{int} - redshift for ξ = 1.0

$\Gamma_{int} = 2.57 \pm 0.05$

Intrinsic spectral index Γ_{int} - redshift for ξ = 2.0

$\Gamma_{int} = (0.60 \pm 0.32)\ z + (2.57 \pm 0.06)$
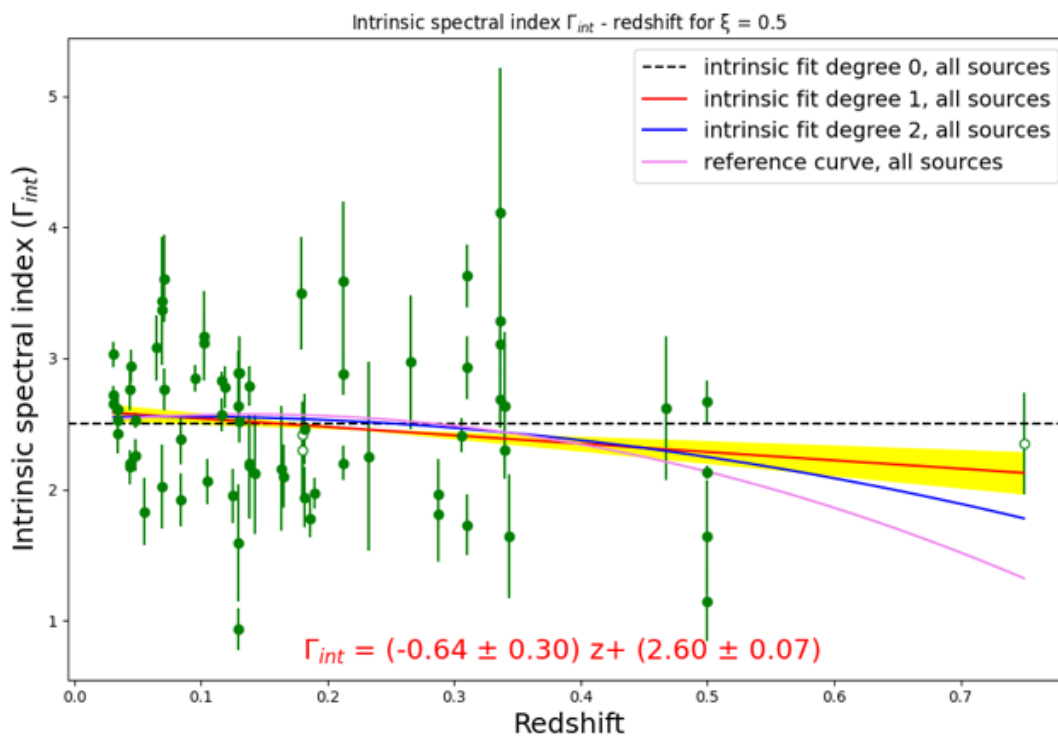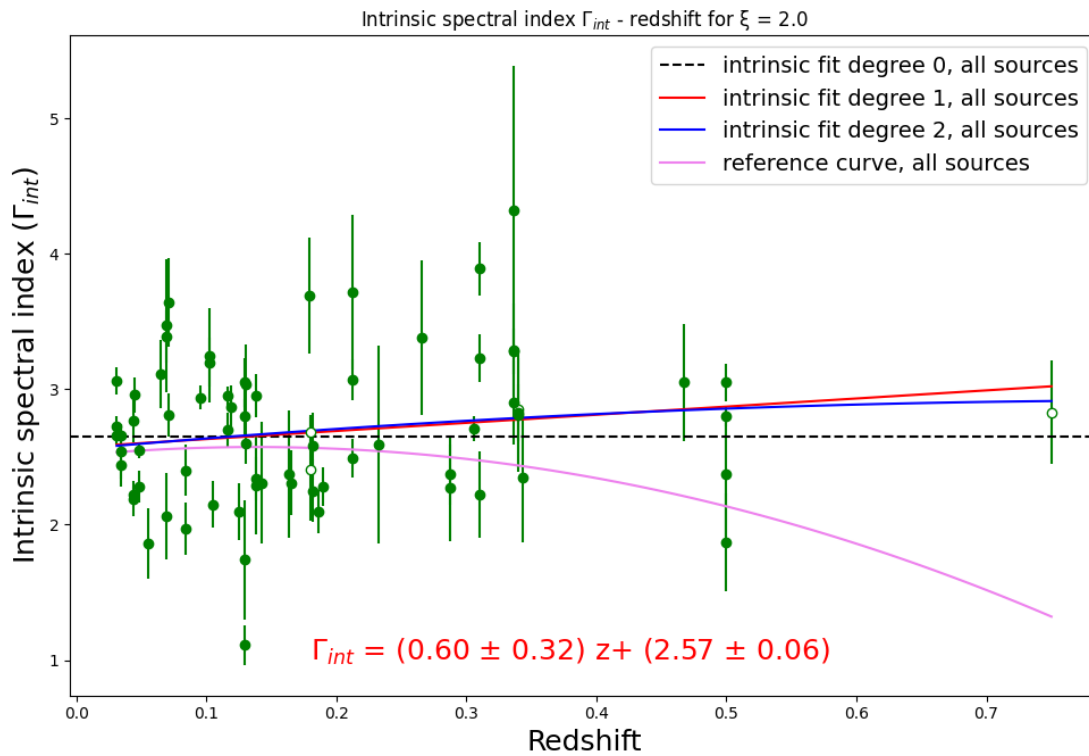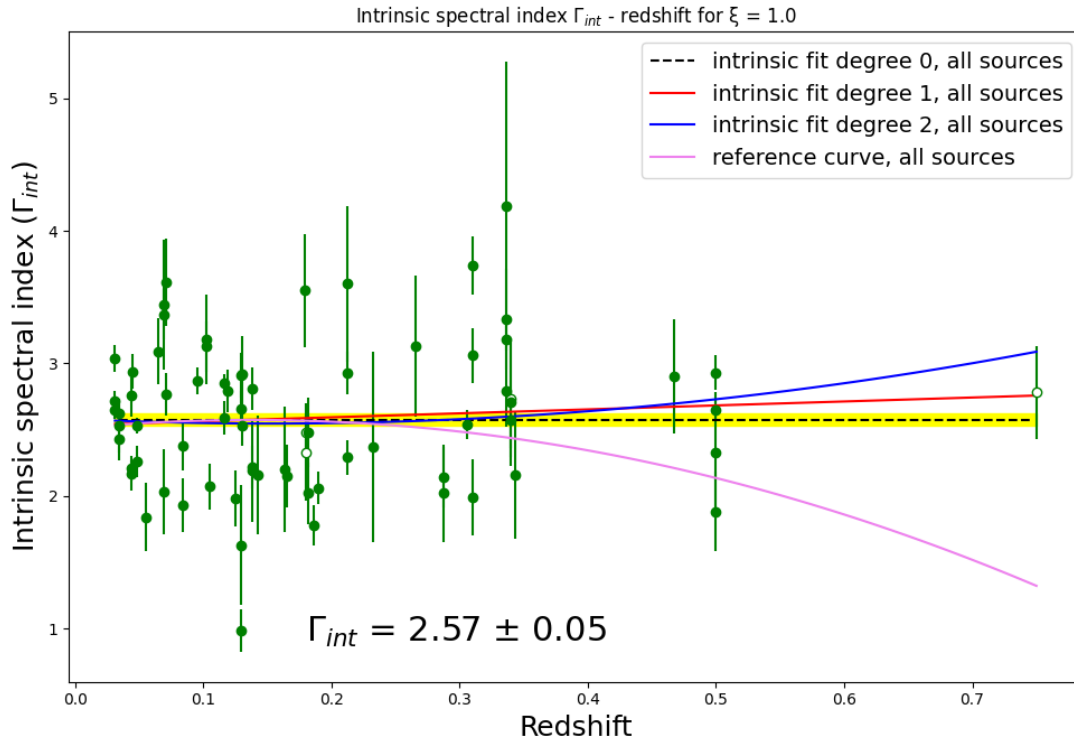
Figures 6.23: Scatter plots between intrinsic VHE spectral index of all BL Lacs with redshift. In title is also indicated the value of ξ used. The red and blue solid lines are the best-fit straight line and parabola respectively. The dashed line is the best-fit of degree zero. It is also illustrated the equation of the curve with the best reduced chi-square. In pink the reference curve. The spectral indices of this plot are summarized in Table 3.

We highlight the case $\xi=1$ in Fig.6.23 since it is very significant. In this case, the evolution with redshift is almost horizontal, as we expected. Note the huge difference compared to the reference curve in pink. The yellow area indicates the region between the line that adds the error to the best fit and the line that subtracts it. This error is obtained from the chi-square minimization procedure and is not to be confused with the error associated with the totality of the data described by $\tilde{\chi}^2$. Calculating the reduced chi-square values, it appears that the best fit curve is exactly that described by the horizontal axis! This is just what we expected to happen after applying the ALP correction.

Having said that, the value of $\tilde{\chi}^2$ are quite large since the sources are rather scattered within the plot. This is mainly due to the great variability of the sources. This represents a problem of difficult observational solution since these sources are almost always observable only in the flare phase: therefore, depending on the intensity of this event, there may be different spectral slopes. However, the fact of using several observations of the same source, carried out in different periods, favors the possibility of having made a good estimate of the average intrinsic value of the slopes of the individual sources.

Very similar plots were obtained taking into consideration only the z TeVCat sources (Fig. 6.24). Also in this situation the only case in which the horizontal axis represents the best fit is the one corresponding to $\xi = 1.0$. The values of the best $\tilde{\chi}^2$, with the respective fit parameters, are shown in Table 5. Galanti et al. (1) similarly confirmed the flattening of $\Gamma_{int}(z)$ for two different parameter sets: $\xi = 0.5$, $L_{dom} = 4\ Mpc$ and $\xi = 0.5$, $L_{dom} = 10\ Mpc$ (Fig. 6.25). Although for different parameters, both analyzes suggest the presence of ALPs.

Table 5:

ξ	$\tilde{\chi}_0^2$	$\tilde{\chi}_1^2$	$\tilde{\chi}_2^2$	$ndof\ (best-fit)$	$|c|\ (best-fit)$
0.1	9.46	9.00	8.82	66 (parabola)	0.97
0.5	8.92	8.50	8.51	67 (straight line)	0.71
1.0	7.20	7.23	7.28	68 (horizontal line)	
2.0	7.13	6.89	6.99	67 (straight line)	0.70
5.0	10.47	10.34	10.50	67 (straight line)	0.70

Intrinsic spectral index Γ_{int} - redshift for $\xi = 0.1$

$\Gamma_{int} = -4.17\ z^2 + 1.32\ z + 2.49$

Intrinsic spectral index Γ_{int} - redshift for $\xi = 0.5$

$$\Gamma_{int} = (-0.65 \pm 0.31) \, z + (2.61 \pm 0.07)$$

Intrinsic spectral index Γ_{int} - redshift for $\xi = 1.0$

$$\Gamma_{int} = 2.58 \pm 0.002$$
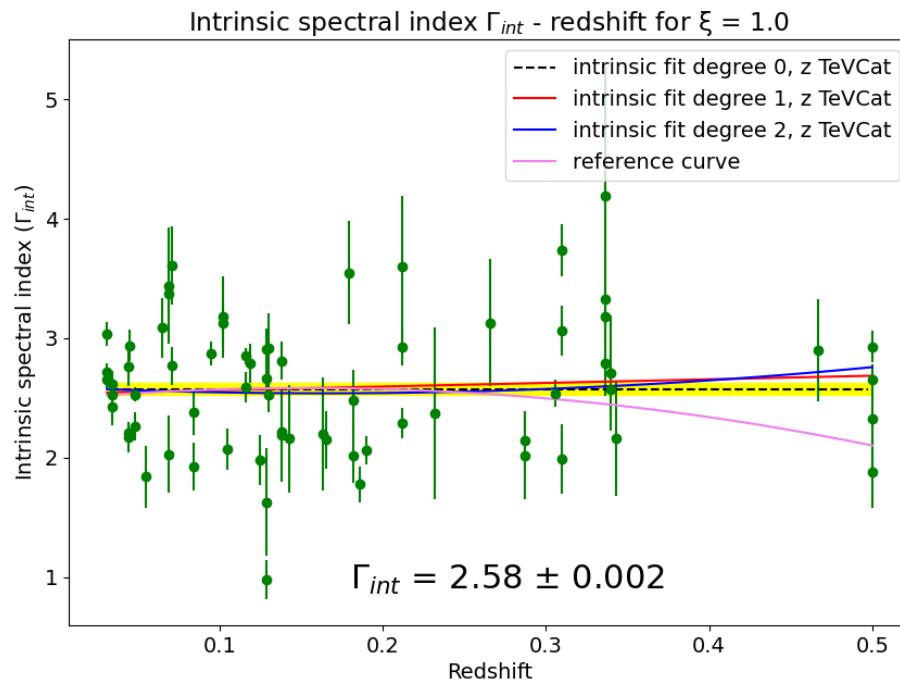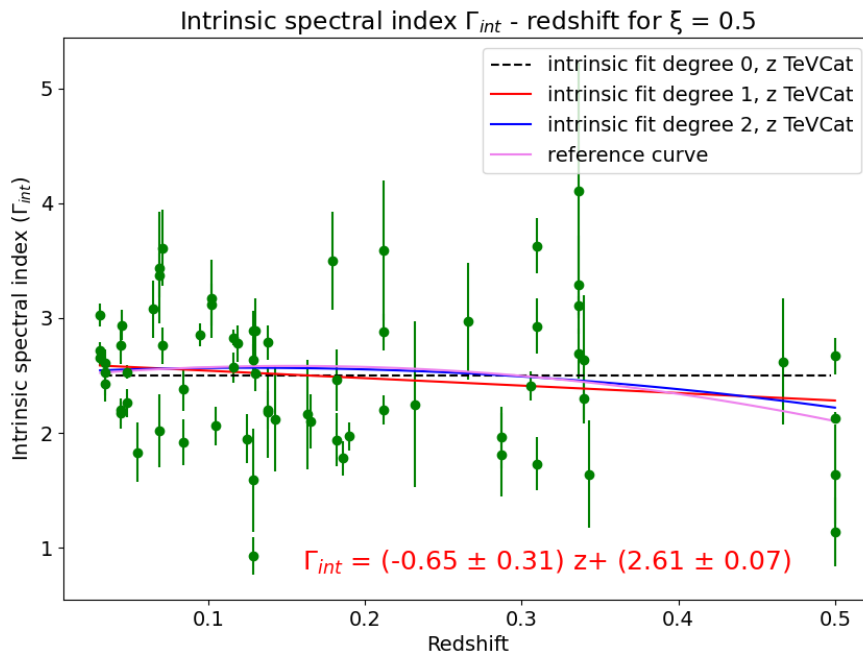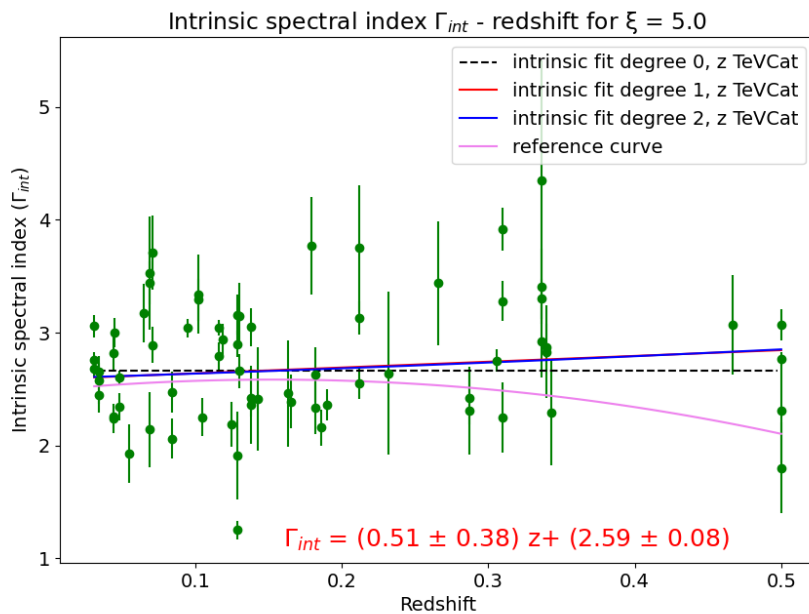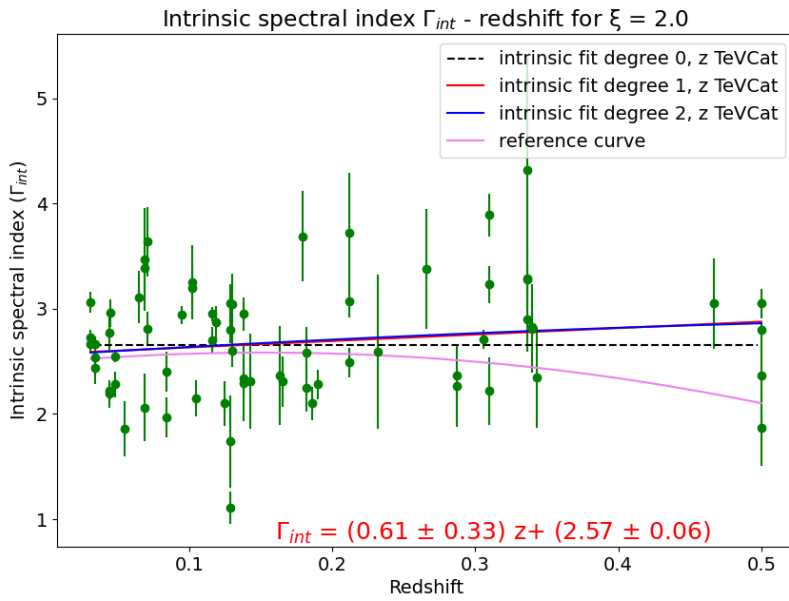
Figures 6.24: Scatter plots between intrinsic VHE spectral index of z TeVCat BL Lacs with redshift. In title is also indicated the value of ξ used. The red and blue solid lines are the best-fit straight line and parabola respectively. The dashed line is the best-fit of degree zero. It is also illustrated the equation of the curve with the best reduced chi-square. In pink the reference curve. The spectral indices of this plot are summarized in Table 3.
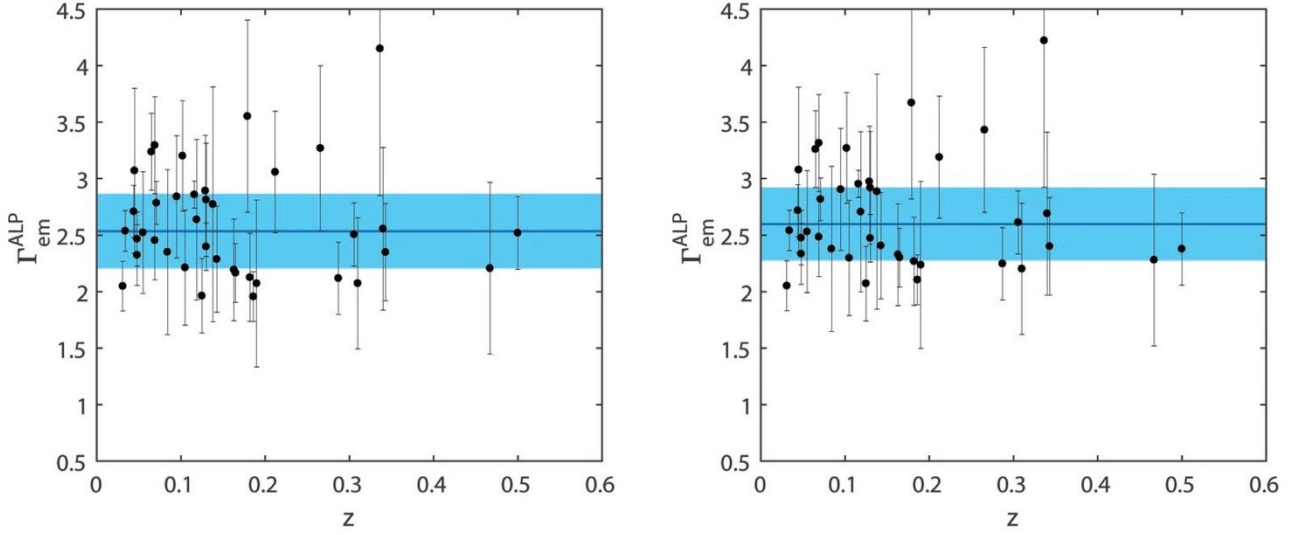
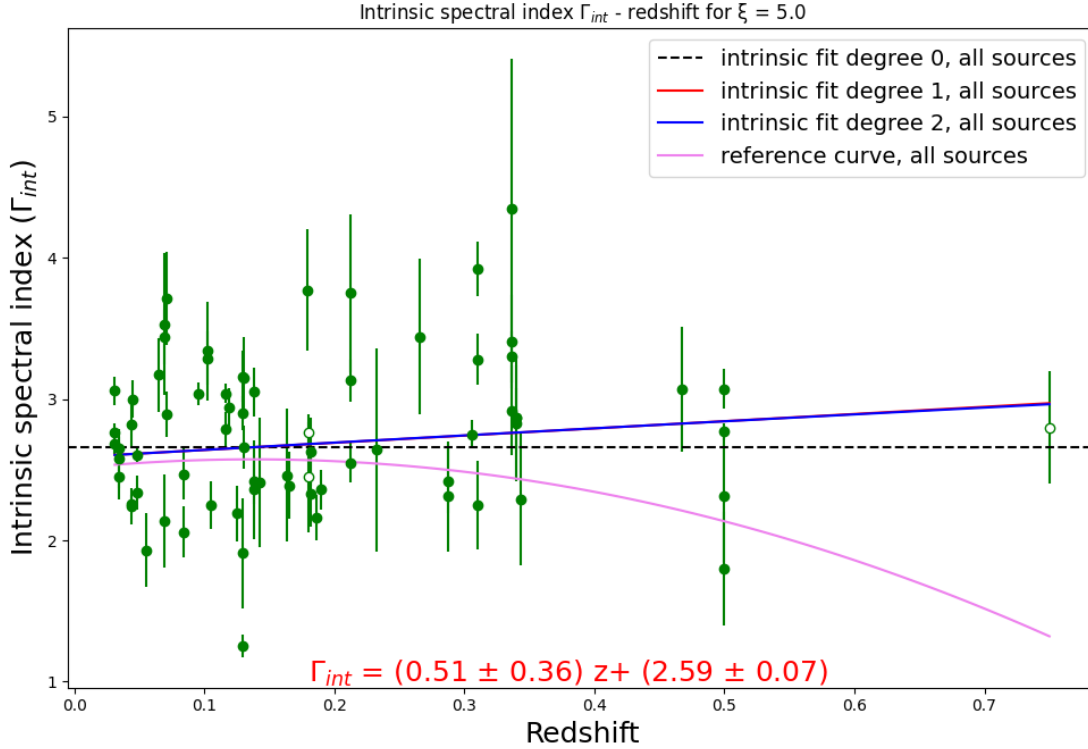Figures 6.25: Scatter plots between intrinsic VHE spectral index of BL Lacs analyzed by Galanti et al. with redshift. The light blue strip encompasses 95 per cent of the sources. In the left-hand panel the correction using $L_{dom} = 4\,Mpc$, in the right-hand the one using $L_{dom} = 10\,Mpc$. The horizontal straight best-fitting regression line are: 2.54 and 2.60, respectively. Both cases obtained for $\xi = 0.5$.

Finally, it was decided to re-make the plots just discussed using only one data per source. As for the other cases discussed, using $\bar{\Gamma}_{int}$ the only value in which the horizontal line describes the best fit is for $\xi = 1.0$. In order not to weigh the discussion down too much, only this case has been shown in Fig. 6.26 (for the other values of ξ see appendix). The values of the best $\tilde{\chi}^2$, with the respective fit parameters, are shown in Table 6.
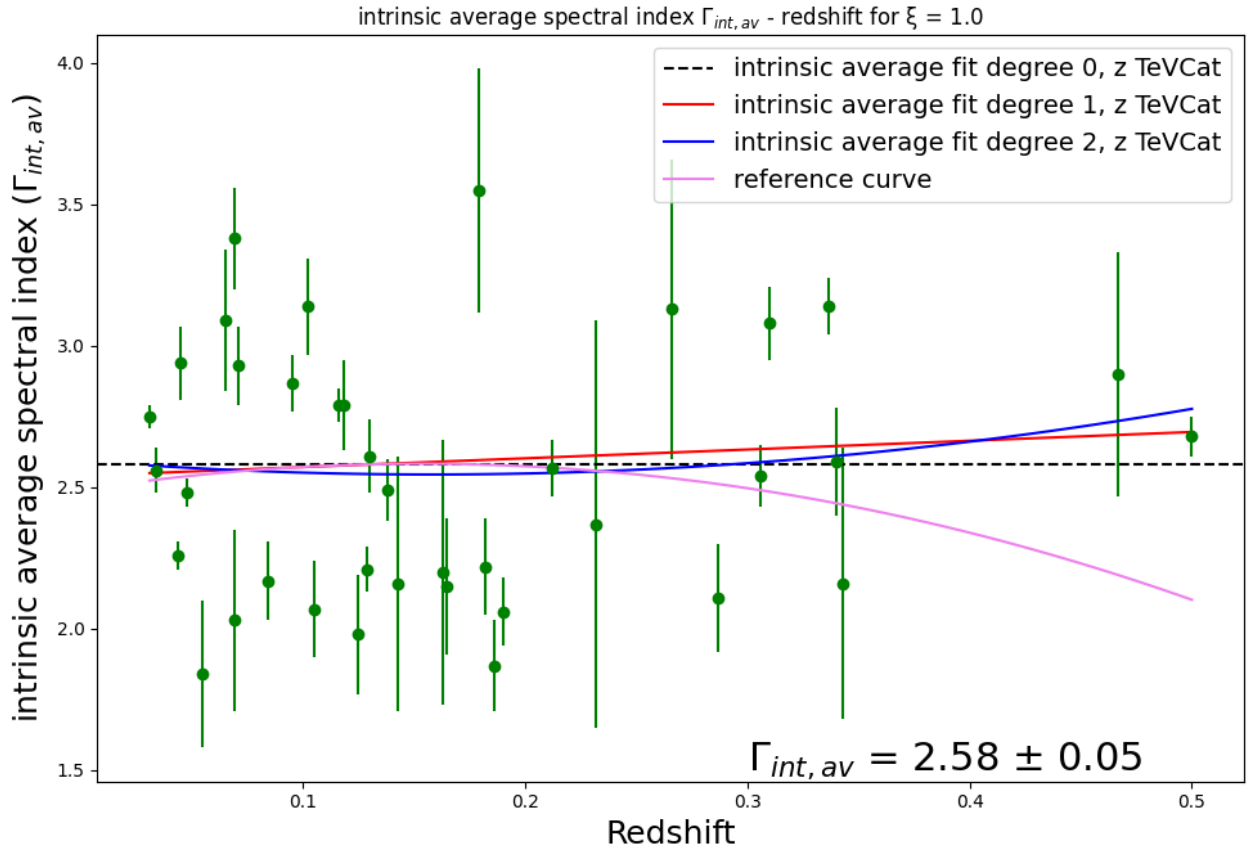
Figure 6.26: Scatter plot for $\xi = 1.0$ between average intrinsic VHE spectral index of z TeVCat BL Lacs with redshift. The red and blue solid lines are the best-fit straight line and parabola respectively. The dashed line is the best-fit of degree zero. It is also illustrated the equation of the curve with the best reduced chi-square. In pink the reference curve. The spectral indices of this plot are summarized in Table 8 as Method I.
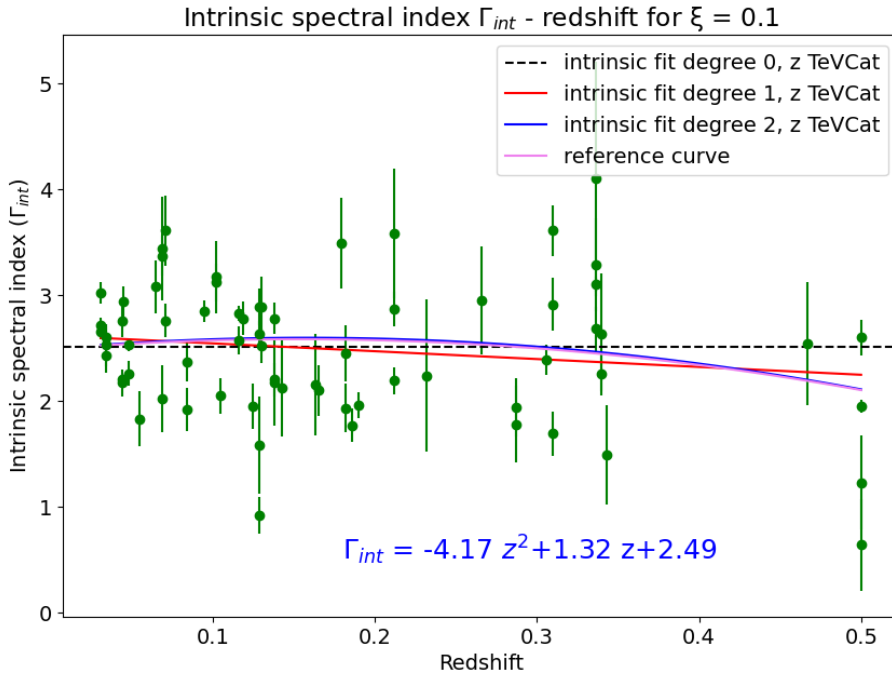
Table 6:

ξ	$\tilde{\chi}_0^2$	$\tilde{\chi}_1^2$	$\tilde{\chi}_2^2$	$ndof\ (best-fit)$	$|c|\ (best-fit)$
0.1	11.73	11.34	11.04	35 (parabola)	0.96
0.5	10.71	10.20	10.29	36 (straight line)	0.70
1.0	8.18	8.26	8.38	37 (horizontal line)	
2.0	8.31	7.89	8.11	36 (straight line)	0.70
5.0	12.08	11.91	12.24	36 (straight line)	0.70

Using $\bar{\Gamma}_{int,all}$, in the same way of $\bar{\Gamma}_{em,all}$, the plot in Fig. 6.27 illustrating their evolution with redshift for $\xi = 1.0$ is, as for the other cases, better described by the horizontal line: $\tilde{\chi}_0^2 = 4.37\ (ndof = 37)$. It is also important to note that the values of reduced chi-squares in this case are much lower than in

the other cases. The values of the best $\tilde{\chi}^2$, with the respective fit parameters, are shown in Table 7. The plots for the other values of ξ are shown in appendix.
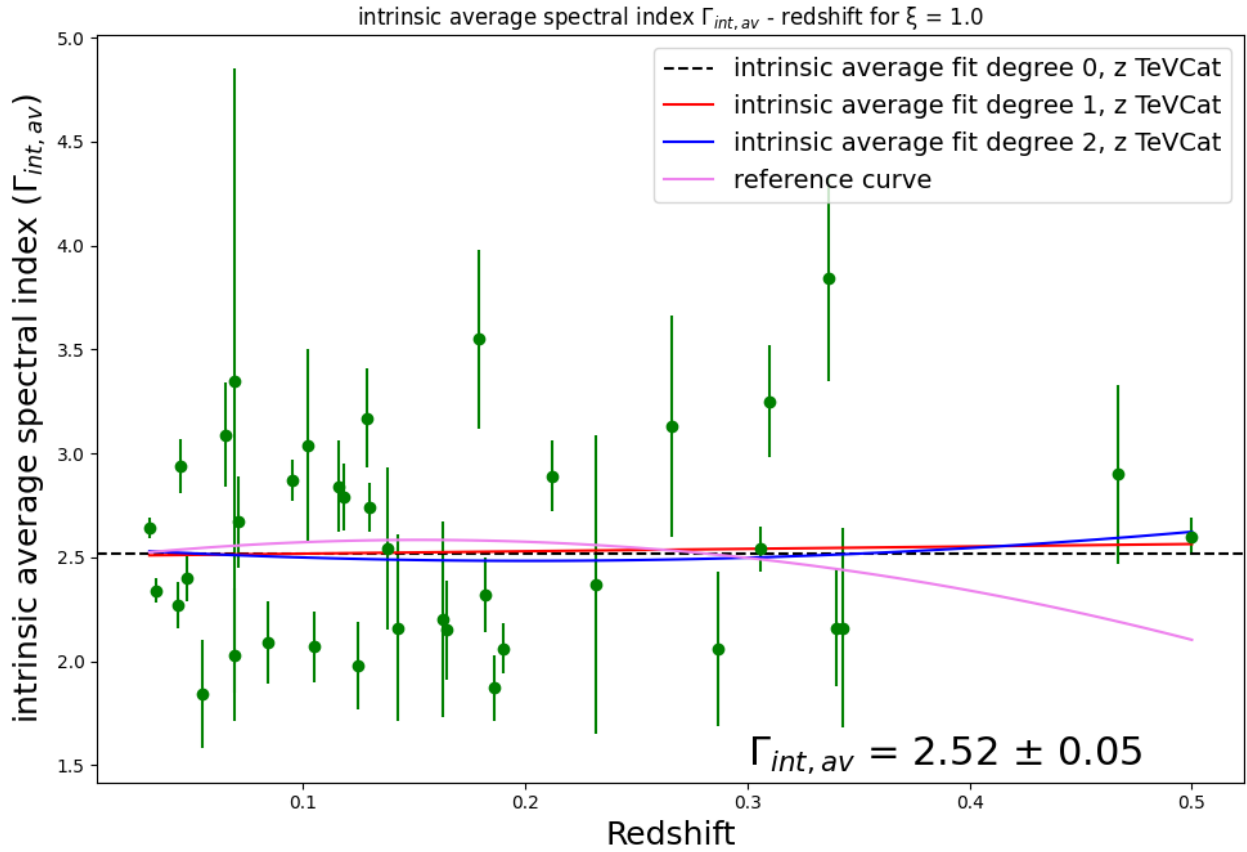
Figure 6.27: Scatter plot for $\xi = 1.0$ between average intrinsic VHE spectral index (method II, $\bar{\Gamma}_{int,all}$) of z TeVCat BL Lacs with redshift. The red and blue solid lines are the best-fit straight line and parabola respectively. The dashed line is the best-fit of degree zero. It is also illustrated the equation of the curve with the best reduced chi-square. In pink the reference curve. The spectral indices of this plot are summarized in Table 8 as Method II.

Table 7:

ξ	$\tilde{\chi}^2_0$	$\tilde{\chi}^2_1$	$\tilde{\chi}^2_2$	$ndof\ (best - fit)$	$|c|\ (best - fit)$
0.1	5.55	4.78	4.86	36 (straight line)	0.68
0.5	5.23	4.78	4.91	36 (straight line)	0.67
1.0	4.37	4.48	4.57	37 (horizontal line)	
2.0	4.24	4.12	4.21	36 (straight line)	0.69
5.0	4.32	4.25	4.28	36 (straight line)	0.68

7 Conclusions

In this thesis I have explored the physical existence of ALPs necessary to explain the evolution of the spectral indices of blazars after correction for EBL attenuation. As easily predictable, the evolution of $\Gamma_{obs}(z)$ (Fig. 6.3-6.4) is apparent: the absorption undergone by the VHE photons from high-z sources is well established. The EBL photons interact mainly with photons of higher energy causing a distortion of the slope of the observed spectrum.

The correction for EBL carried out in this thesis derives from the model by Franceschini and suggests a spectral hardening for high-z sources. This was achieved regardless of the data database used: both by using the entire data set (more than one spectrum per source), and by using only one data set per source and also considering only the sources classified in TeVCat as HBL. However these results, compared to those obtained by the analysis of Galanti et al. (20) analysis, provide a flatter $\Gamma_{em}(z)$. The decreasing trend of $\Gamma_{em}(z)$ was confirmed also taking into account some sources whose redshift is still uncertain. The fluxes emitted in this situation suggest a noticeable difference depending on the redshift: $\Phi_{em}^{CP}(E, z = 0) \propto E^{-2.49}$, $\Phi_{em}^{CP}(E, z = 0.75) \propto E^{-1.16}$ which we cannot physically explain. The various bias effects, suggested to explain this phenomenon, have at present been excluded by several independent studies [(1)]. For this reason it was thought that the correction could be due to particles so far only theorized and never observed: the ALPs. Using the program obtained from Galanti's theoretical model, the spectra have become softer, resulting in a significant change in the evolution of the spectral index with redshift. As the parameter ξ increases, the correction applied at high redshift is always more significant in the modification of the plot $\Gamma_{int} - z$. The fact that only for $\xi = 1.0$ the best fit is horizontal axis can be considered an advantage. This is because it could mean that it is possible to constrain the product of $g_{a\gamma\gamma}$ and B. This reasoning would be based exclusively on the presence of ALPs and that the blazars intrinsic spectra are equal at least up to redshift = 0.5-0.7. That is, such sources do not present a significant evolution of the intrinsic spectrum at VHE. By placing ever more stringent constraints on the coupling constant through other experiments, this method could serve to estimate the value of the extragalactic magnetic field with ever greater precision. Clearly there are still several elements to be taken into consideration such as the magnetic field near the blazar and the Galactic one which, for now, have been set aside because they are considered less influential on gamma photon-ALP conversion. In any case, updates of this type, to apply to the model, could lead to increasingly significant results.

However, there are currently several uncertainties both in the spectra of the individual sources and in the value associated with the extragalactic magnetic field. This is reflected in the rather wide dispersion of the data. In this context, the strong variability of the sources must also be taken into consideration. For this reason this study, although interesting, is to be taken with caution due to the few high redshift statistics and the uncertainties on the individual spectra. It will certainly be very important to replicate it once the CTA project is actually operational. It might also be interesting to apply this study to other gamma-ray sources such as supernovae and gamma-ray bursts which are observed up to very high redshift. The absorption due to the EBL creates a wall that is difficult to overcome by gamma photons, however, considering the hypothesized presence of ALP here, the observation limit would certainly be moved further.

A further important aspect to refine this study is certainly that of accurately defining, source by source, which is the most reliable observed spectrum possible. This will require an in-depth study of the individual observations and also of the possible morphology of the individual sources. For example, it is suspected that the PG 1553 blazar is generated by the presence of two very close supermassive black holes. This hypothesis is due to the fact that the blazar has a rather precise periodicity. As mentioned, these objects usually are aperiodic and therefore unpredictable emissions. For PG 1553, on the other hand, the proximity of the two black holes would generate a precession motion of the light cone emitted by the blazar which would favor its observation. Obviously these characteristics could influence the observed spectrum and make it a source with peculiar characteristics. For this reason, in-depth studies on the single sources are fundamental in the selection of the observed spectral indices from which the correction starts. Furthermore, more knowledge into how, when and why flare phenomena occur are clearly very useful to understand how the spectrum of a single source evolves. Finally, a further challenge in the study of these sources lies in their determination of the redshift, due to the lack of spectral features. For these reasons, the uncertainties to be taken into consideration are considerable and varied, however the results obtained here appear to be encouraging. Furthermore, according to this study, the presence of ALPs seems to be a valid explanation in motivating the hardening of the emitted spectra obtained for high redshift sources.

A few days before the delivery of this thesis, a further study was conducted regarding the redshift of RGB J2243 by Paiano, S.[6]. The best estimate, obtained through a method discussed in detail in (132), gives $z = 0.9$. Applying in this thesis such z to RGB J2243, the following values are obtained: $\Gamma_{em} =$

---

[6] Dipartimento di Fisica e Astronomia, Università di Padova, vicolo dell'Osservatorio 3, I–35122 Padova, Italy; INAF - Osservatorio Astronomico di Padova, vicolo dell'Osservatorio 5, I-35122 Padova, Italy; INFN - Sezione di Padova, via Marzolo 8, Padova, Italy.

$\Gamma_{int,\xi=0.1} = 1.34 \pm 0.61$, $\Gamma_{int,\xi=0.5} = 2.09 \pm 0.33$, $\Gamma_{int,\xi=1.0} = 2.42 \pm 0.35$, $\Gamma_{int,\xi=2.0} = 2.38 \pm 0.41$, $\Gamma_{int,\xi=5.0} = 2.35 \pm 0.44$. Also in this case the emitted spectral index is not consistent with a horizontal trend of $\Gamma_{em}(z)$ given the significant difference compared to low redshift sources ($\Gamma_{em}(z < 0.2) \sim 2.5$). However, compared to the case considered in this thesis ($z = 0.75$) it suggests a very slight increase in the reference curve at high redshifts.

Considering instead $\Gamma_{int,\xi=1.0}$, it is perfectly consistent with the horizontal trend obtained, in this thesis, for $\xi = 1.0$.

Table 1:

Source (spectral type)	z	Detector	$\Delta E_0(z)[TeV]$	Γ_{obs}	K_{obs} $[cm^{-2}s^{-1}TeV^{-1}]$
PG 1553 (HBL)	0.5	VERITAS	0.183-0.500	4.45 ± 0.15	$(5.23 \pm 0.24) \times 10^{-11}$
		HESS	0.245-1.080	4.01 ± 0.35	$(5.68 \pm 0.75) \times 10^{-11}$
		HESS 2005+2006	0.245-1.070	4.44 ± 0.50	$(4.60 \pm 0.61) \times 10^{-11}$
		MAGIC	0.098-0.392	4.06 ± 0.18	$(3.73 \pm 0.50) \times 10^{-11}$
1ES 0033 (HBL)	0.467	MAGIC	0.156-0.390	4.22 ± 0.18	$(8.23 \pm 0.75) \times 10^{-12}$
PKS 0447 (HBL)	0.343	HESS	0.241-1.52	3.85 ± 0.48	$(3.48 \pm 0.93) \times 10^{-11}$
3C 66A (IBL)	0.34	VERITAS	0.228-0.466	4.08 ± 0.28	$(4.12 \pm 0.28) \times 10^{-11}$
		MAGIC	0.078-0.488	3.44 ± 0.16	$(2.04 \pm 0.29) \times 10^{-11}$
TXS 0506 (blazar)	0.3365	VERITAS	0.142-0.226	4.85 ± 0.97	$(2.26 \pm 1.35) \times 10^{-12}$
		MAGIC A	0.079-0.392	3.77 ± 0.08	$(1.87 \pm 0.17) \times 10^{-11}$
		MAGIC B	0.080-0.394	3.49 ± 0.51	$(2.62 \pm 1.45) \times 10^{-11}$
		MAGIC C	0.079-0.389	3.79 ± 0.38	$(6.01 \pm 2.49) \times 10^{-12}$
S5 0716 (IBL)	0.31	MAGIC 2008	0.181-0.676	3.38 ± 0.48	$(1.40 \pm 0.35) \times 10^{-10}$
		MAGIC 2015 fase A	0.148-0.554	4.07 ± 0.07	$(6.77 \pm 0.24) \times 10^{-11}$
		MAGIC 2015 fase B	0.148-0.397	4.60 ± 0.14	$(4.78 \pm 0.36) \times 10^{-11}$
OJ 287 (BL Lac)	0.306	VERITAS	0.119-0.471	3.49 ± 0.13	$(6.88 \pm 0.47) \times 10^{-12}$
1ES 0414+009 (HBL)	0.287	VERITAS	0.232-0.611	3.40 ± 0.44	$(1.67 \pm 0.25) \times 10^{-11}$
		HESS	0.170-1.14	3.41 ± 0.16	$(5.78 \pm 0.41) \times 10^{-12}$
PKS 0301 (HBL)	0.2657	HESS	0.247-0.519	4.42 ± 0.65	$(9.38 \pm 1.57) \times 10^{-12}$
1ES 1011+497 (HBL)	0.212	MAGIC	0.147-0.586	4.13 ± 0.47	$(3.66 \pm 1.04) \times 10^{-11}$
		Ahnen	0.149-0.741	3.28 ± 0.18	$(4.80 \pm 0.41) \times 10^{-11}$
		Aleksic	0.113-0.714	3.68 ± 0.17	$(3.00 \pm 0.32) \times 10^{-11}$
RBS 0413 (HBL)	0.19	VERITAS	0.299-0.855	3.20 ± 0.18	$(1.40 \pm 0.14) \times 10^{-11}$
1ES 1101-232 (HBL)	0.186	HESS	0.259-3.44	2.95 ± 0.18	$(1.96 \pm 0.34) \times 10^{-11}$
1ES 1218+304 (HBL)	0.182	VERITAS	0.189-1.44	3.14 ± 0.22	$(3.63 \pm 0.57) \times 10^{-11}$
		MAGIC	0.087-0.626	3.03 ± 0.21	$(4.65 \pm 0.67) \times 10^{-11}$
RX J0648.7+1516 (HBL)	0.179	VERITAS	0.213-0.475	4.36 ± 0.42	$(2.28 \pm 0.27) \times 10^{-11}$
H 2356-309 (HBL)	0.165	HESS	0.224-0.913	3.02 ± 0.25	$(1.20 \pm 0.14) \times 10^{-11}$
1ES 1440+122 (HBL)	0.163	VERITAS	0.249-0.988	3.10 ± 0.46	$(6.98 \pm 1.73) \times 10^{-12}$
1RXS J101015.9-311909 (HBL)	0.142639	HESS	0.280-2.32	3.03 ± 0.48	$(7.77 \pm 2.83) \times 10^{-12}$
1ES 0806+524 (HBL)	0.138	VERITAS	0.310-0.630	3.63 ± 0.20	$(1.95 \pm 0.17) \times 10^{-11}$
		MAGIC HIGH-STATE	0.174-0.928	2.91 ± 0.18	$(5.55 \pm 0.54) \times 10^{-11}$
		MAGIC LOW-STATE	0.138-1.070	2.77 ± 0.25	$(1.58 \pm 0.24) \times 10^{-11}$
1ES 1215+303 (HBL)	0.13	VERITAS	0.295-0.837	3.70 ± 0.31	$(2.23 \pm 0.37) \times 10^{-11}$
		MAGIC	0.095-1.320	2.97 ± 0.16	$(2.17 \pm 0.28) \times 10^{-11}$
H 1426+428 (HBL)	0.129	CAT	0.250-0.998	3.73 ± 0.20	$(3.47 \pm 0.50) \times 10^{-10}$

		HEGRA 2000	0.774-10.200	2.74 ± 0.36	$(8.01 \pm 6.54) \times 10^{-11}$
		HEGRA 2002	0.778-10.200	2.02 ± 0.13	$(5.61 \pm 1.85) \times 10^{-12}$
		Whipple	0.367-1.700	3.46 ± 0.10	$(2.98 \pm 0.27) \times 10^{-10}$
RGB J0710+591 (HBL)	0.125	VERITAS	0.420-3.650	2.68 ± 0.19	$(2.48 \pm 0.62) \times 10^{-11}$
B3 2247+381 (HBL)	0.1187	MAGIC	0.167-0.846	3.29 ± 0.13	$(1.37 \pm 0.10) \times 10^{-11}$
PKS 2155-304 (HBL)	0.116	HESS	0.221-4.230	3.53 ± 0.08	$(1.20 \pm 0.08) \times 10^{-10}$
		MAGIC	0.316-3.150	3.26 ± 0.12	$(8.76 \pm 1.00) \times 10^{-10}$
1ES 1312-423 (HBL)	0.105	HESS	0.362-4.120	2.67 ± 0.15	$(5.89 \pm 1.26) \times 10^{-12}$
W Comae (IBL)	0.102	VERITAS	0.263-1.150	3.74 ± 0.37	$(6.02 \pm 0.97) \times 10^{-11}$
		VERITAS II	0.190-1.500	3.68 ± 0.19	$(2.00 \pm 0.25) \times 10^{-10}$
SHBL J001355.9-185406 (HBL)	0.095	HESS	0.441-2.100	3.45 ± 0.05	$(7.04 \pm 0.29) \times 10^{-12}$
1ES 1741+196 (HBL)	0.084	VERITAS	0.212-0.422	2.72 ± 0.14	$(9.30 \pm 0.34) \times 10^{-12}$
		MAGIC	0.124-1.970	2.38 ± 0.14	$(4.88 \pm 0.77) \times 10^{-12}$
PKS 2005-489 (HBL)	0.071	HESS	0.342-4.560	3.20 ± 0.17	$(3.45 \pm 0.62) \times 10^{-11}$
		HESS II	0.228-2.280	3.98 ± 0.33	$(2.36 \pm 0.43) \times 10^{-11}$
BL Lacertae (IBL)	0.069	VERITAS	0.222-0.559	3.75 ± 0.50	$(5.63 \pm 0.83) \times 10^{-10}$
		MAGIC	0.155-0.699	3.63 ± 0.16	$(1.88 \pm 0.14) \times 10^{-11}$
PKS 0548-322 (HBL)	0.069	HESS	0.337-3.530	2.42 ± 0.35	$(8.30 \pm 3.66) \times 10^{-12}$
PKS 1440-389 (HBL)	0.065	HESS	0.162-0.923	3.39 ± 0.27	$(2.23 \pm 0.34) \times 10^{-11}$
1ES 1727+502 (HBL)	0.055	VERITAS	0.315-1.260	2.18 ± 0.26	$(3.65 \pm 0.83) \times 10^{-11}$
1ES 1959+650 (HBL)	0.048	MAGIC	0.193-1.530	2.80 ± 0.07	$(9.11 \pm 0.52) \times 10^{-11}$
		MAGIC II	0.194-2.40	2.54 ± 0.11	$(5.69 \pm 0.66) \times 10^{-11}$
Mrk 180 (HBL)	0.045	MAGIC	0.183-1.310	3.18 ± 0.10	$(4.18 \pm 0.34) \times 10^{-11}$
1ES 2344+514 (HBL)	0.044	VERITAS	0.250-6.250	2.46 ± 0.06	$(4.03 \pm 0.30) \times 10^{-11}$
		MAGIC	0.186-4.020	2.99 ± 0.18	$(6.53 \pm 0.88) \times 10^{-11}$
		VERITAS II	0.489-2.340	2.44 ± 0.14	$(3.22 \pm 0.49) \times 10^{-10}$
Mrk 501 (HBL)	0.034	VERITAS	0.251-2.510	2.72 ± 0.21	$(1.58 \pm 0.28) \times 10^{-10}$
		MAGIC	0.213-2.620	2.62 ± 0.14	$(1.95 \pm 0.22) \times 10^{-10}$
			1.460-15.100	2.94 ± 0.05	$(4.92 \pm 0.57) \times 10^{-10}$
Mrk 421 (HBL)	0.031	MAGIC	0.134-2.830	2.87 ± 0.07	$(4.22 \pm 0.36) \times 10^{-10}$
		MAGIC TABELLA	0.134-2.856	2.80 ± 0.08	$(4.55 \pm 0.26) \times 10^{-10}$
			1.360-7.370	3.23 ± 0.12	$(1.85 \pm 0.52) \times 10^{-9}$
RGB J2243 (HBL)	0.5<z<1.1	VERITAS	0.124-0.330	4.62 ± 0.19	$(2.68 \pm 0.34) \times 10^{-11}$
1RXS J023832 (HBL)	0.232	HESS	0.173-0.554	3.49 ± 0.73	$(6.03 \pm 1.62) \times 10^{-12}$
H 1722 (HBL)	0.34±0.15	MAGIC	0.104-0.521	3.48 ± 0.40	$(9.39 \pm 2.55) \times 10^{-12}$
MAGIC J2001 (IBL)	0.17<z<0.18	MAGIC	0.099-0.393	2.77 ± 0.44	$(6.23 \pm 0.21) \times 10^{-11}$
VER J0521 (IBL)	Z=0.108 or z>0.18	VERITAS	0.224-1.120	3.49 ± 0.14	$(5.42 \pm 0.43) \times 10^{-11}$

Table 2:

Source (spectral type)	z	Γ_{obs}	Γ_{em}^{CP}	K_{em}^{CP} $[cm^{-2}s^{-1}TeV^{-1}]$
PG 1553 (HBL)	0.5	4.45 ± 0.15	1.95 ± 0.06	$(3.32 \pm 0.05) \times 10^{-10}$
		4.01 ± 0.35	0.64 ± 0.43	$(3.45 \pm 0.51) \times 10^{-10}$
		4.44 ± 0.50	1.23 ± 0.44	$(2.91 \pm 0.31) \times 10^{-10}$
		4.06 ± 0.18	2.60 ± 0.17	$(1.88 \pm 0.23) \times 10^{-10}$
1ES 0033 (HBL)	0.467	4.22 ± 0.18	2.54 ± 0.58	$(3.77 \pm 1.06) \times 10^{-11}$
PKS 0447 (HBL)	0.343	3.85 ± 0.48	1.48 ± 0.47	$(9.38 \pm 2.42) \times 10^{-11}$
3C 66A (IBL)	0.34	4.08 ± 0.28	2.25 ± 0.17	$(1.20 \pm 0.05) \times 10^{-10}$
		3.44 ± 0.16	2.63 ± 0.58	$(5.14 \pm 2.56) \times 10^{-11}$
TXS 0506 (blazar)	0.3365	4.85 ± 0.97	4.10 ± 1.11	$(4.82 \pm 3.29) \times 10^{-12}$
		3.77 ± 0.08	3.29 ± 0.44	$(3.65 \pm 1.74) \times 10^{-11}$
		3.49 ± 0.51	2.67 ± 0.21	$(7.64 \pm 1.60) \times 10^{-11}$
		3.79 ± 0.38	3.10 ± 0.07	$(1.50 \pm 0.11) \times 10^{-11}$
S5 0716 (IBL)	0.31	3.38 ± 0.48	1.68 ± 0.21	$(4.16 \pm 0.40) \times 10^{-10}$
		4.07 ± 0.07	2.90 ± 0.25	$(1.71 \pm 0.20) \times 10^{-10}$
		4.60 ± 0.14	3.61 ± 0.24	$(1.14 \pm 0.15) \times 10^{-10}$
OJ 287 (BL Lac)	0.306	3.49 ± 0.13	2.39 ± 0.14	$(1.74 \pm 0.11) \times 10^{-11}$
1ES 0414+009 (HBL)	0.287	3.40 ± 0.44	1.77 ± 0.36	$(3.99 \pm 0.45) \times 10^{-11}$
		3.41 ± 0.16	1.93 ± 0.28	$(1.43 \pm 0.15) \times 10^{-11}$
PKS 0301 (HBL)	0.2657	4.42 ± 0.65	2.94 ± 0.50	$(2.01 \pm 0.25) \times 10^{-11}$
1ES 1011+497 (HBL)	0.212	4.13 ± 0.47	3.58 ± 0.61	$(6.01 \pm 2.21) \times 10^{-11}$
		3.28 ± 0.18	2.19 ± 0.13	$(8.97 \pm 0.47) \times 10^{-11}$
		3.68 ± 0.17	2.87 ± 0.16	$(5.79 \pm 0.51) \times 10^{-11}$
RBS 0413 (HBL)	0.19	3.20 ± 0.18	1.96 ± 0.12	$(2.14 \pm 0.13) \times 10^{-11}$
1ES 1101-232 (HBL)	0.186	2.95 ± 0.18	1.76 ± 0.15	$(3.07 \pm 0.46) \times 10^{-11}$
1ES 1218+304 (HBL)	0.182	3.14 ± 0.22	1.92 ± 0.23	$(5.34 \pm 0.88) \times 10^{-11}$
		3.03 ± 0.21	2.45 ± 0.27	$(7.93 \pm 1.34) \times 10^{-11}$
RX J0648.7+1516 (HBL)	0.179	4.36 ± 0.42	3.49 ± 0.43	$(3.64 \pm 0.42) \times 10^{-11}$
H 2356-309 (HBL)	0.165	3.02 ± 0.25	2.09 ± 0.24	$(1.84 \pm 0.19) \times 10^{-11}$
1ES 1440+122 (HBL)	0.163	3.10 ± 0.46	2.15 ± 0.48	$(1.05 \pm 0.26) \times 10^{-11}$
1RXS J101015.9-311909 (HBL)	0.142639	3.03 ± 0.48	2.11 ± 0.46	$(1.05 \pm 0.38) \times 10^{-11}$
1ES 0806+524 (HBL)	0.138	3.63 ± 0.20	2.78 ± 0.15	$(2.57 \pm 0.17) \times 10^{-11}$
		2.91 ± 0.18	2.19 ± 0.16	$(8.22 \pm 0.65) \times 10^{-11}$
		2.77 ± 0.25	2.17 ± 0.40	$(2.30 \pm 0.49) \times 10^{-11}$
1ES 1215+303 (HBL)	0.13	3.70 ± 0.31	2.88 ± 0.28	$(2.90 \pm 0.42) \times 10^{-11}$
		2.97 ± 0.16	2.52 ± 0.16	$(3.37 \pm 0.39) \times 10^{-11}$
H 1426+428 (HBL)	0.129	3.73 ± 0.20	2.88 ± 0.17	$(4.42 \pm 0.53) \times 10^{-10}$
		2.74 ± 0.36	1.57 ± 0.46	$(4.98 \pm 5.21) \times 10^{-11}$
		2.02 ± 0.13	0.92 ± 0.17	$(3.53 \pm 1.49) \times 10^{-12}$
		3.46 ± 0.10	2.63 ± 0.13	$(3.80 \pm 0.45) \times 10^{-10}$
RGB J0710+591 (HBL)	0.125	2.68 ± 0.19	1.94 ± 0.21	$(3.26 \pm 0.93) \times 10^{-11}$
B3 2247+381 (HBL)	0.1187	3.29 ± 0.13	2.77 ± 0.16	$(1.96 \pm 0.18) \times 10^{-11}$
PKS 2155-304 (HBL)	0.116	3.53 ± 0.08	2.82 ± 0.07	$(1.57 \pm 0.09) \times 10^{-10}$
		3.26 ± 0.12	2.57 ± 0.13	$(1.12 \pm 0.13) \times 10^{-9}$
1ES 1312-423 (HBL)	0.105	2.67 ± 0.15	2.05 ± 0.17	$(7.40 \pm 1.78) \times 10^{-12}$
W Comae (IBL)	0.102	3.74 ± 0.37	3.15 ± 0.34	$(7.59 \pm 1.12) \times 10^{-11}$
		3.68 ± 0.19	3.11 ± 0.18	$(2.57 \pm 0.30) \times 10^{-10}$

SHBL J001355.9-185406 (HBL)	0.095	3.45 ± 0.05	2.85 ± 0.10	$(8.21 \pm 0.66) \times 10^{-12}$
1ES 1741+196 (HBL)	0.084	2.72 ± 0.14	2.37 ± 0.19	$(1.12 \pm 0.06) \times 10^{-11}$
		2.38 ± 0.14	1.91 ± 0.20	$(6.03 \pm 1.40) \times 10^{-12}$
PKS 2005-489 (HBL)	0.071	3.20 ± 0.17	2.75 ± 0.16	$(3.86 \pm 0.63) \times 10^{-11}$
		3.98 ± 0.33	3.60 ± 0.33	$(2.77 \pm 0.50) \times 10^{-11}$
BL Lacertae (IBL)	0.069	3.75 ± 0.50	3.44 ± 0.49	$(6.57 \pm 0.95) \times 10^{-10}$
		3.63 ± 0.16	3.36 ± 0.19	$(2.22 \pm 0.20) \times 10^{-11}$
PKS 0548-322 (HBL)	0.069	2.42 ± 0.35	2.02 ± 0.32	$(9.55 \pm 3.97) \times 10^{-12}$
PKS 1440-389 (HBL)	0.065	3.39 ± 0.27	3.08 ± 0.25	$(2.68 \pm 0.37) \times 10^{-11}$
1ES 1727+502 (HBL)	0.055	2.18 ± 0.26	1.83 ± 0.26	$(3.97 \pm 0.92) \times 10^{-11}$
1ES 1959+650 (HBL)	0.048	2.80 ± 0.07	2.53 ± 0.06	$(1.01 \pm 0.51) \times 10^{-10}$
		2.54 ± 0.11	2.26 ± 0.12	$(6.22 \pm 0.79) \times 10^{-11}$
Mrk 180 (HBL)	0.045	3.18 ± 0.10	2.94 ± 0.14	$(4.63 \pm 0.48) \times 10^{-11}$
1ES 2344+514 (HBL)	0.044	2.46 ± 0.06	2.20 ± 0.06	$(4.32 \pm 0.31) \times 10^{-11}$
		2.99 ± 0.18	2.76 ± 0.16	$(7.30 \pm 0.90) \times 10^{-11}$
		2.44 ± 0.14	2.17 ± 0.13	$(3.42 \pm 0.49) \times 10^{-10}$
Mrk 501 (HBL)	0.034	2.72 ± 0.21	2.53 ± 0.20	$(1.70 \pm 0.29) \times 10^{-10}$
		2.62 ± 0.14	2.43 ± 0.16	$(2.08 \pm 0.28) \times 10^{-10}$
		2.94 ± 0.05	2.60 ± 0.10	$(3.89 \pm 0.93) \times 10^{-10}$
Mrk 421 (HBL)	0.031	2.87 ± 0.07	2.72 ± 0.07	$(4.67 \pm 0.37) \times 10^{-10}$
		2.80 ± 0.08	2.65 ± 0.07	$(4.92 \pm 0.26) \times 10^{-10}$
		3.23 ± 0.12	3.02 ± 0.10	$(1.85 \pm 0.41) \times 10^{-9}$
RGB J2243 (HBL)	0.5	4.62 ± 0.19	3.07 ± 0.40	$(1.27 \pm 0.32) \times 10^{-10}$
	0.75	4.62 ± 0.19	1.98 ± 0.54	$(4.47 \pm 1.54) \times 10^{-10}$
	1.1	4.62 ± 0.19	0.55 ± 0.69	$(2.85 \pm 1.26) \times 10^{-9}$
1RXS J023832 (HBL)	0.232	3.49 ± 0.73	2.23 ± 0.72	$(1.20 \pm 0.30) \times 10^{-11}$
H 1722 (HBL)	0.19	3.48 ± 0.40	3.05 ± 0.43	$(1.44 \pm 0.41) \times 10^{-11}$
	0.34	3.48 ± 0.40	2.62 ± 0.46	$(2.29 \pm 0.69) \times 10^{-11}$
	0.49	3.48 ± 0.40	2.11 ± 0.49	$(4.15 \pm 1.32) \times 10^{-11}$
MAGIC J2001 (IBL)	0.17	2.77 ± 0.44	2.33 ± 0.37	$(9.93 \pm 2.66) \times 10^{-11}$
	0.18	2.77 ± 0.44	2.30 ± 0.37	$(1.03 \pm 0.27) \times 10^{-10}$
VER J0521 (IBL)	0.108	3.49 ± 0.14	2.87 ± 0.13	$(6.96 \pm 0.49) \times 10^{-11}$
	0.18	3.49 ± 0.14	2.41 ± 0.13	$(8.62 \pm 0.57) \times 10^{-11}$

Table 3:

Source (spectral type)	Γ_{em}	$\Gamma_{\xi=0.1}$	$\Gamma_{\xi=0.5}$	$\Gamma_{\xi=1.0}$	$\Gamma_{\xi=2.0}$	$\Gamma_{\xi=5.0}$
PG 1553 (HBL)	1.95 ± 0.06	1.95 ± 0.06	2.13 ± 0.05	2.65 ± 0.08	2.80 ± 0.07	2.77 ± 0.06
	0.64 ± 0.43	0.64 ± 0.43	1.14 ± 0.30	1.88 ± 0.30	1.87 ± 0.36	1.80 ± 0.40
	1.23 ± 0.44	1.23 ± 0.44	1.64 ± 0.43	2.33 ± 0.45	2.37 ± 0.46	2.31 ± 0.46
	2.60 ± 0.17	2.60 ± 0.17	2.67 ± 0.16	2.93 ± 0.13	3.05 ± 0.14	3.07 ± 0.14
1ES 0033 (HBL)	2.54 ± 0.58	2.54 ± 0.58	2.62 ± 0.55	2.90 ± 0.43	3.05 ± 0.43	3.07 ± 0.44
PKS 0447 (HBL)	1.48 ± 0.47	1.49 ± 0.47	1.64 ± 0.47	2.16 ± 0.48	2.35 ± 0.48	2.29 ± 0.47
3C 66A (IBL)	2.25 ± 0.17	2.26 ± 0.17	2.30 ± 0.18	2.57 ± 0.21	2.83 ± 0.21	2.87 ± 0.21
	2.63 ± 0.58	2.63 ± 0.58	2.64 ± 0.56	2.71 ± 0.48	2.81 ± 0.42	2.83 ± 0.41
TXS 0506 (blazar)	4.10 ± 1.11	4.10 ± 1.11	4.11 ± 1.11	4.19 ± 1.09	4.32 ± 1.07	4.35 ± 1.06
	3.29 ± 0.44	3.29 ± 0.44	3.29 ± 0.43	3.33 ± 0.38	3.29 ± 0.34	3.41 ± 0.33
	2.67 ± 0.21	2.68 ± 0.21	2.69 ± 0.22	2.79 ± 0.27	2.90 ± 0.31	2.92 ± 0.32
	3.10 ± 0.07	3.10 ± 0.07	3.11 ± 0.08	3.18 ± 0.12	3.28 ± 0.17	3.30 ± 0.18

S5 0716 (IBL)	1.68 ± 0.21	1.69 ± 0.21	1.73 ± 0.23	1.99 ± 0.29	2.22 ± 0.32	2.25 ± 0.31
	2.90 ± 0.25	2.91 ± 0.25	2.93 ± 0.24	3.06 ± 0.21	3.23 ± 0.18	3.28 ± 0.18
	3.61 ± 0.24	3.61 ± 0.24	3.63 ± 0.24	3.74 ± 0.22	3.89 ± 0.20	3.92 ± 0.19
OJ 287 (BL Lac)	2.39 ± 0.14	2.39 ± 0.14	2.41 ± 0.14	2.54 ± 0.11	2.71 ± 0.09	2.75 ± 0.10
1ES 0414+009 (HBL)	1.77 ± 0.36	1.78 ± 0.36	1.81 ± 0.36	2.02 ± 0.37	2.27 ± 0.39	2.31 ± 0.39
	1.93 ± 0.28	1.94 ± 0.28	1.96 ± 0.27	2.14 ± 0.23	2.37 ± 0.22	2.42 ± 0.23
PKS 0301 (HBL)	2.94 ± 0.50	2.95 ± 0.51	2.97 ± 0.51	3.13 ± 0.53	3.38 ± 0.57	3.44 ± 0.55
1ES 1011+497 (HBL)	3.58 ± 0.61	3.58 ± 0.61	3.59 ± 0.61	3.60 ± 0.59	3.72 ± 0.57	3.75 ± 0.56
	2.19 ± 0.13	2.19 ± 0.13	2.20 ± 0.13	2.29 ± 0.13	2.49 ± 0.14	2.55 ± 0.14
	2.87 ± 0.16	2.87 ± 0.16	2.88 ± 0.16	2.93 ± 0.16	3.07 ± 0.15	3.13 ± 0.15
RBS 0413 (HBL)	1.96 ± 0.12	1.96 ± 0.12	1.97 ± 0.12	2.06 ± 0.12	2.28 ± 0.14	2.36 ± 0.14
1ES 1101-232 (HBL)	1.76 ± 0.15	1.77 ± 0.16	1.78 ± 0.15	1.87 ± 0.16	2.10 ± 0.16	2.16 ± 0.16
1ES 1218+304 (HBL)	1.92 ± 0.23	1.93 ± 0.23	1.94 ± 0.23	2.02 ± 0.23	2.25 ± 0.23	2.33 ± 0.23
	2.45 ± 0.27	2.45 ± 0.27	2.46 ± 0.27	2.48 ± 0.26	2.58 ± 0.25	2.63 ± 0.24
RX J0648.7+1516 (HBL)	3.49 ± 0.43	3.49 ± 0.43	3.50 ± 0.43	3.55 ± 0.43	3.69 ± 0.43	3.77 ± 0.43
H 2356-309 (HBL)	2.09 ± 0.24	2.10 ± 0.24	2.10 ± 0.24	2.15 ± 0.24	2.31 ± 0.24	2.39 ± 0.24
1ES 1440+122 (HBL)	2.15 ± 0.48	2.15 ± 0.48	2.16 ± 0.48	2.20 ± 0.47	2.37 ± 0.47	2.46 ± 0.47
1RXS J101015.9-311909 (HBL)	2.11 ± 0.46	2.12 ± 0.46	2.12 ± 0.46	2.16 ± 0.45	2.31 ± 0.45	2.41 ± 0.46
1ES 0806+524 (HBL)	2.78 ± 0.15	2.78 ± 0.15	2.79 ± 0.15	2.81 ± 0.16	2.95 ± 0.16	3.05 ± 0.17
	2.19 ± 0.16	2.20 ± 0.16	2.20 ± 0.16	2.22 ± 0.16	2.34 ± 0.16	2.42 ± 0.16
	2.17 ± 0.40	2.17 ± 0.40	2.18 ± 0.40	2.19 ± 0.39	2.29 ± 0.36	2.36 ± 0.35
1ES 1215+303 (HBL)	2.88 ± 0.28	2.89 ± 0.28	2.89 ± 0.28	2.92 ± 0.29	3.04 ± 0.29	3.15 ± 0.29
	2.52 ± 0.16	2.52 ± 0.16	2.52 ± 0.16	2.53 ± 0.15	2.60 ± 0.15	2.66 ± 0.15
H 1426+428 (HBL)	2.88 ± 0.17	2.89 ± 0.17	2.89 ± 0.17	2.91 ± 0.17	3.05 ± 0.18	3.16 ± 0.18
	1.57 ± 0.46	1.58 ± 0.46	1.59 ± 0.45	1.63 ± 0.45	1.74 ± 0.44	1.91 ± 0.39
	0.92 ± 0.17	0.92 ± 0.17	0.93 ± 0.16	0.98 ± 0.16	1.11 ± 0.15	1.25 ± 0.08
	2.63 ± 0.13	2.63 ± 0.13	2.64 ± 0.13	2.66 ± 0.13	2.80 ± 0.13	2.90 ± 0.12
RGB J0710+591 (HBL)	1.94 ± 0.21	1.95 ± 0.21	1.95 ± 0.21	1.98 ± 0.21	2.10 ± 0.21	2.19 ± 0.20
B3 2247+381 (HBL)	2.77 ± 0.16	2.78 ± 0.16	2.78 ± 0.16	2.79 ± 0.16	2.87 ± 0.16	2.94 ± 0.14
PKS 2155-304 (HBL)	2.82 ± 0.07	2.83 ± 0.07	2.83 ± 0.07	2.85 ± 0.07	2.95 ± 0.07	3.04 ± 0.07
	2.57 ± 0.13	2.57 ± 0.13	2.57 ± 0.13	2.59 ± 0.13	2.70 ± 0.13	2.79 ± 0.12
1ES 1312-423 (HBL)	2.05 ± 0.17	2.05 ± 0.17	2.06 ± 0.17	2.07 ± 0.17	2.15 ± 0.17	2.25 ± 0.17
W Comae (IBL)	3.15 ± 0.34	3.17 ± 0.34	3.17 ± 0.34	3.18 ± 0.34	3.25 ± 0.35	3.34 ± 0.35
	3.11 ± 0.18	3.12 ± 0.18	3.12 ± 0.18	3.13 ± 0.19	3.20 ± 0.18	3.29 ± 0.19
SHBL J001355.9-185406 (HBL)	2.85 ± 0.10	2.85 ± 0.10	2.85 ± 0.10	2.87 ± 0.10	2.94 ± 0.09	3.04 ± 0.08
1ES 1741+196 (HBL)	2.37 ± 0.19	2.37 ± 0.19	2.38 ± 0.19	2.38 ± 0.19	2.40 ± 0.19	2.47 ± 0.18
	1.91 ± 0.20	1.92 ± 0.20	1.92 ± 0.20	1.93 ± 0.20	1.97 ± 0.19	2.06 ± 0.18
PKS 2005-489 (HBL)	2.75 ± 0.16	2.76 ± 0.16	2.76 ± 0.16	2.77 ± 0.16	2.81 ± 0.16	2.89 ± 0.16
	3.60 ± 0.33	3.61 ± 0.33	3.61 ± 0.33	3.61 ± 0.33	3.64 ± 0.33	3.71 ± 0.33
BL Lacertae (IBL)	3.44 ± 0.49	3.44 ± 0.49	3.44 ± 0.49	3.44 ± 0.49	3.47 ± 0.49	3.53 ± 0.50
	3.36 ± 0.19	3.37 ± 0.19	3.37 ± 0.19	3.37 ± 0.19	3.39 ± 0.19	3.44 ± 0.19

PKS 0548-322 (HBL)	2.02 ± 0.32	2.02 ± 0.32	2.02 ± 0.32	2.03 ± 0.32	2.06 ± 0.32	2.14 ± 0.33
PKS 1440-389 (HBL)	3.08 ± 0.25	3.08 ± 0.25	3.08 ± 0.25	3.09 ± 0.25	3.11 ± 0.25	3.17 ± 0.26
1ES 1727+502 (HBL)	1.83 ± 0.26	1.83 ± 0.26	1.83 ± 0.26	1.84 ± 0.26	1.86 ± 0.26	1.93 ± 0.26
1ES 1959+650 (HBL)	2.53 ± 0.06	2.53 ± 0.06	2.53 ± 0.06	2.53 ± 0.06	2.55 ± 0.06	2.60 ± 0.06
	2.26 ± 0.12	2.26 ± 0.12	2.26 ± 0.12	2.27 ± 0.12	2.28 ± 0.12	2.34 ± 0.12
Mrk 180 (HBL)	2.94 ± 0.14	2.94 ± 0.14	2.94 ± 0.13	2.94 ± 0.13	2.96 ± 0.13	3.00 ± 0.13
1ES 2344+514 (HBL)	2.20 ± 0.06	2.20 ± 0.06	2.20 ± 0.06	2.21 ± 0.06	2.22 ± 0.06	2.26 ± 0.06
	2.76 ± 0.16	2.76 ± 0.16	2.76 ± 0.16	2.76 ± 0.16	2.77 ± 0.16	2.82 ± 0.17
	2.17 ± 0.13	2.17 ± 0.13	2.17 ± 0.13	2.17 ± 0.13	2.19 ± 0.13	2.24 ± 0.13
Mrk 501 (HBL)	2.53 ± 0.20	2.53 ± 0.20	2.53 ± 0.20	2.53 ± 0.20	2.54 ± 0.20	2.58 ± 0.21
	2.43 ± 0.16	2.43 ± 0.16	2.43 ± 0.16	2.43 ± 0.16	2.44 ± 0.16	2.45 ± 0.16
	2.60 ± 0.10	2.60 ± 0.10	2.61 ± 0.10	2.62 ± 0.10	2.66 ± 0.08	2.65 ± 0.08
Mrk 421 (HBL)	2.72 ± 0.07	2.72 ± 0.07	2.72 ± 0.07	2.72 ± 0.07	2.73 ± 0.07	2.76 ± 0.07
	2.65 ± 0.07	2.65 ± 0.07	2.65 ± 0.07	2.65 ± 0.07	2.66 ± 0.07	2.68 ± 0.07
	3.02 ± 0.10	3.02 ± 0.10	3.03 ± 0.10	3.04 ± 0.10	3.06 ± 0.10	3.06 ± 0.10
RGB J2243 (HBL)	3.07 ± 0.40	3.07 ± 0.40	3.13 ± 0.37	3.42 ± 0.31	3.55 ± 0.31	3.56 ± 0.31
	1.98 ± 0.54	1.98 ± 0.54	2.35 ± 0.39	2.78 ± 0.35	2.83 ± 0.38	2.80 ± 0.40
	0.55 ± 0.69	0.56 ± 0.68	1.93 ± 0.26	1.99 ± 0.38	1.86 ± 0.46	1.80 ± 0.48
1RXS J023832 (HBL)	2.23 ± 0.72	2.24 ± 0.72	2.25 ± 0.72	2.37 ± 0.72	2.59 ± 0.73	2.64 ± 0.72
H 1722 (HBL)	3.05 ± 0.43	3.05 ± 0.43	3.05 ± 0.43	3.07 ± 0.43	3.14 ± 0.42	3.18 ± 0.42
	2.62 ± 0.46	2.63 ± 0.46	2.64 ± 0.46	2.73 ± 0.44	2.85 ± 0.43	2.87 ± 0.43
	2.11 ± 0.49	2.11 ± 0.49	2.16 ± 0.47	2.37 ± 0.42	2.49 ± 0.44	2.52 ± 0.45
MAGIC J2001 (IBL)	2.33 ± 0.37	2.33 ± 0.37	2.33 ± 0.37	2.36 ± 0.37	2.43 ± 0.39	2.47 ± 0.39
	2.30 ± 0.37	2.30 ± 0.37	2.30 ± 0.37	2.33 ± 0.37	2.41 ± 0.38	2.45 ± 0.39
VER J0521 (IBL)	2.87 ± 0.13	2.87 ± 0.13	2.88 ± 0.13	2.89 ± 0.13	2.97 ± 0.13	3.06 ± 0.13
	2.41 ± 0.13	2.41 ± 0.13	2.42 ± 0.13	2.48 ± 0.13	2.68 ± 0.13	2.76 ± 0.13

Table 8:

Source[7] (spectral type)	$\bar{\Gamma}_{em}$	$\bar{\Gamma}_{\xi=0.1}$	$\bar{\Gamma}_{\xi=0.5}$	$\bar{\Gamma}_{\xi=1.0}$	$\bar{\Gamma}_{\xi=2.0}$	$\bar{\Gamma}_{\xi=5.0}$
PG 1553 (HBL) Method I	1.99 ± 0.06	1.99 ± 0.06	2.15 ± 0.05	2.68 ± 0.07	2.81 ± 0.06	2.79 ± 0.05
Method II	1.90 ± 0.10	1.90 ± 0.10	2.09 ± 0.09	2.60 ± 0.09	2.72 ± 0.09	2.72 ± 0.09
1ES 0033 (HBL)	2.54 ± 0.58	2.54 ± 0.58	2.62 ± 0.55	2.90 ± 0.43	3.05 ± 0.43	3.07 ± 0.44
PKS 0447 (HBL)	1.48 ± 0.47	1.49 ± 0.47	1.64 ± 0.47	2.16 ± 0.48	2.35 ± 0.48	2.29 ± 0.47
3C 66A (IBL) Method I	2.28 ± 0.16	2.29 ± 0.16	2.33 ± 0.17	2.59 ± 0.19	2.83 ± 0.19	2.86 ± 0.19
Method II	1.91 ± 0.29	1.92 ± 0.29	1.95 ± 0.29	2.16 ± 0.28	2.34 ± 0.27	2.37 ± 0.27
TXS 0506 (blazar) Method I	3.07 ± 0.06	3.07 ± 0.06	3.07 ± 0.07	3.14 ± 0.10	3.22 ± 0.13	3.26 ± 0.14
Method II	3.79 ± 0.49	3.79 ± 0.49	3.80 ± 0.49	3.84 ± 0.49	3.90 ± 0.48	3.92 ± 0.48
S5 0716 (IBL) Method I	2.63 ± 0.13	2.63 ± 0.13	2.73 ± 0.14	3.08 ± 0.13	3.33 ± 0.12	3.38 ± 0.12
Method II	3.10 ± 0.27	3.10 ± 0.27	3.12 ± 0.27	3.25 ± 0.26	3.40 ± 0.25	3.44 ± 0.25
OJ 287 (BL Lac)	2.39 ± 0.14	2.39 ± 0.14	2.41 ± 0.14	2.54 ± 0.11	2.71 ± 0.09	2.75 ± 0.10
1ES 0414+009 (HBL) Method I	1.87 ± 0.22	1.88 ± 0.22	1.91 ± 0.22	2.11 ± 0.19	2.35 ± 0.19	2.39 ± 0.20
Method II	1.83 ± 0.40	1.84 ± 0.40	1.87 ± 0.40	2.06 ± 0.37	2.29 ± 0.37	2.33 ± 0.37
PKS 0301 (HBL)	2.94 ± 0.50	2.95 ± 0.51	2.97 ± 0.51	3.13 ± 0.53	3.38 ± 0.57	3.44 ± 0.55
1ES 1011+497 (HBL) Method I	2.49 ± 0.10	2.49 ± 0.10	2.50 ± 0.10	2.57 ± 0.10	2.79 ± 0.10	2.85 ± 0.10
Method II	2.83 ± 0.17	2.83 ± 0.17	2.84 ± 0.17	2.89 ± 0.17	3.03 ± 0.16	3.09 ± 0.16
RBS 0413 (HBL)	1.96 ± 0.12	1.96 ± 0.12	1.97 ± 0.12	2.06 ± 0.12	2.28 ± 0.14	2.36 ± 0.14
1ES 1101-232 (HBL)	1.76 ± 0.15	1.77 ± 0.16	1.78 ± 0.15	1.87 ± 0.16	2.10 ± 0.16	2.16 ± 0.16
1ES 1218+304 (HBL) Method I	2.14 ± 0.17	2.25 ± 0.19	2.25 ± 0.19	2.25 ± 0.19	2.25 ± 0.19	2.25 ± 0.19
Method II	2.25 ± 0.19	2.26 ± 0.19	2.26 ± 0.19	2.32 ± 0.18	2.51 ± 0.16	2.59 ± 0.16
RX J0648.7+1516 (HBL)	3.49 ± 0.43	3.49 ± 0.43	3.50 ± 0.43	3.55 ± 0.43	3.69 ± 0.43	3.77 ± 0.43
H 2356-309 (HBL)	2.09 ± 0.24	2.10 ± 0.24	2.10 ± 0.24	2.15 ± 0.24	2.31 ± 0.24	2.39 ± 0.24
1ES 1440+122 (HBL)	2.15 ± 0.48	2.15 ± 0.48	2.16 ± 0.48	2.20 ± 0.47	2.37 ± 0.47	2.46 ± 0.47
1RXS J101015.9-311909 (HBL)	2.11 ± 0.46	2.12 ± 0.46	2.12 ± 0.46	2.16 ± 0.45	2.31 ± 0.45	2.41 ± 0.46
1ES 0806+524 (HBL) Method I	2.48 ± 0.10	2.48 ± 0.10	2.49 ± 0.10	2.49 ± 0.11	2.61 ± 0.11	2.68 ± 0.11
Method II	2.52 ± 0.39	2.53 ± 0.39	2.53 ± 0.39	2.54 ± 0.39	2.63 ± 0.38	2.70 ± 0.38
1ES 1215+303 (HBL) Method I	2.61 ± 0.14	2.61 ± 0.14	2.61 ± 0.14	2.61 ± 0.13	2.69 ± 0.13	2.76 ± 0.13
Method II	2.72 ± 0.12	2.72 ± 0.12	2.73 ± 0.12	2.74 ± 0.12	2.82 ± 0.12	2.88 ± 0.13
H 1426+428 (HBL) Method I	2.21 ± 0.09	2.22 ± 0.09	2.18 ± 0.08	2.21 ± 0.08	2.28 ± 0.08	1.93 ± 0.06
Method II	3.14 ± 0.24	3.15 ± 0.24	3.15 ± 0.24	3.17 ± 0.24	3.31 ± 0.24	3.40 ± 0.24
RGB J0710+591 (HBL)	1.94 ± 0.21	1.95 ± 0.21	1.95 ± 0.21	1.98 ± 0.21	2.10 ± 0.21	2.19 ± 0.20

---

[7] Method I is the one derived from eq. 6.10 and 6.11. The method II is the one indicated with $\bar{\Gamma}_{em,all}$ and $\bar{\Gamma}_{int,all}$ in the text.

B3 2247+381 (HBL)	2.77 ± 0.16	2.78 ± 0.16	2.78 ± 0.16	2.79 ± 0.16	2.87 ± 0.16	2.94 ± 0.14
PKS 2155-304 (HBL)	2.76 ± 0.06	2.77 ± 0.06	2.77 ± 0.06	2.79 ± 0.06	2.89 ± 0.06	2.98 ± 0.06
	2.82 ± 0.22	2.82 ± 0.22	2.83 ± 0.22	2.84 ± 0.22	2.95 ± 0.22	3.04 ± 0.22
1ES 1312-423 (HBL)	2.05 ± 0.17	2.05 ± 0.17	2.06 ± 0.17	2.07 ± 0.17	2.15 ± 0.17	2.25 ± 0.17
W Comae (IBL)	3.12 ± 0.16	3.13 ± 0.16	3.13 ± 0.16	3.14 ± 0.17	3.21 ± 0.16	3.30 ± 0.17
	3.02 ± 0.46	3.03 ± 0.46	3.03 ± 0.46	3.04 ± 0.46	3.11 ± 0.46	3.21 ± 0.46
SHBL J001355.9-185406 (HBL)	2.85 ± 0.10	2.85 ± 0.10	2.85 ± 0.10	2.87 ± 0.10	2.94 ± 0.09	3.04 ± 0.08
1ES 1741+196 (HBL) Method I	2.15 ± 0.14	2.16 ± 0.14	2.16 ± 0.14	2.17 ± 0.14	2.19 ± 0.13	2.27 ± 0.13
Method II	2.08 ± 0.20	2.09 ± 0.20	2.09 ± 0.20	2.09 ± 0.20	2.14 ± 0.20	2.22 ± 0.20
PKS 2005-489 (HBL) Method I	2.91 ± 0.14	2.92 ± 0.14	2.92 ± 0.14	2.93 ± 0.14	2.97 ± 0.14	3.05 ± 0.14
Method II	2.65 ± 0.22	2.67 ± 0.22	2.67 ± 0.22	2.67 ± 0.22	2.71 ± 0.22	2.79 ± 0.23
BL Lacertae (IBL) Method I	3.37 ± 0.18	3.38 ± 0.18	3.38 ± 0.18	3.38 ± 0.18	3.40 ± 0.18	3.45 ± 0.18
Method II	3.34 ± 1.50	3.35 ± 1.50	3.35 ± 1.49	3.35 ± 1.50	3.37 ± 1.49	3.42 ± 1.48
PKS 0548-322 (HBL)	2.02 ± 0.32	2.02 ± 0.32	2.02 ± 0.32	2.03 ± 0.32	2.06 ± 0.32	2.14 ± 0.33
PKS 1440-389 (HBL)	3.08 ± 0.25	3.08 ± 0.25	3.08 ± 0.25	3.09 ± 0.25	3.11 ± 0.25	3.17 ± 0.26
1ES 1727+502 (HBL)	1.83 ± 0.26	1.83 ± 0.26	1.83 ± 0.26	1.84 ± 0.26	1.86 ± 0.26	1.93 ± 0.26
1ES 1959+650 (HBL) Method I	2.48 ± 0.05	2.48 ± 0.05	2.48 ± 0.05	2.48 ± 0.05	2.50 ± 0.05	2.55 ± 0.05
Method II	2.39 ± 0.11	2.40 ± 0.11	2.40 ± 0.11	2.40 ± 0.11	2.41 ± 0.11	2.47 ± 0.11
Mrk 180 (HBL)	2.94 ± 0.14	2.94 ± 0.14	2.94 ± 0.13	2.94 ± 0.13	2.96 ± 0.13	3.00 ± 0.13
1ES 2344+514 (HBL) Method I	2.25 ± 0.05	2.25 ± 0.05	2.25 ± 0.05	2.26 ± 0.05	2.27 ± 0.05	2.31 ± 0.05
Method II	2.26 ± 0.11	2.26 ± 0.11	2.26 ± 0.11	2.27 ± 0.11	2.28 ± 0.11	2.32 ± 0.11
Mrk 501 (HBL) Method I	2.55 ± 0.08	2.55 ± 0.08	2.55 ± 0.08	2.56 ± 0.08	2.61 ± 0.07	2.61 ± 0.07
Method II	2.33 ± 0.06	2.34 ± 0.06	2.34 ± 0.06	2.34 ± 0.06	2.36 ± 0.06	2.38 ± 0.06
Mrk 421 (HBL) Method I	2.75 ± 0.04	2.75 ± 0.04	2.75 ± 0.04	2.75 ± 0.04	2.77 ± 0.04	2.79 ± 0.04
Method II	2.64 ± 0.05	2.64 ± 0.05	2.64 ± 0.05	2.64 ± 0.05	2.65 ± 0.05	2.68 ± 0.05
RGB J2243 (HBL)	3.07 ± 0.40	3.07 ± 0.40	3.13 ± 0.37	3.42 ± 0.31	3.55 ± 0.31	3.56 ± 0.31
	1.98 ± 0.54	1.98 ± 0.54	2.35 ± 0.39	2.78 ± 0.35	2.83 ± 0.38	2.80 ± 0.40
	0.55 ± 0.69	0.56 ± 0.68	1.93 ± 0.26	1.99 ± 0.38	1.86 ± 0.46	1.80 ± 0.48
1RXS J023832 (HBL)	2.23 ± 0.72	2.24 ± 0.72	2.25 ± 0.72	2.37 ± 0.72	2.59 ± 0.73	2.64 ± 0.72
H 1722 (HBL)	3.05 ± 0.43	3.05 ± 0.43	3.05 ± 0.43	3.07 ± 0.43	3.14 ± 0.42	3.18 ± 0.42
	2.62 ± 0.46	2.63 ± 0.46	2.64 ± 0.46	2.73 ± 0.44	2.85 ± 0.43	2.87 ± 0.43
	2.11 ± 0.49	2.11 ± 0.49	2.16 ± 0.47	2.37 ± 0.42	2.49 ± 0.44	2.52 ± 0.45
MAGIC J2001 (IBL)	2.33 ± 0.37	2.33 ± 0.37	2.33 ± 0.37	2.36 ± 0.37	2.43 ± 0.39	2.47 ± 0.39
	2.30 ± 0.37	2.30 ± 0.37	2.30 ± 0.37	2.33 ± 0.37	2.41 ± 0.38	2.45 ± 0.39
VER J0521 (IBL)	2.87 ± 0.13	2.87 ± 0.13	2.88 ± 0.13	2.89 ± 0.13	2.97 ± 0.13	3.06 ± 0.13
	2.41 ± 0.13	2.41 ± 0.13	2.42 ± 0.13	2.48 ± 0.13	2.68 ± 0.13	2.76 ± 0.13

Appendix

IACTs

Instrument	Lat. (°)	Long. (°)	Alt. (m)	Tels.	Area (m²)	Pixels	FoV (°)	Thresh. (TeV)	Sens. (% Crab)
H.E.S.S.	-23	16	1800	4	428	960	5	0.1	0.7
VERITAS	32	-111	1275	4	424	499	3.5	0.1	1
MAGIC	29	18	2225	1	234	574	3.5†	0.06	2
CANGAROO	-31	137	160	3	172	427	4	0.4	15
Whipple	32	-111	2300	1	75	379	2.3	0.3	15
HEGRA	29	18	2200	5	43	271	4.3	0.5	5
CAT	42	2	1650	1	17.8	600	4.8†	0.25	15

Table: Properties of selected Cherenkov instruments, including two of historical interest (HEGRA and CAT).

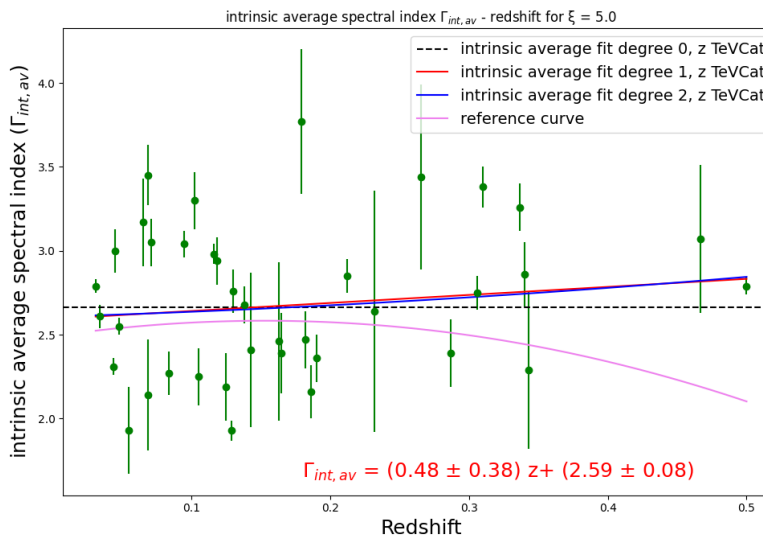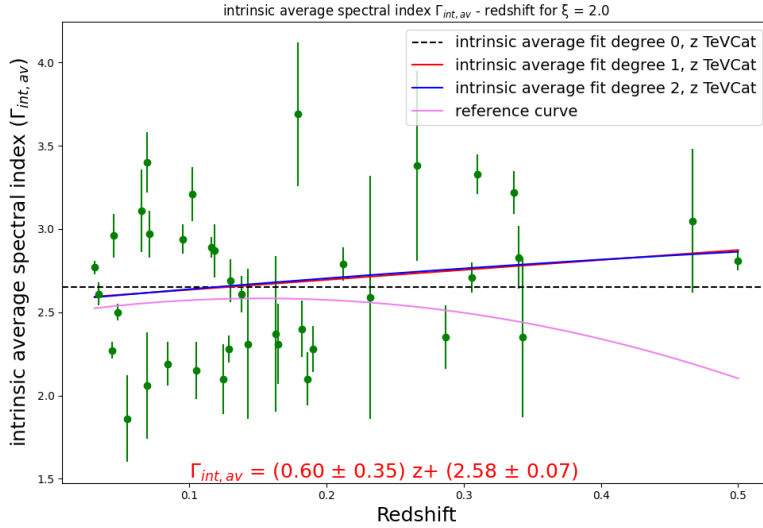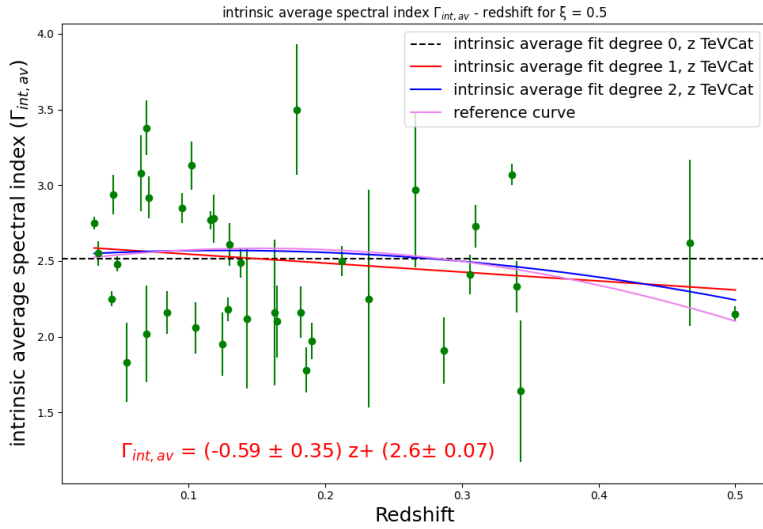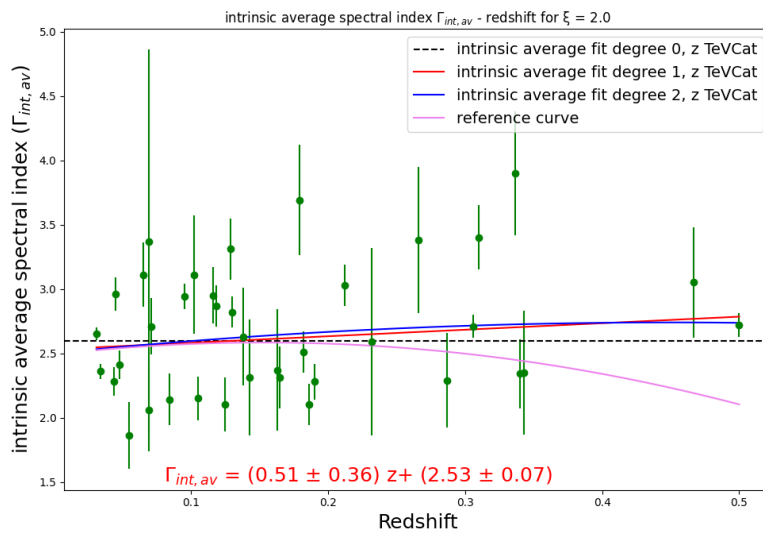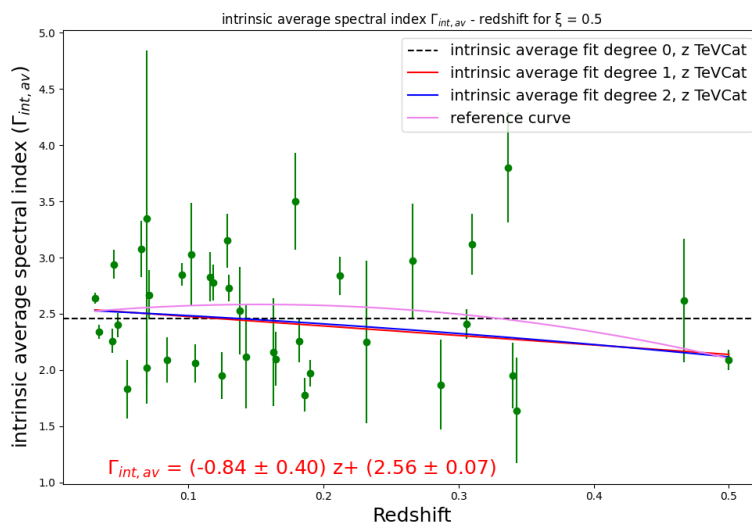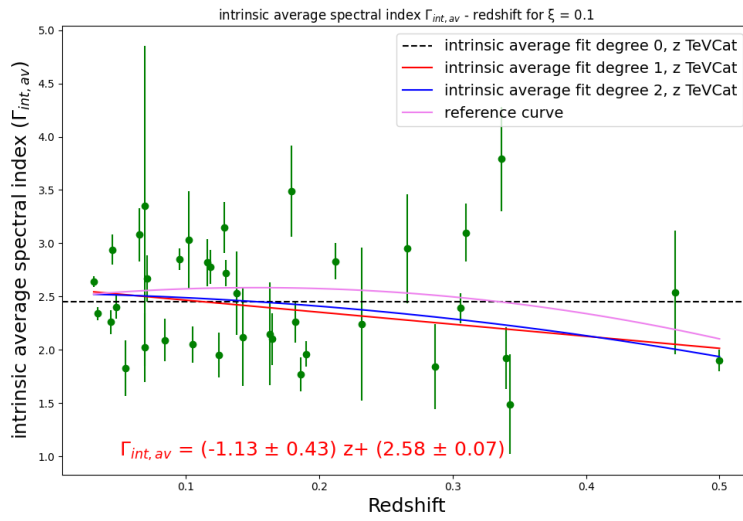## Average intrinsic spectral index-redshift plots obtained using Method I
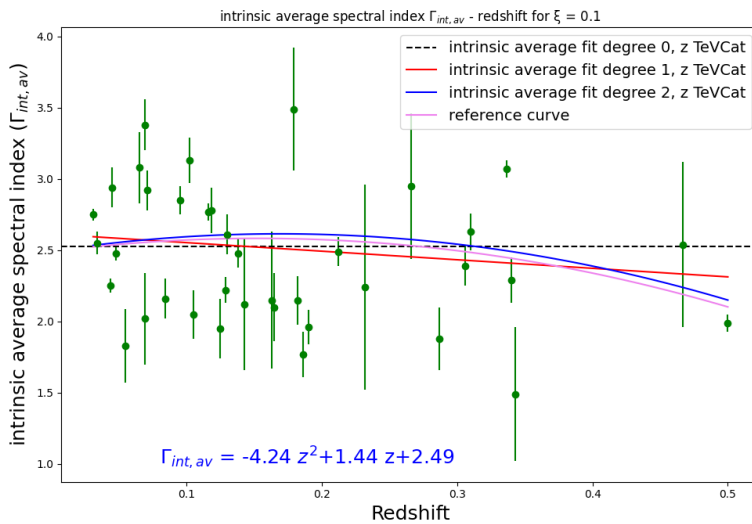
Figure: Scatter plots between average intrinsic VHE spectral index (Method I) of z TeVCat BL Lacs with redshift. In title is also indicated the value of ξ used. The red and blue solid lines are the best-fit straight line and parabola respectively. The dashed line is the best-fit of degree zero. It is also illustrated the equation of the curve with the best reduced chi-square. In pink the reference curve. The spectral indices of this plot are summarized in Table 8.

109

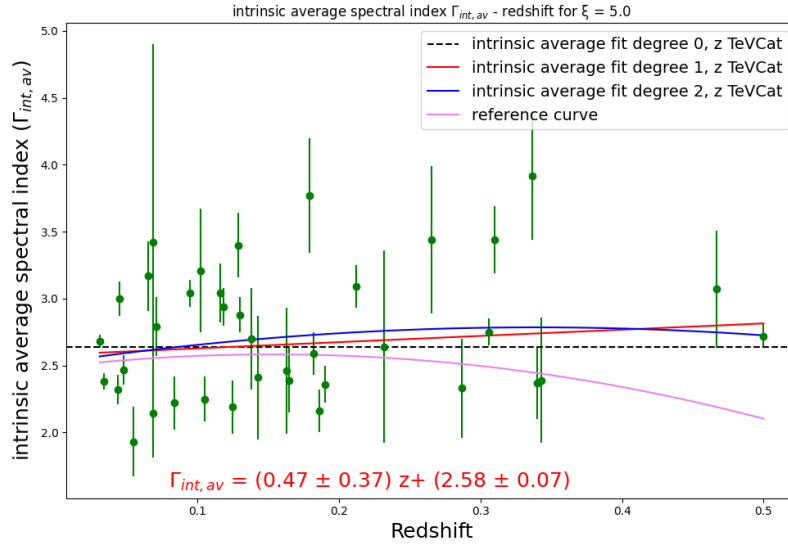# Average intrinsic spectral index-redshift plots obtained using Method II

Figure: Scatter plots between average intrinsic VHE spectral index (Method II) of z TeVCat BL Lacs with redshift. In title is also indicated the value of ξ used. The red and blue solid lines are the best-fit straight line and parabola respectively. The dashed line is the best-fit of degree zero. It is also illustrated the equation of the curve with the best reduced chi-square. In pink the reference curve. The spectral indices of this plot are summarized in Table 8.

Reference

1. **Galanti, G. et al.**, 2020, MNRAS, 493, 1553, Hint at an axion-like particle from the redshift dependence of blazar spectra.

2. **Franceschini, A. and Rodighiero, G.**, 2017, A&A, A34, 603, The extragalactic background light revisited and the cosmic photon-photon opacity.

3. **Galanti, G. and Roncadelli, M.**, 2018, PHYSICAL REVIEW D 043018, 98, Behavior of axionlike particles in smoothed out domainlike magnetic fields.

4. **Roncadelli, M.**, 2019, High-Energy Astrophysics and Axion-Like Particels (ALPs).

5. **Aharonian, F., et al.**, 2008, Rep. Prog. Phys, 096901,71, High energy astrophysics with ground-based gamma ray detectors.

6. **Amelino-Camelia, G., et al.** 1998, Nature, 393, 763-765, Tests of quantum gravity from observations of gamma ray bursts.

7. **Carroll, S. M., et al.**, 2001, Phys. Rev. Lett, 141601, 87, Noncommutative Field Theory and Lorentz Violation.

8. **Ellis, J., et al.** 2006, Astropart. Phys., 25, 402, Robust limits on Lorentz violation from gamma-ray bursts.

9. **Peccei, R.**, 2008, Lect. Notes Phys., 741, 3-17, The Strong CP Problem and Axions.

10. **Nakamura, K.,** 2010, Journal of Physics G: Nuclear and Particle Physics, 37, Review of Particle Physics.

11. **Wilczek, F.**, 1978, Physical Review Letters, 40, 279-282, Problem of Strong P and T In- variance in the Presence of Instantons.

12. **Weinberg, S.**, 1978, Physics Review Letter, 40, 223-226, "A New Light Boson?".

13. **Wilczek, F.**, 1978, Physics Review Letter, 40, 279-282, Problem of Strong P and T Invariance in the Presence of Instantons.

14. **Donnelly, T. W. et al.**, 1978, 1607, , Physic Review D, 18, Do Axion Exist?

15. **Zehnder, A.**, 1981, Physic Riview Letter, 104B, 494-498, Axion Search in a Monochromatic γ Transition: A New Lower Limit for the Axion Mass.

16. **Kim, J. E.**, 1979, Physical Review Letter, 103, 43, Weak Interaction Singlet and Strong CP Invariance.

17. **Dine, M., Fischler, W. and Srednicki, M.**,1981, Physics Letter, 199, B104, A Simple Solution to the Strong CP Problem with a Harmless Axion.

18. **Jaeckel, J. and Ringwald, A.** 2010, Annual Review of Nuclear and Particle Science, 60, 405-437, The Low-Energy Frontier of Particle Physics.

19. **Graham, P., Irastorza, I., Lamoreaux, S., Lindner, A. and van Bibber, K.** 1, 2015, Annual Review of Nuclear and Particle Science, 65, 485-514, Experimental Searches for the Axion and axionlike Particles.

20. **Zioutas, K., Aalseth, C., Abriola, D., III, F., Brodzin- ski, R., Collar, J., Creswick, R., Gregorio, D., Farach,H., Gattone, A., Guérard, C., Hasenbalg, F., Hasi- noff, M., Huck, H., Liolios, A., Miley, H., Morales, A., Morales, J., Nikas, D., Nussinov,** 1999, Nuclear Instruments and Methods in Physics Research Section A: Accelerators, Spectrometers, Detectors and Associated Equipment, 3, 425, 480-487, A decommissioned LHC model magnet as an axion telescope.

21 **Anastassopoulos, V., Aune, S., Barth, K. et al.**, 2017, Nature Phys, 13, 584-590, New CAST limit on the axion–photon interaction.

22. **Ayala, A., et al.**, 2014, Phys. Rev. Lett., 113

23. **Collaboration, The Fermi-LAT.**, 2016, Physical Review Letters, 16, 116, Search for Spectral Irregularities due to Photon – Axionlike - Parti- cle Oscillations with the Fermi Large Area Telescope.

24. **Gabuzda, D.**, 2018, Galaxies,1, 7, 5, Evidence for Helical Magnetic Fields Associated with AGN Jets and the Action of a Cosmic Battery.

25. **Larionov, V. et al.**, 2020, Monthly Notices of the Royal Astronomical Society, 3, 492, 3829-3848, Multiwavelength behaviour of the blazar 3C 279.

26. **Murphy, E., Cawthorne, T. and Gabuzda, D.**, 2013, Monthly Notices of the Royal Astronomical Society,13, 430, 1504-1515, Analysing the transverse structure of the relativistic jets of active galactic nuclei.

27 **Davies, J., Meyer, M. and Cotter, G.,** 2021, Phys. Rev. D, 023008, 103, Relevance of jet magnetic field structure for blazar axionlike particle searches.

28. **Kartavtsev, A., Raffelt, G. and Vogel, H.**, 2017, J. Cosmol. Astropart. Phys, 024, 01.

29. **Galanti, G. and Roncadeli, M.** arXiv:1805.12055.

30. **Davies, J., Meyer, M. and Cotter, G,** 2021. arXiv:2011.08123v2, **.** Relevance of jet magnetic field structure for blazar axionlike particle searches.

31. **Armengaud, E. et al.**, 2014, Journal of Instrumentation, 05, 9, T05002, Conceptual design of the International Axion Observatory (IAXO).

32. **Bähre, R. et al.** 2013, J. Instrum.

33. **Capparelli, L. M., et al.**, 2016, Phys. Dark Universe, 37, 12.

34. **Avignone III, F. T.**, 2009, Phys. Rev, D, 79.

35. **Avignone III, F. T., Crewick, R. J. and Nussinov, S.**, 2011, Astropart. Phys., 34, 640.

36. **Kahn, Y., Safdi, B. R. and Thaler, J.**, 2016, Phys. Rev. Lett, 117.

37. **Raffelt, G.G.**, 1996, Cambridge U. Press, 29, 5, 30, Stars as laboratories for fundamental physics.

38. **Raffelt, G.G.** 2008, Lect.Notes Phys., 741, 51-71, Astrophysical axion bounds.

39. **Archidiacono, M., et al.,** 2015, JCAP, 5, 1505, Future cosmological sensitivity for hot dark matter axions.

40. **Ayala, A., et al.**, arXiv:1406.6053, An improved bound on axion-photon coupling from Globular Clusters.

41. **Straniero, O., et al.,** 2015, 77-81, Axion-Photon Coupling: Astrophysical Constraints.

42. **Friedland, A., Giannotti, M. and Wise, M.**, 2013, Phys.Rev.Lett., 110, Constraining the Axion-Photon Coupling with Massive Stars.

43. **Dominguez, I., et al.**, 2017, Mem. Soc. Ast. It, 88, 270-273, On the influence of axions on Mup.

44. **Moody, J.E. and Wilczek, F.**, 1984, Phys. Rev. D30, 130, New Macroscopic Forces?

45. **Redondo, J. and Ringwald, A.** 2011, Contemp. Phys. 52, 211-236, Light shining through walls.

46. **De Angelis, A., M., Roncadelli and Mansutti, O.**, 2007, Phys. Rev. D, 121301, 76.

47. **De Angelis, A., Mansutti, O. and Roncadelli, M.**, 2008, Phys. Lett. B, 847, 659.

48. **Tavecchio, F. et al.**, 2012, Phys. Rev. D, 080536, 86.

49. **Tavecchio, F., Roncadelli, M. and Galanti, G.**, 2015, Physics Letters B, 375, 744.

50. **Franceschini, A., Rodighiero, G. and Vaccari, M.**, 2008, A&A, 3, 487, 837-852, Extragalactic optical-infrared background radiation, its time evolution and the cosmic photon-photon opacity.

51. **Dole, H., et al.**, 2006, Astronomy and Astrophysics, 451, 417, The cosmic infrared background resolved by Spitzer. Contributions of mid-infrared galaxies to the far-infrared background.

52. **Madau, P. and Dickinson, M.,** 2014, Annu. Rev. Astron. Astrophys, 52, 415, Cosmic Star-Formation History.

53. **Franceschini, A., et al.,** 2001, Astron. Astrophys., 378, A long-wavelength view on galaxy evolution from deep surveys by the Infrared Space Observatory.

54. **Magorrian, John, et al.**, 1998, Astrophysical Journal, 115, 2285, The Demography of Massive Dark Objects in Galaxy Centers.

55. **Heger, A. and E., Woosley S.**, 2002, ApJ, 567, 532, The Nucleosynthetic Signature of Population III.

56 **Carr, B. J., Bond, J. R. and Arnett, W. D.**, 1984, ApJ, 277, 445, . Cosmological consequences of Population III stars.

57. **Leinert, C. et al.**, 1998, AAS, 1, 127.

58. **Gilmore, R.C. et al.**, 2012, MNRAS, 1992, 422.

59. **Somerville, R. et al.**, 2012, MNRAS, 1992, 423.

60. **Madau, P. and Pozzetti, L.**, 2000, MNRAS, L9, 312.

61. **Franceschini, A. et al.**, 1994, ApJ, 140, 427.

62. **Malkan, M. and Stecker, F.**, 1998, ApJ, 13, 496.

63. **Franceschini, A., Aussel, H., Cesarsky, C. J., Elbaz, D., Fadda, D.**, 2001, AA, 1, 378.

64. **Kneiske, T., Mannheim, K. and Hartmann D.**, 2002, AA, 1, 386.

65. **Franceschini, A. and Rodighiero, G.**, 2017, AA, A34, 603.

66. **Planck Collaboration,**2020, A&A, A6, 641.

67 **Krolik, Julian H.** 1999, Active galactic nuclei: from the central black hole to the galactic environment.

68. **Nalewajko, K. et al.,** 2019, Long-term optical spectroscopic variations in blazar 3C 454.3. https://arxiv.org/abs/1909.01357.

69. **Amaya-Almazan, R.A., Chavushyan, V. and Patino-Alvarez, V.M,** 2020. https://arxiv.org/abs/2011.08762**,** Multiwavelength analysis and the difference in the behavior of the spectral features during the 2010 and 2014 flaring periods of the blazar 3C 454.

70. **Abeysekara, A. U. et al.,** https://arxiv.org/abs/2002.03567, The Great Markarian 421 Flare of February 2010: Multiwavelength variability and correlation studies.

71. **Allen, C. et al.**, https://arxiv.org/abs/1708.02829, Very-High-Energy γ-Ray Observations of the Blazar 1ES 2344+514 with VERITAS.

72. **Aharonian, F. et al.**, 2007, ApJ, L71, 664, An Exceptional Very High Energy Gamma-Ray Flare of PKS 2155-304.

73. **Franceschini, A.,** High energy emission from AGNs.

74. **Ghisellini, G. and Tavecchio, F.** 2008, MNRAS, 387, The blazar sequence: a new perspective.

75. **Moore, R. L. and Stockman, H. S.**, 1981, ApJ, 60, 243.

76. **Stickel, M. et al.**, 1991, ApJ Letters, L17, 400.

77. **Stocke, J.T. et al.**, 1990, ApJ, 141, 348.

78. **Urry, C. M. and Padovani, P.**, 1991, ApJ, 60, 371.

79. **Padovani, P., Giommi, P. and Rau, A.**, 2012, MNRAS, L48, 422.

80. **Gabuzda, D. C. et al.**, 1989, ApJ, 701, 347.

81. **Marscher, A. P. et al.**, 2002, ApJ, 85, 577.

82. **Ghisellini, et al.**, 1993, ApJ, 65, 407.

83. **Maraschi, L. and Rovetti, F.**, 1994, ApJ, 79, 436.

84. **Sambruna, R. M., Maraschi, L. and Urry, C. M.**, 1996, ApJ, 444, 463.

85. **Scarpa, R. and Falomo, R.**, 1997, A&A, 109, 325.

86. **Costamante, L., Ghisellini, G. and Giommi, P., et al.**, 2001, A&A, 512, 371.

87. **Ghisellini, G., Tavecchio, F. and Foschini, L., et al.**, 2010, MNRAS, 497, 402.

88. **Potter, W.J. and Cotter, G.**, 2013, MNRAS, 304, 436.

89. **Blandford, R. D. and Znajek, R. L.**, 1977, MNRAS, 433, 179.

90. **Maraschi, L. and Tavecchio, F**, 2003, ApJ, **.** 667, 593.

91. **Ostorero, L., Villata, M. and Raiteri, C. M.**, 2004, A&A, 913, 419.

92. **Padovani, P., et al.**, 2007, ApJ, 182, 662.

93. **Falomo, R., Pesce, J. E. and Treves, A.**, 1993, A.J., 2031, 105.

94. **Asano, K., et al.**, 2014, Ap.J., 64, 780.

95. **Maselli, A., Massaro, E. and Nesci, R., et al.**, 2010, A&A, A74, 512.

96. **Birkinshaw, M., Worrall, D. M. and Hardcastle, M. J.**, 2002, MNRAS, 142, 335.

97. **Scarpa, R. et al.**, 1999, ApJ, 643, 526.

98. **Jorstad et al.,** 2010.

99 **Meisner, A.M. and Romani, R.W.**, 2010, ApJ, 712, 14-25, Imaging Redshift Estimates for BL Lacertae Objects.

100. **Sbarufatti, B., Treves, A. and Falomo, R.**, 2005, ApJ, 132, 1.

101. **Abeysekara, A.U., Archambault, S. and Archer, A. et al.**, 2017, The Astrophysical Journal Supplement Series, 1, 233, Discovery of Very-high-energy Emission from RGB J2243+203 and Derivation of Its Redshift Upper Limit.

102. **Georganopoulos, M., Finke, J. D. and Reyes, L. C.**, 2010, ApJ, 714, L157.

103. **Cerruti, M., et al.**, 2017, 6th International Symposium on High Energy Gamma-Ray Astronomy, 050027, 1792.

104. **Sahu, Sarira, López Fortín, Carlos E. and Nagataki, Shigehiro**, 2019, The Astrophysical Journal Letters, 1, 884, Multi-TeV Flaring from High-energy Blazars: An Evidence of the Photohadronic Process.

105. **Rosa González, D. et al.,** February 2019, Monthly Notices of the Royal Astronomical Society, arXiv:1811.03948, New GTC spectroscopic data and a statistical study to better constrain the redshift of the BL Lac RGB J2243 + 203.

106. **Durrer, R. and Neronov, A.**, 2013, Astron. Astrophys, 62, 21, Cosmological magnetic fields: their generation, evolution and observation.

107. **Rees, M.J. and Setti, G.**, 1968, Nature, 127, 219.

108. **Hoyle, F.,** 1969, Nature, 936, 223.

109. **Kronberg, P.P., Lesh, H. and Hopp, U.**, 1999, Astrophys. J., 56, 511.

110. **Cowie, L., et al.**, 1995, Astron. J., 1522, 109.

111. **Pshirkov, M.S., Tinyakov, P.G. and Urban, F. R.,** 2016, Phys. Rev. Lett., 191302, 116.

112. **Durrer, R. and Neronov, A.**, 2013, Astron. Astrophys. Rev, 62, 21.

113. **Mortsell, E., Bergstrom, L. and Goobar, A.**, 2002, Phys. Rev. D, 047702, 66, Photon axion oscillations and type Ia supernovae.

114. **Csaki, C., Kaloper, N. and Terning, J.**, 2002, Phys. Rev. Lett., 161302, 88, Dimming supernovae without cosmic acceleration

115. **Mortsell, E. and Goobar, A.**, 2003, JCAP, 003, 0304, Constraining photon-axion oscillations using quasar spectra.

116. **Grasso, D and Rubinstein, H.R.**, 2001, Phys. Rept, 348, 163-266, Magnetic fields in the early Universe.

117. **Widrow, L.M., et al.**, 2012, Space Sci. Rev., 166, 37-70, The first magnetic fields.

118. **Raffelt, G.G. and Stodolsky, L.**, 1988, Phys. Rev. D, 37, 1237.

119. **Heisenberg, W. and Euler, H.**, 1936, Phys., 98, 714.

120. **Dweck, E. and Jrennrich, F.**, 2013, Astropart. Phys., 112, 43.

121. **Dobrynina, A., Kartavtsev, A. and Raffelt, G.,** 2015, Phys. Rev. D, 91.

122. **Paiano, S., Franceschini, A. and Stamerra, A.**, 2017, Monthly Notices of the Royal Astronomical Society, 31, 1, A new method to unveil blazars among multi-wavelength counterparts of Unassociated Fermi γ-ray Sources.

123. **Galanti, G. and Roncadelli, M.** J. High Energy Phys.

124. **Aharonian, F., et al.**, 2007, ApJ, 664, L71

Ringraziamenti

Voglio ringraziare tutte le persone che mi sono state accanto durante questo lungo percorso, dandomi una mano, ognuno a modo suo. Sto pensando a quante volte sono stato ascoltato in vista di un esame, a tutte le volte che anche in condizioni di stress mi avete fatto sorridere, a tutte le volte che mi avete reso la vita più semplice, a tutti i sacrifici fatti per farmi arrivare fino a qui. Mi fate sentire una persona veramente speciale. Alla mia famiglia, non potrei aver avuto dei genitori e delle sorelle migliori!